Stony Brook University

Refining mid-infrared emission spectroscopy as a tool for understanding planetary surface mineralogy through laboratory studies, computational models, and lunar remote sensing data

A Dissertation Presented

by

Jessica Anne Arnold

to

The Graduate School

in Partial Fulfillment of the

Requirements

for the Degree of

Doctor of Philosophy

in

Geosciences

Stony Brook University

May 2014

Stony Brook University

The Graduate School

Jessica Anne Arnold

We, the dissertation committee for the above candidate for the

Doctor of Philosophy degree, hereby recommend

acceptance of this dissertation.

Dr. Timothy Glotch – Dissertation Advisor
Associate Professor, Geosciences

Dr. Hanna Nekvasil - Chairperson of Defense
Professor, Geosciences

Dr. Deanne Rogers
Assistant Professor, Geosciences

Dr. Scott McLennan
Professor, Geosciences

Dr. Joshua Bandfield
Research Scientist
Space Science Institute

This dissertation is accepted by the Graduate School

Charles Taber
Dean of the Graduate School

Abstract of the Dissertation

Refining mid-infrared emission spectroscopy as a tool for understanding planetary surface mineralogy through laboratory studies, computational models, and lunar remote sensing data

by

Jessica Anne Arnold

Doctor of Philosophy

in

Geosciences

Stony Brook University

2014

Mid-infrared emissivity spectra, while useful for quantifying mineral abundance, are dependent on a variety of other factors, including grain size. At present, scattering models are not fully able reproduce this dependence, especially for very fine-grained powders (d~<60μm) typical of planetary regolith. Previous studies have modeled emissivity spectra of mineral powders by using Mie single scattering theory coupled with a radiative transfer model, such as Hapke [1993]. Chapter 2 of this work uses multiple scattering T-matrix code (from Mackowski and Mishchenko, 2011) to calculate the scattering coefficients for a cluster of spheres, rather than a single sphere as in Mie theory. I acquired emissivity spectra of highly uniform silica glass spheres, normally used for sieve calibration, for comparison to modeled spectra. Then, I calculated optical constants of the glass from micro-FTIR reflectance spectra of polished grains mounted on a petrographic slide. Modeled emissivity spectra computed with this T-

matrix/radiative transfer hybrid method show a marked improvement over Mie-radiative transfer hybrid models, especially for smaller grain sizes.

The complex index of refraction ($\tilde{n}=n+ik$) as a function of wavelength, where n and k are often referred to as optical constants, is an essential input into radiative transfer models. Hence, quantitative estimates of mineral abundance from remote sensing data require that optical constants are known for a comprehensive set of relevant minerals. While many geologically abundant materials are monoclinic or triclinic, due to both the additional complexity of the models needed and the increased effort required to orient these samples, very few sets of optical constants have been measured for lower-symmetry minerals. Chapter 3 describes how optical constants were calculated from polarized mid-infrared reflectance spectra of oriented single-crystals of five natural samples in the monoclinic crystal system, which include four pyroxene samples and one orthoclase sample.

Lastly, in Chapter 4, remote sensing emissivity data from the Diviner Lunar Radiometer Experiment, along with lunar environment laboratory measurements of mineral mixtures, are used to establish constraints on the absolute abundance of olivine at sites where it has been detected by the visible/near-infrared instruments Moon Mineralogy Mapper and Kaguya Spectral Profiler. The two main results of this section are: 1) spectra do not mix linearly at these wavelengths for particles sizes typical of lunar regolith and 2) Diviner data are consistent with a wide range in olivine abundances at these sites.

Table of Contents

Acknowledgements

I would like to thank

...

My advisor, Timothy Glotch for all of the amazing opportunities he's given me during my time at Stony Brook and for his seemingly boundless patience and encouragement

My committee members: Hanna Nekvasil, Deanne Rogers, Scott McLennan, and Josh Bandfield for taking the time to evaluate this work.

The Geosciences Staff for their support, especially Yvonne Barbour and Diane Isgro for guiding me though the labyrinth of Stony Brook's administration

Everyone in our ever-growing and never boring research group: Congcong Che, Matt Ferrari, Lonia Friedlander, Eli Sklute, Alexis Martone, Steven Jaret, Steve Liu, Katherine Shirley, Melinda Rucks, and Gen Ito

My friends, especially all those I've crossed paths with at the Graduate Christian Fellowship

And finally my family who has given me so much support and has always encouraged my enthusiasm for science

List of Figures

Chapter 2

Chapter 4

List of Tables

Chapter 2

Chapter 3

Chapter 4

Chapter 1: Introduction and overview

1.1 Introduction

Mid-infrared (mid-IR), 2.5-100 μm or 100-4000 cm^{-1}, spectroscopy is a valuable tool for understanding the mineralogy of planetary surfaces. Mid-IR data from the Lunar Reconnaissance Orbiter (LRO) Diviner Lunar Radiometer Experiment (Diviner) have been used to study broad-scale lunar mineralogy [*Greenhagen et al.*, 2010], identify areas with highly silicic compositions [*Glotch et al.*, 2010b], characterize regions of nearly pure plagioclase composition [*Donaldson Hanna et al.*, 2012], identify the composition of crater central peaks [*Song et al.*, 2013], and investigate olivine-bearing lithologies (this work). However, in addition to composition, mid-IR emissivity is also a function of many other factors including grain size distribution, shape, and packing [*Hunt and Logan*, 1972; *Salisbury and Wald*, 1992], as well as atmospheric pressure [*Logan and Hunt*, 1970].

A better understanding of how light interacts planetary regolith and the parameters that go into scattering models is essential for making the most of mid-IR orbital data. The aim of this work is to address some of the challenges involved in obtaining quantitative estimates of mineral abundance from mid-IR remote sensing data. In particular, I focus on improving the match between laboratory measurements and emissivity models for fine particulates by improving the input parameters for these models. I also discuss work to use laboratory and Diviner emissivity data to place upper limits on olivine abundance in locations where it has been identified on the lunar surface with visible/near-infrared remote sensing instruments. This includes an investigation of non-linearity of spectral mixing for fine particulates (<63 μm), which make up a large fraction of the near-surface regolith of the Moon as well as other solar system objects.

1.1.1 Spectral Emissivity

When sunlight hits a planetary surface, it is either reflected or absorbed and subsequently re-emitted at longer wavelengths (lower energy). The majority of reflected radiation is at visible/near infrared (VNIR) wavelengths, while emitted radiation is at mid-IR wavelengths. The relation between emitted intensity (B_λ) and wavelength (λ) for a black-body surface at a given temperature (T) is known as Planck's law, where k_B is Boltzmann's constant, h is Planck's constant, and c is the speed of light.

$$B_\lambda = \frac{2hc^2}{\lambda^5}\frac{1}{e^{hc/\lambda k_B T}-1}. \qquad (1.1)$$

A black-body absorbs all incident radiation at all wavelengths, and re-emits it according to this characteristic function. Spectral emissivity, or emissivity as a function of wavelength, is defined as the ratio between the measured radiance of the surface and that of a perfectly emitting blackbody at the same temperature as the surface, $\varepsilon_\lambda = \frac{I_\lambda}{B_\lambda(T)}$ (1.2), so that a perfect emitter has an emissivity of one at all wavelengths. For a laboratory samples, temperature can be measured directly, although in practice this can be difficult. Hence, in laboratory emissivity measurements [*Ruff et al.*, 1997] as well as in remote sensing, a quantity called brightness temperature (T_b) is used to estimate the surface temperature. To get the brightness temperature, portions of the measured spectrum where the surface has a known emissivity, usually at or very close to one, are fit to a blackbody curve.

1.1.2 Features of mid-IR emissivity spectra

One class of minima in emissivity spectra at mid-IR wavelengths are known as Reststrahlen bands (RB). These bands are the result of lattice vibrations, for example Si-O stretching, that

cause an increase in the absorption coefficient at certain wavelengths [e.g. *Salisbury et al.*, 1994]. Changes in the shapes and positions of RBs can be related to mineralogy [*Lyon*, 1965; *Salisbury and Walter*, 1989].

Diviner makes use of an emissivity maximum (and reflectance minimum) of silicates [*Conel*, 1969] known as the Christiansen feature (CF) to characterize lunar silicate mineralogy [*Greenhagen et al.*, 2010]. This feature occurs where the real index of refraction of the material approaches that of the incident medium, just short of the RBs. This feature is related to polymerization of the silica tetrahedra, with tectosilicates such as quartz having an emissivity maximum at shorter wavelengths, whereas for orthosilicates such as olivine this maximum occurs at longer wavelengths [*Nash et al.*, 1993]. Diviner has three channels centered near 8μm, selected so that the wavelength where the CF occurs can be estimated with a parabolic fit.

1.1.3 Radiative transfer models

All radiative transfer models are based on the equation of radiative transfer (ERT) laid out by *Chandrasekhar* [1960]. The following is one form of this equation:

$$\frac{dI_\nu(s,\boldsymbol{\Omega})}{ds} + [\gamma_\nu(s) + \sigma_\nu(s)]I_\nu(s,\boldsymbol{\Omega}) =$$

$$\gamma_\nu(s)I_{\nu B}\,[T(s)] + \frac{1}{4\pi}\sigma_\nu(s)\iint_{\Omega'=4\pi} I_\nu(s,\boldsymbol{\Omega}')p(\boldsymbol{\Omega}',\boldsymbol{\Omega})d\Omega'. \qquad (1.2)$$

This equation, which has four components, describes light passing through a medium that scatters, absorbs and emits radiation. On the right-hand side, the first component is the thermal emission, which in the case of local thermodynamic equilibrium is related to both the Planck function and $\gamma_\nu(s)$, the absorption coefficient, ($\gamma_\nu(s)I_{\nu B}\,[T(s)]$), and the second is radiation

scattered towards the direction of observation ($\frac{1}{4\pi}\sigma_\nu(s)\iint_{\Omega'=4\pi} I_\nu(s,\boldsymbol{\Omega}')p(\boldsymbol{\Omega}',\boldsymbol{\Omega})d\Omega'$). Here, σ_ν is the scattering coefficient and $p(\boldsymbol{\Omega}',\boldsymbol{\Omega})$ is the phase function. On the left hand side are losses due to absorption ($\gamma_\nu(s)I_\nu(s,\boldsymbol{\Omega})$) and ($\sigma_\nu(s)I_\nu(s,\boldsymbol{\Omega})$) of radiation scattered away from the observation direction [*Sharkov*, 2003]. A more condensed form of this equation includes the single-scattering albedo (*w*):

$$w_\nu = \frac{\sigma_\nu(s)}{\gamma_\nu(s) + \sigma_\nu(s)}$$

Different radiative transfer formulations arise from assumptions made in the context of the particular problem at hand to simplify the ERT and reduce the computational burden (for example neglecting scattering).

There are also various methods for estimating two parameters included in the RTE, single scattering albedo (*w*) and the phase function p(g), where g is the complement of the scattering angle. Single scattering albedo describes the relative probability of a scattering versus absorption event and the phase function is the probability of scattering at particular angle relative to the direction of incidence. Both of these parameters are functions of the optical constants of the material, which refer to the real and imaginary portions of the complex index of refraction (ñ=*n*+i*k*), where *n* is the real index and *k* is the imaginary index of refraction. Hence, having a comprehensive library of optical constants is crucial for the application of radiative transfer models to planetary regoliths.

1.1.4 Motivation and goals

I seek to address two main issues with interpreting mid-IR spectra obtained from remote sensing instruments. First, current models for emissivity as a function of particle size are not well

suited to finely particulate surfaces. As particle size decreases, so does the spectral contrast of the RB [*Salisbury and Wald*, 1992]. This effect is under-estimated by current models [*Moersch and Christensen*, 1995; *Pitman et al.*, 2005]. In addition, new spectral features, due to transmission of light through particles appear in the spectra. Second, there is a dearth of mid-infrared optical constants of low-symmetry minerals; hence, many important mineral classes, including pyroxenes and feldspars, are excluded from current optical constant libraries.

Several formulations based on the ERT for have been put forth by *Hapke* [1993]; [*Hapke*, 1996]; *Hapke* [2008] for both reflectance and emission from planetary surfaces. These were developed for modeling closely packed particulates whose size is much larger than the wavelength of incident radiation. This assumption is not applicable to the mid-IR for planetary regolith where particle size is comparable to wavelength. Hapke's formulas for calculating *w* and p(g) ignore diffraction, an important effect at these scales. Hence, there have been some efforts to test coupled approaches that use Mie single scattering theory to derive these parameters and then use Hapke's model for reflectance and emission as a function of these parameters. This, however, replaces one problematic assumption with another, namely that particles are well separated enough to ignore multiple scattering. I examine replacing Mie single scattering in these coupled models with a multiple scattering T-matrix model (also called the extended boundary condition method), that explicitly solves Maxwell's equations at each light-particle interface, and can be used for densely packed particles of any size relative to the wavelength of light [*Mishchenko*, 2008].

As mentioned earlier, the scattering parameters *w* and p(g) depend on optical constants. There are published sets of optical constants for only two geologically relevant monoclinic

minerals: orthoclase and gypsum. I developed code to calculate optical constants for minerals in the monoclinic crystal system and apply it to orthoclase and several clinopyroxenes.

Additionally, I am interested in applying mid-IR remote sensing data from Diviner to understand lunar surface mineralogy. Olivine has been detected in several locations using VNIR instruments [*Mustard et al.*, 2011; *Yamamoto et al.*, 2010; 2012]. These detections are mostly confined to the walls and ejecta of small craters near the edge of large impact basins where the lunar crust has been thinned [*Yamamoto et al.*, 2010]. As part of this study, I look at whether linear mixing between components of mid-IR spectra of small particles (<63 μm) can be assumed and how mixing behaviors change in ambient versus near-vacuum pressures. I then use spectra acquired under lunar-like environmental conditions of olivine-plagioclase mixtures to estimate upper limits of olivine abundance within the areas of interest and discuss how these measurements relate to models for the exposure of olivine at the lunar surface.

1.2 Overview of chapters

This dissertation contains five chapters, including this introduction. The subsequent three chapters each focus on a different aspect of mid-IR spectroscopy. Section 1.1 discussed the motivation behind choosing these topics, while this section outlines the structure of the dissertation and gives an overview of the methods to address each of these topics. The final chapter provides a summary and discusses future directions.

Chapter 2 evaluates the efficacy of a multiple sphere T-matrix method (MSTM) for calculating single scattering albedo and the cosine asymmetry, two key input parameters for radiative transfer models. These same parameters are calculated using Mie single-scattering theory. Both sets of inputs were coupled with three different radiative transfer models that give

approximate analytical expressions for hemispherical emissivity from a semi-infinite plane-parallel layer of particulates. Two of these are widely used: [*Hapke,* 1993] and [*Conel,* 1969] . The third, Hapke [1996], can be used to approximate the emissivity of a medium heated from below and, while less frequently applied to planetary remote sensing, was chosen for study due its applicability to laboratory conditions. Modeled MSTM/RT and Mie/RT emissivity spectra are compared with measured spectra of monodisperse (i.e. uniformly sized) silica spheres of four different diameters. This chapter is being prepared for publication in *Journal of Geophysical Research—Planets.*

Chapter 3 details a method for measuring mid-IR optical constants of minerals in the monoclinic crystal system and applies this method to one orthoclase and four clinopyroxene samples. The derivation of mid-IR optical constants requires polarized specular reflectance spectra of oriented single crystals. I describe how samples were characterized, oriented and prepared. Then, I provide an overview of the mathematical formulation of dispersion theory, which treats vibrations within a crystal lattice as damped harmonic oscillators. Parameters that describe these oscillators are related to the complex index of refraction (n+ik), where n and k are known as the optical constants. The equations necessary to relate the optical constants to reflectance as a function of polarization with respect to the crystal axes and incidence angle of the incoming electromagnetic field are outlined. For this later set of equations, I chose to use the formulation of [*Mayerhöfer et al.,* 2011] based on Berreman's [1972] 4x4 matrix method, and discuss why this is a robust method. I wrote a Matlab script to iteratively fit the laboratory reflectance spectra using estimated dispersion parameters. The refined oscillator parameters are then used to calculate the optical constants.

I chose a gem-quality orthoclase sample as a test-case for my code and laboratory techniques, so that the derived optical constants could be compared with previously published values [*Aronson*, 1986]. Once the method was validated, I chose to focus on clinopyroxene, as this is a major rock-forming mineral group with only one set of optical constants published in the literature [*Jäger et al.*, 1998]. I made an effort to select samples with a wide range of calcium, magnesium and iron contents. A manuscript based on this work is currently in press at *American Mineralogist*.

Chapter 4 describes a survey of Diviner data for locations on the Moon that are known from visible/near-infrared orbital observations to be relatively enriched in olivine, with little or no pyroxene. This study focus on detections by the Kaguya Spectral Profiler (SP) instrument from *Yamamoto et al.* [2010] as this is the most comprehensive survey to date of such lithologies. VNIR reflectance data from Chandryaan-1 Moon Mineralogy Mapper (M^3) are used to confirm these detections. The Diviner emissivity spectra were then extracted from the same locations as the M^3 spectra. The wavelength position of the CF is estimated by finding the wavelength of maximum emissivity from a parabolic fit to Diviner's three mineralogical channels. A correction to the CF to account for the effects of space weathering on mineralogical interpretation is also described.

I describe a set of lunar environment emissivity spectra of olivine-plagioclase mixtures that were acquired at the University of Oxford's Atmospheric, Oceanic and Planetary Physics department [*Thomas et al.*, 2010] for comparison with Diviner remote sensing data. This allows for comparison of the measured mixture spectra to spectra modeled using the assumption of linear mixing well as characterization of the response of the CF position as estimated from Diviner data to mixture composition. Assuming that the areas of interest can be modeled as a

two-component mixture of olivine and plagioclase, I determine the upper bounds on the abundance of olivine present at these sites and discuss the relationship between these measurements and published models for the transport of olivine to the lunar surface. A manuscript based on this chapter is nearly ready to be submitted to *Geophysical Research Letters*.

In Chapter 5, I summarize the main conclusions of the preceding chapters and explore possible avenues for building on this work. One near-term goal is to tackle the problem of obtaining optical constants for triclinic minerals. I would also like to explore how packing density and particle shape affect emissivity spectra modeled using the coupled T-matrix/RT method and to explore more exact radiative transfer models. An eventual goal is to test the ability of these models to derive mineralogy under conditions of non-linear mixing against laboratory data.

References

Aronson, J. R. (1986), Optical constants of monoclinic anisotropic crystals: orthoclase, *Spectrochimica Acta Part A: Molecular Spectroscopy*, *42*(2), 187-190.

Berreman, D. W. (1972), Optics in stratified and anisotropic media: 4× 4-matrix formulation, *JOSA*, *62*(4), 502-510.

Chandrasekhar, S. (1960), Radiative Transfer, *Dover*.

Conel, J. E. (1969), Infrared emissivities of silicates: Experimental results and a cloudy atmosphere model of Spectral emission from condensed particulate mediums, *Journal of Geophysical Research*, *74*(6), 1614-1634.

Donaldson Hanna, K. L., M. B. Wyatt, I. R. Thomas, N. E. Bowles, B. T. Greenhagen, A. Maturilli, J. Helbert, and D. A. Paige (2012), Thermal infrared emissivity measurements under a simulated lunar environment: Application to the Diviner Lunar Radiometer Experiment, *Journal of Geophysical Research: Planets*, *117*(E12), E00H05.

Glotch, T. D., et al. (2010), Highly Silicic Compositions on the Moon, *Science*, *329*(5998), 1510-1513.

Greenhagen, B. T., et al. (2010), Global Silicate Mineralogy of the Moon from the Diviner Lunar Radiometer, *Science*, *329*(5998), 1507-1509.

Hapke, B. (1993), Introduction to the Theory of reflectance and Emission Spectroscopy, edited, Cambridge University Press, New York.

Hapke, B. (1996), A model of radiative and conductive energy transfer in planetary regoliths, *Journal of Geophysical Research: Planets (1991–2012)*, *101*(E7), 16817-16831.

Hapke, B. (2008), Bidirectional reflectance spectroscopy: 6. Effects of porosity, *Icarus*, *195*(2), 918-926.

Hunt, G. R., and L. M. Logan (1972), Variation of Single Particle Mid-Infrared Emission Spectrum with Particle Size, *Appl. Opt.*, *11*(1), 142-147.

Jäger, C., F. Molster, J. Dorschner, T. Henning, H. Mutschke, and L. Waters (1998), Steps toward interstellar silicate mineralogy. IV. The crystalline revolution, *Astronomy and Astrophysics*, *339*, 904-916.

Logan, L. M., and G. R. Hunt (1970), Emission spectra of particulate silicates under simulated lunar conditions, *Journal of Geophysical Research*, *75*(32), 6539-6548.

Lyon, R. J. P. (1965), Analysis of rocks by spectral infrared emission (8 to 25 microns), *Economic Geology*, *60*(4), 715-736.

Mackowski, D. W., and M. I. Mishchenko (1996), Calculation of the< i> T</i> matrix and the scattering matrix for ensembles of spheres, *JOSA A*, *13*(11), 2266-2278.

Mayerhöfer, T. G., S. Weber, and J. Popp (2011), Simplified formulas for non-normal reflection from monoclinic crystals, *Optics Communications*, *284*(3), 719-723.

Mishchenko, M. I. (2008), Multiple scattering, radiative transfer, and weak localization in discrete random media: unified microphysical approach, *Reviews of Geophysics*, *46*(2).

Moersch, J., and P. R. Christensen (1995), Thermal emission from particulate surfaces: A comparison of scattering models with measured spectra, *Journal of Geophysical Research: Planets (1991–2012)*, *100*(E4), 7465-7477.

Mustard, J. F., et al. (2011), Compositional diversity and geologic insights of the Aristarchus crater from Moon Mineralogy Mapper data, *Journal of Geophysical Research: Planets*, *116*(E6), E00G12.

Nash, D. B., J. W. Salisbury, J. E. Conel, P. G. Lucey, and P. R. Christensen (1993), Evaluation of infrared emission spectroscopy for mapping the moon's surface composition from lunar orbit, *Journal of Geophysical Research: Planets*, *98*(E12), 23535-23552.

Pitman, K. M., M. J. Wolff, and G. C. Clayton (2005), Application of modern radiative transfer tools to model laboratory quartz emissivity, *Journal of Geophysical Research: Planets (1991–2012)*, *110*(E8).

Salisbury, J. W., and L. S. Walter (1989), Thermal infrared (2.5–13.5 μm) spectroscopic remote sensing of igneous rock types on particulate planetary surfaces, *Journal of Geophysical Research: Solid Earth*, *94*(B7), 9192-9202.

Salisbury, J. W., and A. Wald (1992), The role of volume scattering in reducing spectral contrast of reststrahlen bands in spectra of powdered minerals, *Icarus*, *96*(1), 121-128.

Salisbury, J. W., A. Wald, and D. M. D'Aria (1994), Thermal-infrared remote sensing and Kirchhoff's law: 1. Laboratory measurements, *Journal of Geophysical Research: Solid Earth (1978–2012)*, *99*(B6), 11897-11911.

Sharkov, E. A. (2003), *Passive microwave remote sensing of the Earth: physical foundations*, Springer.

Song, E., J. L. Bandfield, P. G. Lucey, B. T. Greenhagen, and D. A. Paige (2013), Bulk mineralogy of lunar crater central peaks via thermal infrared spectra from the Diviner Lunar Radiometer: A study of the Moon's crustal composition at depth, *Journal of Geophysical Research: Planets*, *118*(4), 689-707.

Thomas, I., N. Bowles, B. Greenhagen, T. Glotch, K. Donaldson Hanna, M. Wyatt, J. Bandfield, and D. Paige (2010), Emission measurements of lunar analogues for interpretation of returning data from the Diviner Lunar Radiometer on NASA's Lunar Reconnaissance Orbiter, paper presented at Lunar and Planetary Institute Science Conference Abstracts.

Yamamoto, S., et al. (2010), Possible mantle origin of olivine around lunar impact basins detected by SELENE, *Nature Geosci*, *3*(8), 533-536.

Yamamoto, S., et al. (2012), Olivine-rich exposures in the South Pole-Aitken Basin, *Icarus*, *218*(1), 331-344.

Chapter 2: Modeling scattering properties and mid-infrared emissivity of wavelength-sized particles: silica spheres as a test case

This chapter is a preliminary manuscript that will be submitted to Journal of Geophysical Research—Planets. Some of this material has been presented at the 43rd Lunar and Planetary Science Conference.

Arnold, J.A., T.D. Glotch, and M.J. Wolff (2012). Exact calculations of the scattering properties of wavelength-sized particles. 43rd Lunar and Planetary Science Conference, Abstract #2529.

"The light... it's strange out here, isn't it? It's kind of like, it doesn't, it doesn't scatter quite right."— Daniel Faraday from Lost

2.1 Introduction

Radiative transfer (RT) treats all media, whether a soil, regolith or cloud, as discrete particles, whose individual scattering properties can be used to describe the bulk material. As pointed out by *Mishchenko* [2008], the incoming electromagnetic radiation does not "see" distinct particles, but one complex scatterer, and therefore, where possible, a direct solution to Maxwell's equations is best. However, due to computational limitations, this is not always practical. Hence, approximate models are often used to describe special cases.

At present, such approximate scattering models are not fully able to replicate the dependence of mid-IR emissivity spectra of regolith-type surfaces on particle size. This shortcoming limits our interpretations of mineralogical composition and abundance on planetary surfaces. Here, we test whether using a T-matrix model [*Mackowski and Mishchenko*, 1996] that calculates scattering properties from an exact solution to Maxwell's equations for groups of spheres, provides input parameters that improve models of mid-infrared (mid-IR) emissivity spectra. The

T-matrix derived scattering parameters are input into three different approximate RT emissivity models and compared with spectra modeled using Mie single scattering coupled with the same RT models.

Mie/Hapke, along with other Mie/RT hybrid emissivity models, depend on Mie's single-scattering solution, which describes the scattering of electromagnetic radiation using the solution to Maxwell's equations for a plane-wave incident on a single, isolated sphere [*Mie*, 1908]. Mie scattering can be used to determine two of the basic inputs needed in a RT model: the single scattering albedo (w) and the asymmetry parameter (g). The single scattering albedo is the ratio of the scattered radiation to the sum of the scattered and absorbed radiation, while the asymmetry parameter describes, relative to the direction of incidence, whether radiation tends to scatter forwards or backwards. Single scattering ignores the mutual excitation of particles, and only considers the excitation from the external field [*Mishchenko*, 2008], so that the observed radiation has only interacted with one particle. For the single-scattering approximation to be valid, particles must be well separated. *Van de Hulst* [1957] gives a value for separation distance of at least three sphere radii, however *Mishchenko et al.* [2007] finds much larger separations are necessary for the single scattering approximation to be valid. This criterion is satisfied in low-density media, such as atmospheric aerosols [e.g. *Wolff and Clancy*, 2003], but not within a planetary regolith, where particles are typically not separated. There are two methods to correct Mie theory for close packing: diffraction subtraction [*Wald and Salisbury*, 1995] and structure factor correction [*Mishchenko and Travis*, 1994; *Mishchenko et al.*, 1997]. These corrections work well when particle sizes are substantially larger than the wavelength of the incident radiation; however they break down for small particle sizes. For example, *Moersch and*

Christensen [1995] point out that for particle size less than ~7% of wavelength, diffraction subtraction causes the modeled single scattering albedo to be negative.

Moersch and Christensen [1995] evaluated four different radiative transfer (RT) models in comparison to measured emission spectra of fine-grained quartz. None of these models adequately reproduce the measured spectra however, the Mie/Hapke hybrid model [*Hapke*, 1993] comes closest to reproducing changes in IR spectra with particle size. Even this model underestimates changes in emissivity with particle size for the strongest bands. Mustard [*Mustard and Hays*, 1997] used Mie/Hapke reflectance to model olivine and quartz grains <25 μm in size, representing the finest fraction of the lunar and martian regoliths. This was largely successful in the case of olivine, where modeled spectra generally reproduced the changes in spectral contrast with particle size as well as changes in major spectral features such as the widening of the CF with decreasing particle size. For quartz, however, the spectral contrast of the modeled spectra were overestimated, with the largest discrepancies occurring between 7.3μm and 9.5μm, just long-ward of the Christiansen feature (an emissivity maximum/reflectance minimum that occurs in the mid-IR where the index of refraction of a substance approaches that of the surrounding medium). *Mustard and Hays* [1997] concluded that the model may break down due to the large values of n and k quartz exhibits in this region. *Pitman et al.* [2005] concentrated on improving models of quartz emissivity and introduced a more thorough treatment of particle packing by using a discrete-ordinate/multi-stream method. This method breaks up the sphere of possible propagation directions into several parts, and integrates the equation of radiative transfer over each part, whereas a 2-stream approximation only considers two directions. The emissivity model of *Pitman et al.* [2005] also included a better

characterization of grain size distribution. Despite these improvements, there are still significant discrepancies between model and laboratory quartz spectra, especially in the 7-9.5 μm region.

In this work, we replace Mie scattering with the T-matrix approach to look at the average scattering properties of clusters containing large numbers of particles. This method, based on the direct computation of solutions to Maxwell's equations, is able to rigorously account for multiple scattering [*Mishchenko et al.*, 1996] of closely-packed particulates. The T-matrix relates the incident radiation to the scattered radiation and depends solely on the intrinsic properties of the scattering material (shape, size, refractive index) and orientation with respect to the coordinate system, rather than the incident or reflected field. This allows for rapid calculation of scattering properties over a many different illumination angles [*Mishchenko et al.*, 2002].

In addition to multiple scattering, there are three issues that can cause departure of measured emission spectra from theory: 1) particle shape, 2) packing, and 3) size distribution. These parameters are not trivial to determine in a finely particulate mineral sample. For comparison of measured and modeled spectra, we used mono-disperse (i.e. uniformly-sized) silica spheres to eliminate ambiguity due to shape and size distribution.

2.2 Radiative transfer models

2.2.1 Mie scattering

The Mie scattering model requires as input the sphere size parameter $x = \pi D/\lambda$, where D is the particle diameter and λ is the wavelength of incident light, and the complex index of refraction $\tilde{n} = n + ik$. From these, the single scattering albedo w, phase function $p(\theta)$, where θ is the scattering angle, and the asymmetry parameter $g=\langle cos\theta \rangle$ can be calculated. The notation for the asymmetry parameter can be confusing as Hapke uses g to denote the phase angle, π-θ, and ξ

for the asymmetry parameter [*Hapke*, 2012]. Here we will simply write out <cosθ> to avoid ambiguity. The extinction (Q_{ext}), scattering (Q_{sca}) and absorption (Q_{abs}) coefficients must satisfy the condition that the total extinction efficiency equals the sum of the scattering and absorption efficiencies: $Q_{ext}=Q_{sca}+Q_{abs}$. Single scattering albedo is defined as the scattering efficiency divided by the total extinction ($w=Q_{sca}/Q_{ext}$). The phase function $p(\theta)$, sometimes expressed in terms of p(cos θ), describes how incident radiation is scattered by the particle as a function of angle, hence if the particle is isotropic (equal scattering in all directions) $p(\theta)=1$. The asymmetry parameter is the average value of cosθ weighted by the phase function, $< cos\theta >= \frac{1}{2}\int_{-1}^{1} p(\theta)cos\theta d(cos\theta)$ (2.1). This value will be positive if the particle is forward-scattering and negative if it is back-scattering. A comprehensive derivation of Mie scattering is given in Bohren and Huffman (1983). For both the *Hapke* [1993] and *Conel* [1969] Mie/RT and T-matrix/RT hybrid models, we use *Wald's* [1995] correction to the single scattering albedo. $w_d = 2w - 1$ for close-packed particulates. The *Wald* [1995] correction is based on the assumption that the maximum extinction efficiency approaches 2 for particles much larger than wavelength, but it approaches 1 for smaller particulates.

2.2.2 Mie/Hapke hemispherical emissivity

An approximate emissivity model that, along with ignoring reflected radiation, assumes isotropic scattering and emission is outlined in *Hapke* [1993]. In this case, emissivity depends only on *w* and the emission angle μ:

$\varepsilon = \int_{\Omega} \gamma H(w,\mu)\, d\Omega$ (2.2)

where $\gamma = \sqrt{1-w}$, $H(w, \mu)$ is the H-function from *Chandrasekhar* [1960], and Ω is the detector's field of view. Integrating this equation over the upper hemisphere, and using an approximate form of the H-function results in a simplified equation for hemispherical emissivity:

$\varepsilon_h \approx \frac{2\gamma}{1+\gamma}\left(1+\frac{1}{6}r_0\right)$ (2.3a), where $r_0 = \frac{(1-\gamma)}{(1+\gamma)}$ (2.3b)

Two time-independent models for hemispherical emissivity are given in *Hapke* [1996] and Chapter 16 of *Hapke* [2012]. One is for a surface heated by incident sunlight, and the second is for a medium heated from below. In this work we only assess the latter, since it approximates the laboratory setting more realistically. In the heating from below case, emissivity is:

$\varepsilon = \frac{2\gamma}{\zeta+\gamma}$ (2.4)

where $\zeta = \sqrt{1-\beta w}$, which depends on the hemispherical asymmetry (β), a parameter normally used in the two-stream approximation [*Hapke* 1993)], where uniform radiance is incident on the particle from an entire hemisphere. The phase function is integrated over a hemisphere with latitude and longitude angles Λ and L, respectively, for all scattering angles (θ).

$\frac{1+\beta}{2} = \int_{\vartheta=0}^{\pi/2}\cdot\int_{L=-\pi/2}^{\pi/2}\cdot\int_{\Lambda=0}^{\pi}\frac{p(\cos(\theta+\Lambda)cosL)}{4\pi}cosLdLd\Lambda cos\theta d\vartheta$. (2.5)

The hemispherical asymmetry parameter is defined so that the radiation scattered back into the hemisphere it originated from is $\frac{1-\beta}{2}$ and the fraction scattered forward is $\frac{1+\beta}{2}$. The cosine asymmetry parameter is occasionally used as an approximation of β [*Hapke*, 1993; *Kinch et al.*, 2007], so that $\zeta = \sqrt{1-<cos\theta>w}$. We use this estimate when evaluating *Hapke* [1996].

2.2.3 Mie/Conel

Conel [1969] is a model developed for powdered silicate spectra based on a cloud-like atmospheric model. This was the first formulation to couple a RT approximation for multiple scattering with parameters calculated from Mie's solution. A series of simplifying assumptions to the RT equation of *Chandrasekhar* [1960], gives the following equation for emissivity:

$\varepsilon = \frac{2}{u+1}$ (2.6a), where $u^2 = (1-w\frac{<cos\vartheta>}{3})/(1-w)$ (2.6b).

These assumptions include a phase function that can be expressed as a Legendre polynomial and a two-stream approximation.

2.2.4 Multiple scattering T-matrix method (MSTM)

Like Mie scattering, the T-matrix method, also called the extended boundary condition method (EBCM), gives the scattering efficiencies (Q_{ext},Q_{sca},Q_{abs}), the cosine asymmetry parameter <cosθ>, along with the scattering matrix. The scattering matrix relates the Stokes vectors of the incoming and outgoing E-field and allows for the calculation of other parameters such as the phase function, which for unpolarized light is F_{11} [*Kokhanovsky*, 2006]:

$$\begin{pmatrix} I_{sc} \\ Q_{sc} \\ U_{sc} \\ V_{sc} \end{pmatrix} = \frac{\lambda^2}{4\pi^2 D^2} \begin{pmatrix} F_{11} & F_{12} & F_{13} & F_{14} \\ F_{21} & F_{22} & F_{23} & F_{24} \\ F_{31} & F_{32} & F_{33} & F_{34} \\ F_{41} & F_{42} & F_{43} & F_{44} \end{pmatrix} \begin{pmatrix} I_{inc} \\ Q_{inc} \\ U_{inc} \\ V_{inc} \end{pmatrix} \quad (2.7).$$

Here, λ is wavelength and D is the distance between the source and the detector. The Stokes vectors describe the polarization of the scattered (subscript sc) and incident (subscript inc) beams. The total flux of the beam is related to I, the direction of linear polarization is described by Q and U, and circular polarization in described by V. The elements of the scattering matrix (F_{ij}) depend on the scattering angle (θ). Instead of a single spherical particle as in Mie scattering, the T-matrix method can be used to calculate these parameters for any radially symmetric particle as well as groups of particles.

Mishchenko et al. [2007] used this method to examine the scattering properties of sphere clusters of increasing density. A spherical volume element of fixed radius was filled with randomly-distributed wavelength-sized particles. The number of particles within the volume element was varied to give packing densities of 0.1%-24%. At low density, the results of the T-matrix method are in agreement with standard RT models, while the onset of multiple-scattering effects becomes apparent at higher density (Figure 2.1).

2.3 Materials and Methods

2.3.1 MSTM and Mie codes

The Multiple Sphere T Matrix (MSTM) Fortran package developed by D. Mackowski, which is available at (http://eng.auburn.edu/users/dmckwski/scatcodes/), calculates the scattering properties of clusters of spherical particles [*Mackowski and Mishchenko*, 1996] in a similar manner to *Mishchenko* [2007], described earlier. Mie scattering properties were calculated using a code written for Matlab by *Mätzler* [2002], based on the Fortran code in the appendix of the light scattering textbook by *Bohren and Huffman* [1983]. Similar to Mie scattering, the input parameters needed for MSTM are the relative positions and sizes of the spheres and their indices of refraction. Due to computational limitations, the number of spheres per volume element was adjusted for each sphere diameter that we modeled (see Table 2.1). The packing fraction of the 2, 19, and 49 μm spheres was kept close to 0.6, however the packing fraction of the 179 μm cluster is lower when defined relative to the volume of its surrounding sphere, since there were only 4 spheres in this cluster. To generate a random close packing of particles within a spherical volume (example, Figure 2.2) element as in *Mishchenko* [2007], we utilized a molecular dynamics – based Fortan program [*Donev et al.*, 2005] available at [http://cims.nyu.edu/~donev/Packing/PackLSD/Instructions.html].

2.3.2 Computing resources

To run the MSTM code we utilized the Pleiades cluster housed at the NASA Advanced Supercomputing (NAS) facility at NASA Ames Research Center along with recently decommissioned New York Blue/P supercomputer at Brookhaven National Laboratory. The

Pleiades cluster has several node types. We primarily used the Sandy Bridge and Westmere nodes for this work, which have 1,872 and 3,840 available nodes, respectively, each with 2GB of memory per core. NY Blue/P had up to 512 nodes available for a given job, with 2GB of memory per node.

2.3.3 Silica spheres: description, mid-IR emissivity measurements and optical constants

To minimize the variables of particle size and shape, we used mono-disperse silica spheres for our laboratory emissivity measurements. The silica spheres, from Fischer scientific, are highly uniform calibration standards whose size distribution has been measured with optical microscopy. Information on the size distributions of each diameter is given in Table 2.2. Throughout the text, we will refer to the nominal diameters. We analyzed four size fractions: 2μm 19μm, 49μm, and 179μm.

Mid-IR silica optical constants were calculated using dispersion theory, following the method of *Spitzer and Kleinman* [1961] in the range of 400-1700 cm^{-1}. Using this model, dispersion oscillator parameters were obtained from iterative fits of a silica reflectance spectrum. To acquire this spectrum, several grains of the largest sphere size (179 μm) were mounted on a slide and polished to obtain a flat surface. The specular reflectance of a polished grain surface was measured with a Nicolet iN10 micro-FTIR microscope., with a 25μm spot size. Although, we cannot polarize the incident beam with this instrument, it is not necessary, since silica is optically isotropic. Figure 2.3 shows the modeled real and imaginary indices of refraction (*n*, *k*).

We acquired MIR emissivity spectra (350 cm^{-1}-2000 cm^{-1}) of the four different sizes of the silica spheres with a Nicolet 6700 FTIR spectrometer, using a CsI beamsplitter and a deuterated L-alanine doped triglycine sulfate (DLaTGS) detector in an atmosphere purged of CO_2 and H_2O.

Spectra were calibrated using separate measurements of a black-body heated at two different temperatures in the manner of *Ruff et al.* [1997]. We chose wavelengths for MSTM modeling based on the emissivity features of silica within the wavelength range of measured optical constants.

2.4 Results

Comparison of emissivity spectra produced from Mie versus MSTM inputs for *Conel* [1969] is given is Figure 2.4. The same comparison for *Hapke's* [1993] hemispherical emissivity model, assuming isotropic scattering and emission is given in Figure 2.5. In these cases, the single scattering albedos derived using Mie and MSTM models require diffraction subtraction to produce overall emissivity values that match the measured data. As found by other workers [*Cheng et al.*, 2010; *Wald and Salisbury*, 1995], who investigated quartz and snow, respectively, without this correction, the shape of the absorptions are very similar to those of the measured spectra, but the overall emissivity is low compared to the measured emissivity. See Figure 2.6 for an example of the *Hapke* [1993] hemispherical emissivity model without this correction.

Figure 2.7 shows Mie/*Hapke* [1996] and MSTM/*Hapke* [1996] hybrid models for hemispherical emissivity, assuming heating from below. In neither case do the single scattering albedos require the correction of *Wald* [1995] to produce emissivity values close to unity.

2.5 Discussion

There are a couple trends seen in the modeled spectra of the two smaller sphere sizes for all of the RT models tested. First, all Mie/RT and MSTM/RT models have a deep band at ~700 cm^{-1} for the 2 μm sphere size that is not present in the measured spectrum. Second, all Mie/RT models

over-estimate the band depth of the broad, shallow ~720 cm^{-1} feature of the 19 μm sphere size, while the MSTM/RT models are a much better fit to the measured values in this region. Overall MSTM derived scattering parameters do more to improve modeled emissivity for the 19 μm than the 2 μm sphere size. It may be that the overall size parameter of the volume element determines the improvement in the single scattering albedo values. The size of the 19 μm particle cluster (~159 μm) was much larger than any of the wavelengths modeled and sufficient to produce realistic values, but even with 967 spheres, the 2μm particle cluster only had a ~23 μm diameter, which is comparable to mid-IR wavelengths. The number of spheres required for a much larger overall diameter is computationally prohibitive at this time, as runtime scales with number of spheres squared.

Generally, the *Hapke* [1993] and *Conel* [1969] models produce similar calculated emissivity spectra. Both models over-estimate the 720 cm^{-1} feature of the 19 μm sphere size as well as the ~850cm^{-1} band of the 2 μm sphere size. Additionally, the latter band is shifted to ~800 cm^{-1}. Excluding the 2μm spheres, changes in spectral contrast with particle size in the 1050 cm^{-1} region are commensurate with the measured spectra. While an improvement, MSTM-derived single scattering albedos still underestimate the overall emissivity without correction when used as input for the *Hapke* [1993] and *Conel* [1969] models. However, when diffraction subtraction is used with MSTM derived single scattering albedos, the modeled spectrum of the smallest particle size (2 μm) is reasonable, whereas the Mie/RT scattering models break down. For these models, diffraction subtraction boosts the overall emissivity of the 19μm, 49μm and 179μm sizes closer to measured values, but gives emissivity greater than 1 throughout most of the Mie/RT modeled spectra of the 2μm sphere size. Additionally, diffraction subtraction produces modeled

emissivity values greater than 1 for the 19μm sphere size using both the MSTM/*Hapke*[1993] and MSTM *Conel*[1969] models.

The *Hapke* [1996] model gives the most reasonable emissivity values for the smallest particle size, and surprisingly does not require any correction to either the Mie- or MSTM-derived single scattering albedos. It reproduces the Christiansen feature, an emissivity maximum that is not dependent on particle size. The Mie/*Hapke* [1996] model gives the best fit for the 179μm particle size, but changes in spectral contrast with sphere diameter are muted compared with the measured values. MSTM/*Hapke* [1996] most closely replicates the variations in spectral contrast with particle size while at the same time giving more realistic overall emissivity values for the 2μm spheres. Moreover, using this model, the 2um sphere emissivity is improved in the higher-wavenumber portion of the spectrum, where the size parameter of the cluster is larger compared to wavelength.

2.6 Conclusions

The surfaces of airless solar system bodies are largely made up of particulates generated by impact and space weathering processes. In order to interpret remote sensing data of these bodies, models that are able to predict emissivity spectra of small particle sizes are needed. Since at mid-IR wavelengths emissivity spectra vary with particle size, it is important to be able to model these changes in order to separate this effect from compositional differences. Studies that modeled emissivity using Mie single scattering parameters with RT, cite the need for a more realistic treatment of close-packed particles [*Moersch and Christensen*, 1995; *Mustard and Hays*, 1997; *Pitman et al.*, 2005].

The single scattering assumption that goes into Mie/RT hybrid models is not suitable for planetary surfaces where particles are not well separated. Scattering parameters (*w* and <cosθ>) derived from a multiple scattering T-matrix method rather than Mie scattering improve the agreement between measured and modeled emissivity spectra, especially for the smallest particles sizes. All RT models are considerably improved for the 19 μm particle size using MSTM inputs. While the 2 μm models show some improvement in the 900-1300 cm^{-1} region, the regions near 700 cm^{-1} and 400-500 cm^{-1} are still problematic. This is likely due to the relatively small size of the volume element, which is wavelength-scale, causing some of the same problems inherent in the Mie single scattering assumption. The MSTM/*Hapke* [1993] and MSTM/*Conel* [1969] models over-estimate the emissivity of the larger particles compared with their two respective Mie/RT models, however this is not the case with the MSTM/*Hapke* [1996] model spectra.

Of the three MSTM/RT hybrid models tested, the hemispherical emissivity from *Hapke* [1996] is the only one that both captures the changes in emissivity with particle size and is able to reasonably model the smallest particle size. One potential avenue for improving the performance for the smallest sphere diameter is to try relaxing the density of the cluster to get an overall larger volume size parameter with the same number of spheres.

References

Bohren, C. F., and D. R. Huffman (1983), *Absorption and scattering of light by small particles*, John Wiley & Sons.

Chandrasekhar, S. (1960), Radiative Transfer, *Dover*.

Cheng, J., S. Liang, F. Weng, J. Wang, and X. Li (2010), Comparison of radiative transfer models for simulating snow surface thermal infrared emissivity, *Selected Topics in Applied Earth Observations and Remote Sensing, IEEE Journal of*, *3*(3), 323-336.

Conel, J. E. (1969), Infrared emissivities of silicates: Experimental results and a cloudy atmosphere model of Spectral emission from condensed particulate mediums, *Journal of Geophysical Research*, *74*(6), 1614-1634.

Donev, A., S. Torquato, and F. H. Stillinger (2005), Neighbor list collision-driven molecular dynamics simulation for nonspherical hard particles.: II. applications to ellipses and ellipsoids, *Journal of Computational Physics*, *202*(2), 765-793.

Hapke, B. (1993), Introduction to the Theory of reflectance and Emission Spectroscopy, edited, Cambridge University Press, New York.

Hapke, B. (1996), A model of radiative and conductive energy transfer in planetary regoliths, *Journal of Geophysical Research: Planets (1991–2012)*, *101*(E7), 16817-16831.

Hapke, B. (2012), *Theory of reflectance and emittance spectroscopy*, Cambridge University Press.

Kinch, K. M., J. Sohl-Dickstein, J. F. Bell, J. R. Johnson, W. Goetz, and G. A. Landis (2007), Dust deposition on the Mars Exploration Rover Panoramic Camera (Pancam) calibration targets, *Journal of Geophysical Research: Planets*, *112*(E6), E06S03.

Kokhanovsky, A. A. (2006), *Light Scattering Reviews: Single and Multiple Light Scattering*, Springer.

Mackowski, D. W., and M. I. Mishchenko (1996), Calculation of the< i> T</i> matrix and the scattering matrix for ensembles of spheres, *JOSA A*, *13*(11), 2266-2278.

Mätzler, C. (2002), MATLAB functions for Mie scattering and absorption, version 2, *IAP Res. Rep*, *8*.

Mie, G. (1908), Beiträge zur Optik trüber Medien, speziell kolloidaler Metallösungen, *Annalen der physik*, *330*(3), 377-445.

Mishchenko, M. I. (2008), Multiple scattering, radiative transfer, and weak localization in discrete random media: unified microphysical approach, *Reviews of Geophysics*, *46*(2).

Mishchenko, M. I., and L. D. Travis (1994), Light scattering by polydispersions of randomly oriented spheroids with sizes comparable to wavelengths of observation, *Applied Optics*, *33*(30), 7206-7225.

Mishchenko, M. I., L. D. Travis, and D. W. Mackowski (1996), < i> T</i>-matrix computations of light scattering by nonspherical particles: A review, *Journal of Quantitative Spectroscopy and Radiative Transfer*, *55*(5), 535-575.

Mishchenko, M. I., L. D. Travis, and A. A. Lacis (2002), *Scattering, absorption, and emission of light by small particles*, Cambridge university press.

Mishchenko, M. I., L. Liu, and G. Videen (2007), Conditions of applicability of the single-scattering approximation, *Opt. Express*, *15*(12), 7522-7527.

Mishchenko, M. I., L. D. Travis, R. A. Kahn, and R. A. West (1997), Modeling phase functions for dustlike tropospheric aerosols using a shape mixture of randomly oriented polydisperse spheroids, *Journal of Geophysical Research: Atmospheres (1984–2012)*, *102*(D14), 16831-16847.

Moersch, J., and P. R. Christensen (1995), Thermal emission from particulate surfaces: A comparison of scattering models with measured spectra, *Journal of Geophysical Research: Planets (1991–2012)*, *100*(E4), 7465-7477.

Mustard, J. F., and J. E. Hays (1997), Effects of hyperfine particles on reflectance spectra from 0.3 to 25 μm, *Icarus*, *125*(1), 145-163.

Pitman, K. M., M. J. Wolff, and G. C. Clayton (2005), Application of modern radiative transfer tools to model laboratory quartz emissivity, *Journal of Geophysical Research: Planets (1991–2012)*, *110*(E8).

Ruff, S. W., P. R. Christensen, P. W. Barbera, and D. L. Anderson (1997), Quantitative thermal emission spectroscopy of minerals: A laboratory technique for measurement and calibration, *Journal of Geophysical Research: Solid Earth (1978–2012)*, *102*(B7), 14899-14913.

Spitzer, W., and D. Kleinman (1961), Infrared lattice bands of quartz, *Physical Review*, *121*(5), 1324.

Van de Hulst, H. (1957), Light scattering by small particles.

Wald, A. E., and J. W. Salisbury (1995), Thermal infrared directional emissivity of powdered quartz, *Journal of Geophysical Research: Solid Earth (1978–2012)*, *100*(B12), 24665-24675.

Wolff, M. J., and R. T. Clancy (2003), Constraints on the size of Martian aerosols from Thermal Emission Spectrometer observations, *Journal of Geophysical Research: Planets*, *108*(E9), 5097.

Tables and Figures

Table 2.1. Number of spheres and volume element size for MSTM models of silica sphere clusters.

Nominal diameter	Number of spheres in volume element	Volume element diameter
2 µm	967	23.1 µm
19 µm	500	159.3 µm
49 µm	150	309.5 µm
179 µm	4	463.µm

Table 2.2. Information on sphere diameters and size distributions for silica spheres used in laboratory emissivity measurements.

Nominal diameter	Mean diameter	Size distribution: standard deviation (σ) and coefficient of variation (CV)
2 µm	2.0µm ± 0.4µm	σ = 0.6µm, 30% CV
19 µm	19.3µm ± 1.0µm	σ = 1.9µm, 9.8% CV
49 µm	49.0µm ± 1.4µm	σ = 2.4µm, 4.9% CV
179 µm	179µm ± 3.7µm	σ = 9.3µm, 3.3% CV

Figure 2.1. Phase functions (the F_{11} element of the scattering matrix) of a fixed-volume filled with different numbers of spheres. The black line, showing one particle, represents single-scattering.

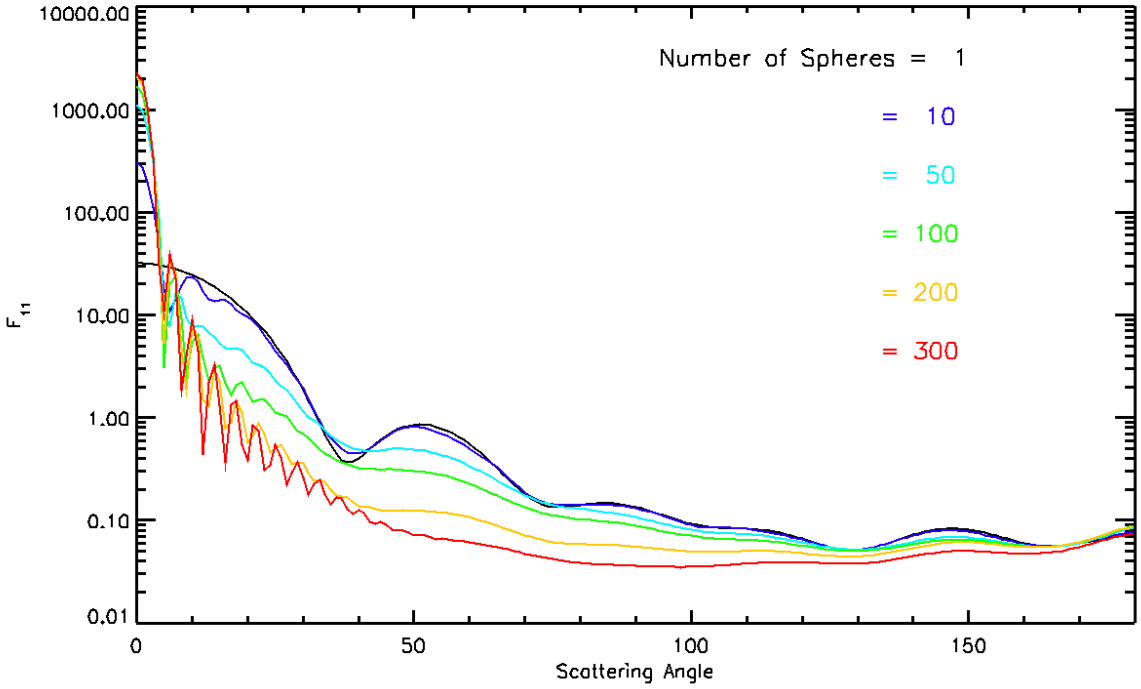

Figure 2.2. Example of sphere cluster modeled by MSTM code, with 967 spheres of 2μm diameter. Cluster is centered at x=y=z=0, where axes are in μm and shading is for visibility.

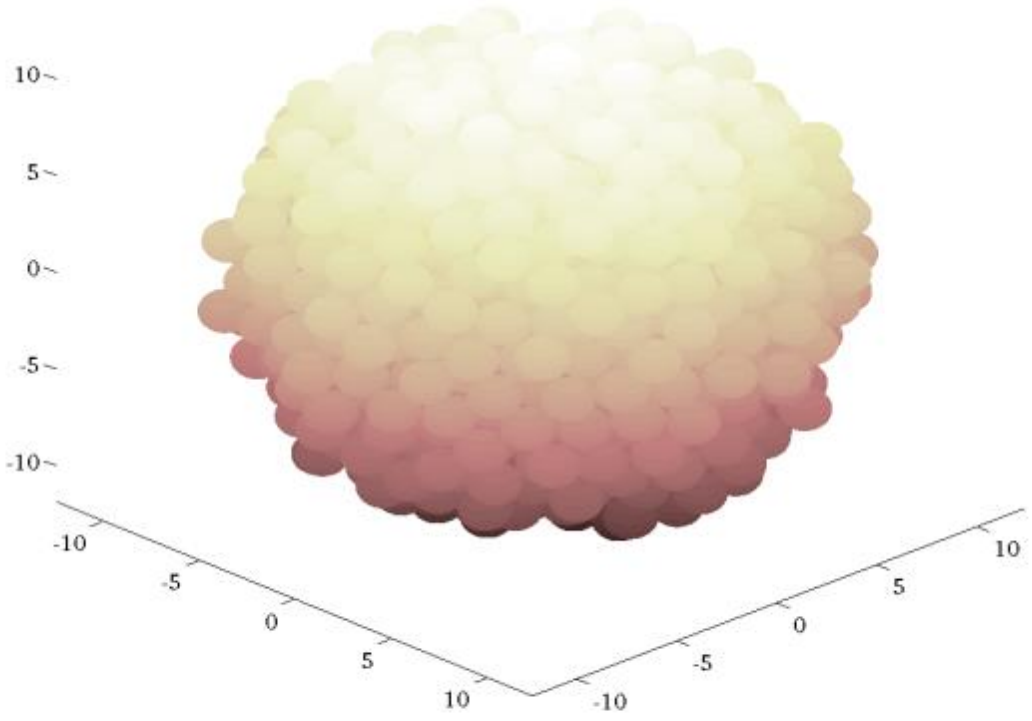

Figure 2.3. Silica optical constants derived from specular reflectance, input into both Mie and MSTM codes.

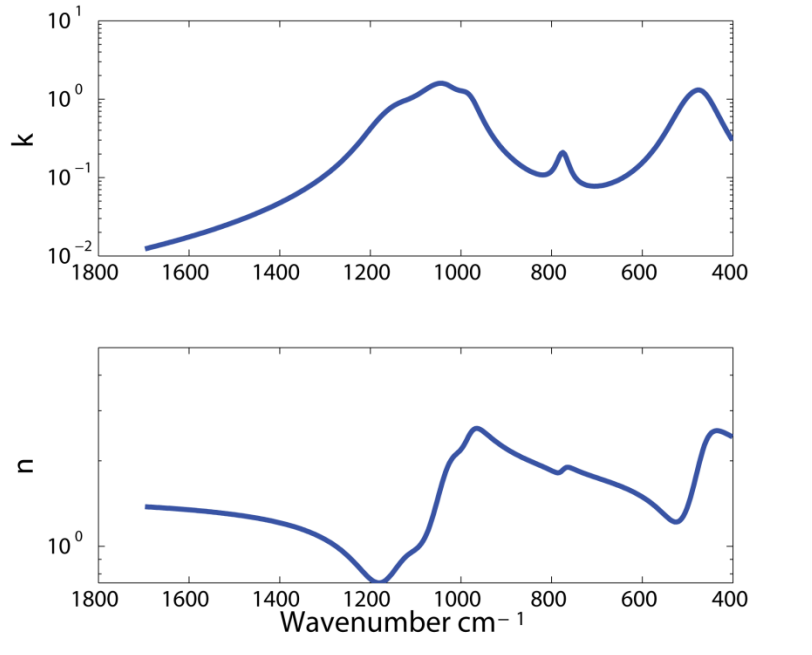

Figure 2.4. Left: Conel [1969] hemispherical emissivity model with Mie input parameters. Right: Conel [1969] hemispherical emissivity with MSTM input parameters. Laboratory spectra are shown as solid lines, while the modeled spectra are shown as dahed lines.

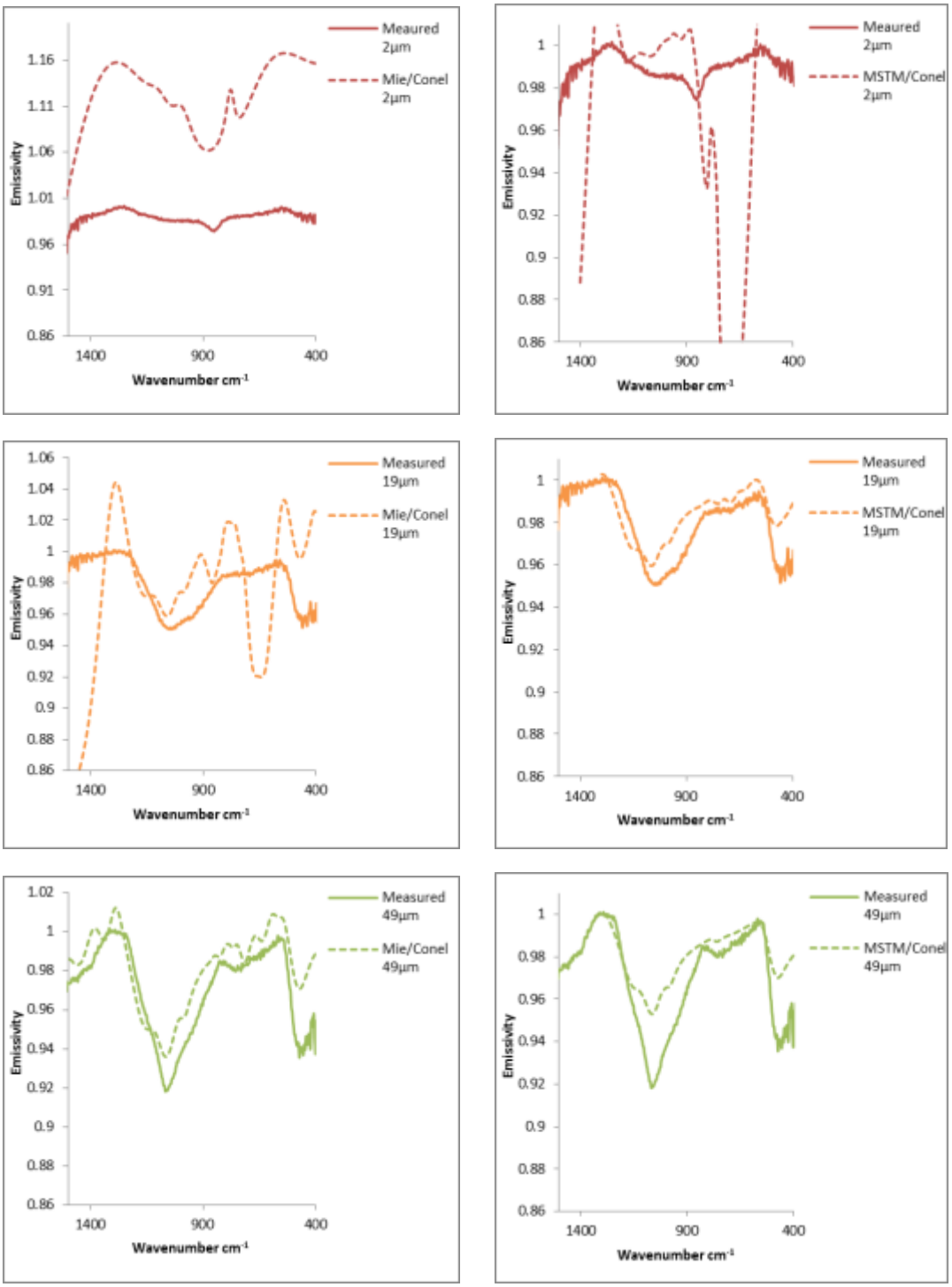

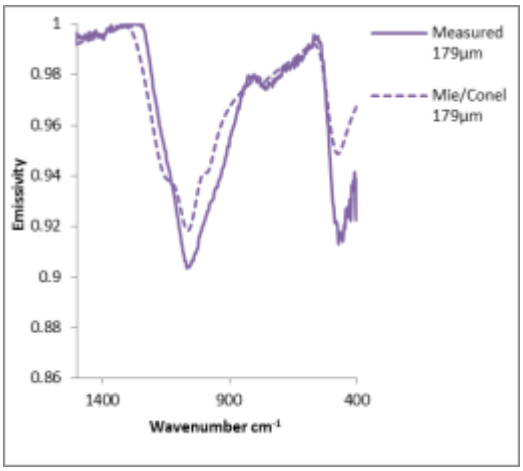
Measured 179µm
Mie/Conel 179µm
Emissivity
1
0.98
0.96
0.94
0.92
0.9
0.88
0.86
1400
900
400
Wavenumber cm-1

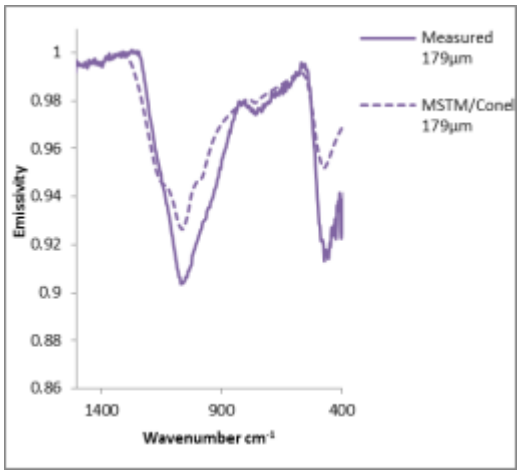
Measured 179µm
MSTM/Conel 179µm
Emissivity
1
0.98
0.96
0.94
0.92
0.9
0.88
0.86
1400
900
400
Wavenumber cm-1

Figure 2.5. Left: Hapke [1993] hemispherical emissivity model with Mie input parameters. Right: Hapke [1993] hemispherical emissivity with MSTM input parameters. Laboratory spectra are shown as solid lines, while the modeled specta are shown as dahed lines.

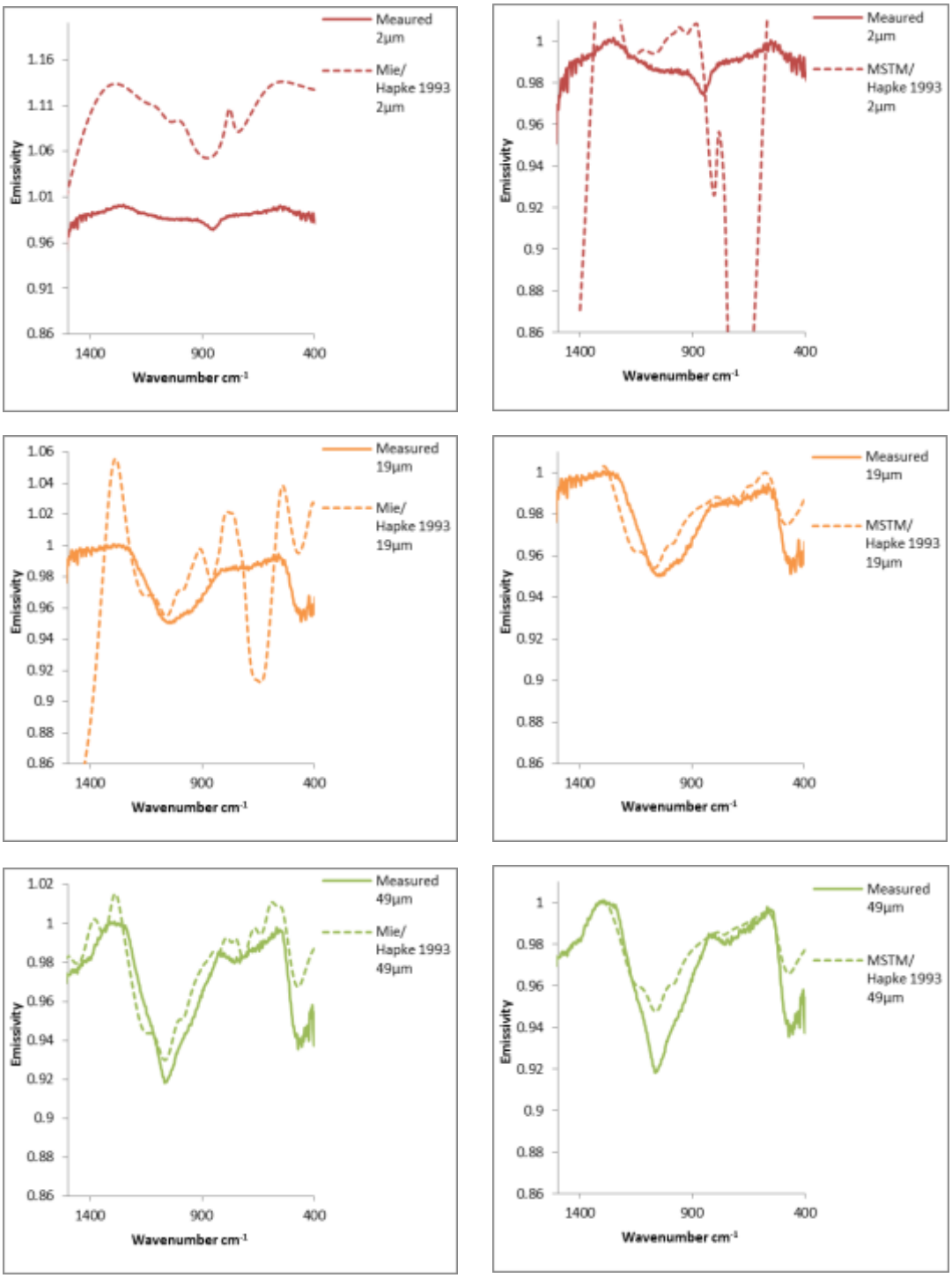

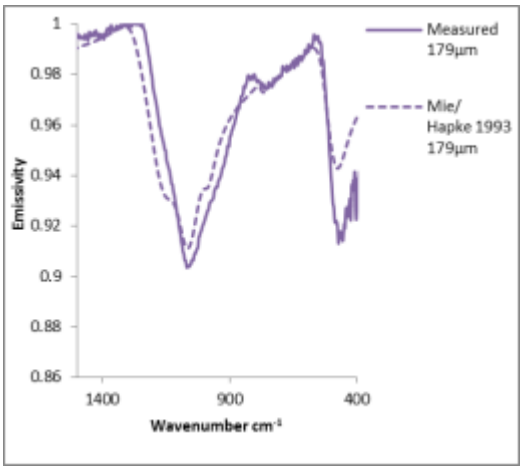
Measured
179µm
Mie/
Hapke 1993
179µm
Emissivity
1
0.98
0.96
0.94
0.92
0.9
0.88
0.86
1400
900
400
Wavenumber cm-1

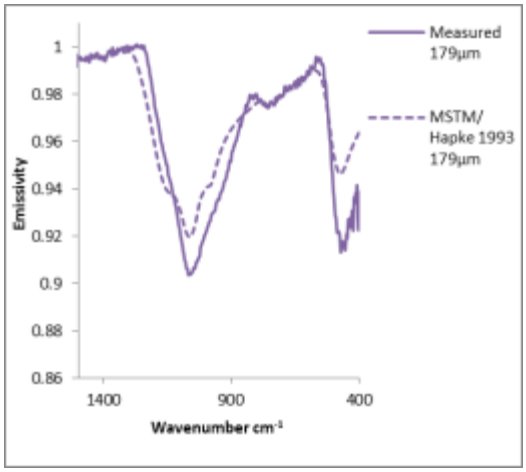
Measured
179µm
MSTM/
Hapke 1993
179µm
Emissivity
1
0.98
0.96
0.94
0.92
0.9
0.88
0.86
1400
900
400
Wavenumber cm-1

Figure 2.6. Mie/Hapke [1993] model vs. measured spectra with and without the Wald [1995] diffraction subtraction correction to single scattering albedo (*w*).

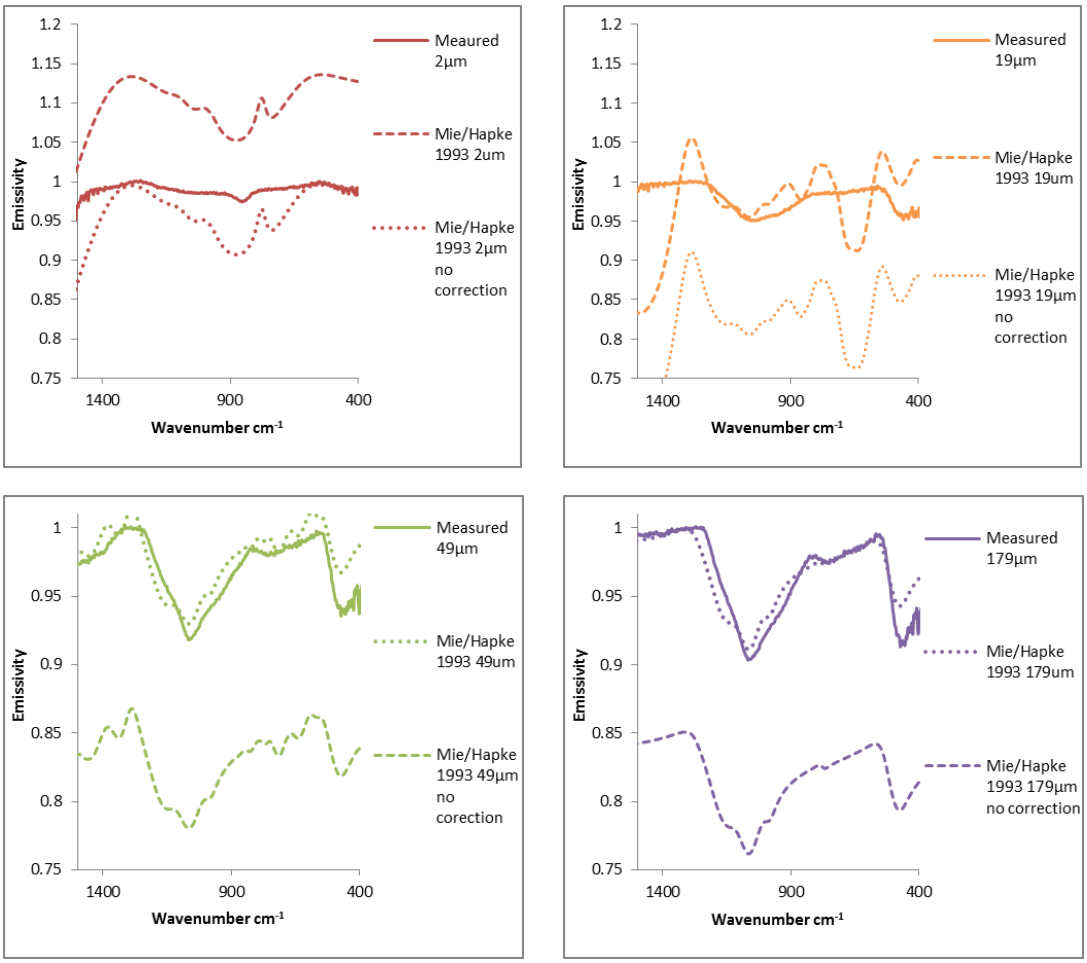

Figure 2.7. Left: Hapke [1996] hemispherical emissivity model with Mie input parameters. Right: Hapke [1996] hemispherical emissivity with MSTM input parameters. Laboratory spectra are shown as solid lines, while the modeled specta are shown as dahed lines.

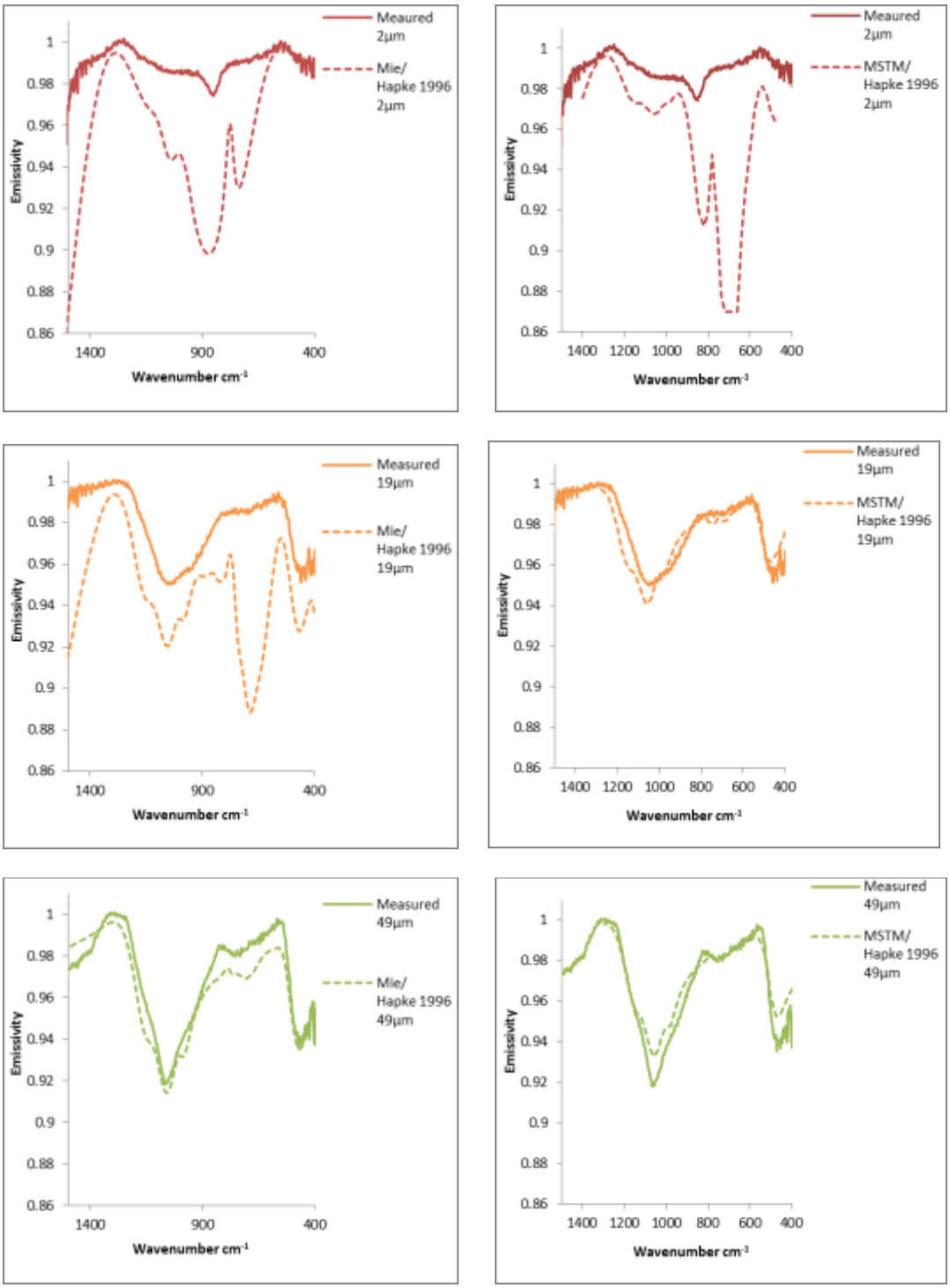

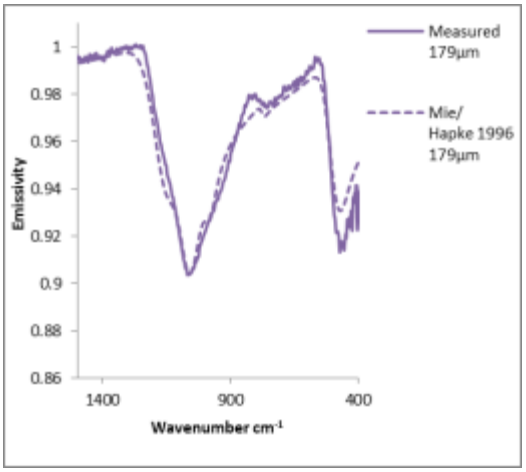
Measured 179µm
Mie/ Hapke 1996 179µm
Emissivity
1
0.98
0.96
0.94
0.92
0.9
0.88
0.86
1400
900
400
Wavenumber cm-1

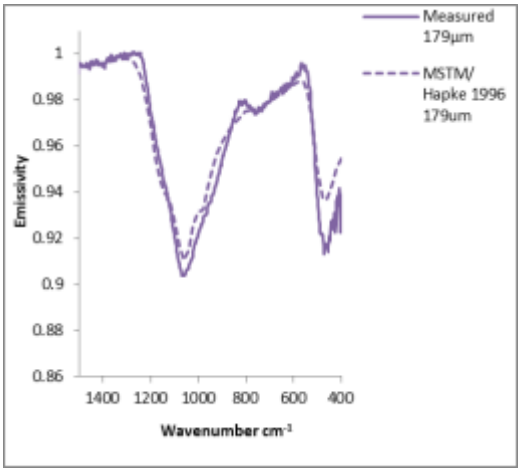
Measured 179µm
MSTM/ Hapke 1996 179um
Emissivity
1
0.98
0.96
0.94
0.92
0.9
0.88
0.86
1400
1200
1000
800
600
400
Wavenumber cm-1

Chapter 3: Mid-infrared optical constants of clinopyroxene and orthoclase derived from oriented single-crystal reflectance spectra

This Chapter is a re-formatted version of a paper submitted to American Mineralogist of the same name.

J.A. Arnold, T.D. Glotch, and A.M. Plonka (2014). *Mid-infrared optical constants of clinopyroxene and orthoclase derived from oriented single-crystal reflectance spectra, American Mineralogist, in press.*

"[I]t is nearly impossible to find a material for which n is not less than 1 at some frequencies. And these are not exotic materials. Try table salt." –Craig Bohren on common errors in physics textbook writing

3.1 Abstract

We have determined the mid-IR optical constants of one alkali feldspar and four pyroxene compositions in the range of 250–4000 cm^{-1}. Measured reflectance spectra of oriented single crystals were iteratively fit to modeled spectra derived from classical dispersion analysis. We present the real and imaginary indices of refraction (*n* and *k*) along with the oscillator parameters with which they were modeled. While materials of orthorhombic symmetry and higher are well-covered by the current literature, optical constants have been derived for only a handful of geologically relevant monoclinic materials, including gypsum and orthoclase. Two input parameters that go into radiative transfer models, the scattering phase function and the single scattering albedo, are functions of a material's optical constants. Pyroxene is a common rock-forming mineral group in terrestrial bodies as well meteorites and is also detected in cosmic dust.

Hence, having a set of pyroxene optical constants will provide additional details about the composition of solar system bodies and circumstellar materials. We follow the method of *Mayerhofer et al.* [2010], which is based on the Berreman 4x4 matrix formulation. This approach provides a consistent way to calculate the reflectance coefficients in low-symmetry cases. Additionally, while many models assume normal incidence to simplify the dispersion relations, this more general model applies to reflectance spectra collected at non-normal incidence.

3.2. Introduction

Pyroxenes are common rock-forming minerals in terrestrial planets and asteroids. They are also abundant in meteorites and interplanetary and cosmic dust particles. The pyroxene crystal structure allows for a variety of cations to occupy its M1 and M2 sites, with ordering and preference between the two sites being controlled by temperature, pressure, and cooling rate. As a result, pyroxene composition is a good indicator of the thermal history of the source magma [*Kilma et al.,* 2008[and can be used to compare the evolution of different planetary bodies [*Karner et al.,* 2006]. Pyroxene is readily detected in the near-infrared (NIR) via two strong Fe^{2+} crystal field absorption bands near 1 and 2 μm whose positions and strengths are functions of composition. As the mid-IR (MIR, around 3-15 μm, though definitions vary) is sensitive to Si–O vibrational modes [*Salisbury,* 1972], it can be used to provide additional details about composition as well as to estimate abundance relative to more felsic components [*Ramsey and Christensen,* 1998].

The wavelength-dependent complex index of refraction ($\tilde{n}=n+ik$), where n and k are the optical constants, is an essential input into scattering models of planetary surfaces. Commonly used radiative transfer models of airless bodies include *Lumme and Bowell* [1981], *Hapke* [1993a; 2012], *Shkuratov et al.* [1999] and *Mishchenko et al.* [1999]. Hapke's theory uses optical

constants to calculate the single scattering albedo and the phase function. In Skhuratov's model of lunar regolith scattering, the reflectance of the surface (A) is dependent on only four parameters $A(n,k,S,q)$, where n and k are the optical constants, S is the scattering path-length and q is the packing density [*Skhuratov* et al. 1999]. Hence, accurate determination of optical constants for a variety of minerals is necessary for using remote sensing data to make quantitative estimates of mineralogical composition. At MIR wavelengths, materials of orthorhombic symmetry and higher are well-covered by the current literature; these include quartz, calcite, olivine, orthopyroxene, kaolinite, serpentine, palagonite, and iron oxides *[Spitzer and Kleinman,* 1961; *Wenrich and Christensen,* 1996; *Lucy,* 1998; *Lane,* 1999; *Suto* et al., 2002; *Glotch et al,.* 2006; *Sogawa et al.,* 2006; *Dyar et al.,* 2009; *Roush et al.*1991; *Glotch and Rossman,* 2009].

Monoclinic and triclinic minerals have largely been ignored in optical constant research, although in some cases orientation-averaged effective optical constants have been calculated and presented (e.g., *Roush et al.* ,1991; *Glotch et al.,* 2007). This is due to the additional complexity of obtaining values for low-symmetry materials, despite the fact that these crystal systems contain important rock-forming mineral groups such as clinopyroxene and feldspar. In this work, we use dispersion analysis to calculate the optical constants of four distinct clinopyroxene compositions in the range of 250–4000 cm^{-1}, following the method of *Mayerhofer et al.* [2010] and present a procedure that can be applied to derive the optical constants of monoclinic single crystals. We also calculate the optical constants of orthoclase and compare to the previously computed optical constants of *Aronson* [1986] as a test of our model.

3.3. Background

3.3.1 The Moon

The Clementine mission provided a global lunar map of pyroxene abundance, broadly highlighting that it is a major component of the mare basalts and less prevalent in highlands. Modeled clinopyroxene concentrations are especially high in fresh mare craters due the short exposure ages of these surfaces [*Shkuratov et al*., 2004]. While pyroxene is only a minor component in the lunar highlands it is found in the following highlands rock types: ferroan anorthosites (FAN's), alkali- and Mg-suite rocks [*Tompkins and Pieters*, 1999]. Attempting to put these in a global context, *Klima et al.* [2011] used NIR data from the Moon Mineralogy Mapper (M^3) to detail the distribution of high− versus low-Ca pyroxene and estimate Mg #. Low-Ca pyroxene is limited to regional exposures within the South Pole-Aitken Basin and in the highlands north and south of Mare Frigoris, approximately half of which have Mg # (Mg/(Mg+Fe) commensurate with FAN rocks (~Mg # 55−75).

MIR emission data from the Diviner Lunar Radiometer Experiment complements visible near-IR (VNIR) measurements from Clementine and M^3, as they are able to detect Fe-poor lithologies in the presence of mafic materials such as pyroxene and olivine. Three of Diviner's channels are centered near the silicate Christiansen feature (CF) [*Paige et al.* 2010], which is an emissivity maximum whose position moves to shorter wavelengths with increasing SiO_2 polymerization [*Conel,* 1969; *Logan et al*., 1973; *Salisbury and Walter,* 1989], allowing Diviner to be used to map silicate compositions across the Moon [*Greenhagen et al*., 2010; *Glotch et al*., 2010, 2011; *Song et al*., 2013; *Allen et al*., 2011*; Arnold et al.*, 2013] A global map of CF position clearly demonstrates the difference between the relatively pyroxene-rich mare and feldspar-rich highlands [*Greenhagen et al.*, 2010]. Although Diviner has only three spectral

bands in the 8 μm range, laboratory measurements in a simulated lunar environment show the estimated CF position combined with spectral shape is adequate to distinguish pyroxene from a mixture of plagioclase and olivine [*Donaldson Hanna et al.*, 2012].

3.3.2 Mars

The low-albedo regions of Mars were initially categorized into two surface compositions based on Mars Global Surveryor Thermal Emission Spectrometer (MGS-TES) data, where Surface Type 1 was determined to be basalt containing ~25% clinopyroxene [*Bandfield et al.*, 2000; *Hamilton et al.*, 2001]. *Rogers et al.* [2007] defined 4 distinct spectral types within low-albedo terrains. Subsequently, *Rogers and Christensen* [2007] determined the mineralogy of these four groups, with clinopyroxene abundance being one of the major distinguishing features. While low-Ca pyroxenes were mostly detected in Noachian terrain, high-Ca pyroxene was found in a wider age-range of units. Some of the mineralogical differences between the four groups, especially high silica phases, are the result of weathering. However, the differences in pyroxene abundance likely represent differences in the magma from which the crust was derived. These differences were also identified with data from the OMEGA (Observatoire pour la Minéralogie, l'Eau, les Glaces et l'Activité) NIR imaging spectrometer. Using this instrument, *Ody et al.* [2012] presented global maps of anhydrous minerals, including pyroxene. The highest pyroxene concentration occurs in the Syrtis Major volcanic province, which is coincident with Group 2 of *Rogers and Christensen* [2007]. *Glotch and Rogers* [2013] suggested that the unusually high concentration of high-Ca pyroxene at this site was the result of subsurface interactions of basaltic magma and a Ca-carbonate-bearing layer.

3.3.3 Asteroids

Pyroxene has been identified in several S-type asteroid families [*Chapman et al*., 1975]. *Sunshine et al.* [2004] applied the Modified Gaussian Model (MGM) to VNIR asteroid spectra collected by the NASA Infrared Telescope Facility (IRTF), to determine the relative amounts of low- and high calcium pyroxene. They determined that the Vestoids and well as the S-type asteroid families Merxia and Agnia have a high ratio of high calcium pyroxene to total pyroxene, indicating that they are derived from differentiated bodies.

Pyroxene absorptions are the most common VNIR spectral feature on the surface of the asteroid Vesta, which was first linked to the HED (howardite-eucrite-diogenite) meteorites due to the similarity of their 0.9 μm band in VNIR spectra [*McCord et al.,* 1970]. The findings of Dawn's Visible InfraRed (VIR) mapping spectrometer support this connection. Much of the surface shows a howardite-like spectrum intermixed with smaller-scale regions resembling eucrites and diogenites. The south polar region (Rheasilvia), a large impact basin, is consistent with more Mg-rich pyroxene characteristic of diogenites [*De Sanctis et al*., 2012]. These spectral variations are indicative of a differentiated crust where the deeper diogenitic materials have been exposed through impact.

3.3.4 Interplanetary and Interstellar Dust

The presence of crystalline silicates in interplanetary dust particles (IDPs) was established through micrometeorite samples collected from Earth's stratosphere [*Bradley et al.,* 1983; *Mackinnon and Rietmeijer,* 1987]. Additionally, ground-based MIR spectra from three different instruments provided evidence for crystalline silicates in comets [*Hanner et al.,* 1994]. Prior to the Infrared Space Observatory (ISO), whose instruments covered a range of ~2.5 – 240 μm, silicates in cosmic dust were thought to be primarily amorphous [*Roush et al*., 1991; *Molster and Kemper,* 2004]. This assumption guided most previous laboratory studies of pyroxene optical

constants [*Jäger et al.,* 1994; *Dorschner et al.,* 1995; *Henning and Mutschke,* 1997]. Using ISO, crystalline pyroxene was detected in dust produced by evolved stars [*Molster et al.,* 2002], the circumstellar disks of young stellar objects (YSO's) [*Bouwman et al*. 2001] and planetary nebula [*Beintema,* 1997]. As a result of the detection of crystalline pyroxene around planetary nebula, *Jäger et al.* [1998] estimated the MIR optical constants for a natural enstatite (low-Ca orthopyroxene) sample along the crystallographic axes using Kramers-Kronig analysis. Better characterization of the materials in circumstellar environments would improve our understanding of dust formation and processing and enable comparison to our own solar system.

3.4. Methods

3.4.1 *Sample description and preparation*

All samples are large single crystals (roughly 0.5−1 cm on a side) and their chemical compositions are summarized in Table 3.1. Approximate major element abundances were determined by scanning electron microscope energy dispersive x-ray spectroscopy (SEM–EDS). To produce the chemical formulas in Table 3.1, atomic abundances of oxygen were assumed by stoichiometry to be O_6, which may introduce error if any non-pyroxene phases are present in the samples. We prepared thin sections of each sample in order to optically examine the samples for exsolution and twinning. One augite (Aug1) sample was loaned from the Stony Brook Geosciences Department mineral collection and originates from Indian Well, AZ. This sample does not show signs of exsolution or twinning. The diopside (Diop1) sample was purchased from Kelly's Rocks and is from Magog, QC, Canada. While twinning is present over ~30−40% of a section perpendicular to the *a-c* plane in the diopside sample, the IR spectra match previously published oriented reflectance spectra [*Johnson et al*., 2002]. The hedenbergite (Hed1) and second augite (Aug2) sample were provided by D. Lindsley at Stony Brook University. The

hedenbergite sample does not exhibit exsolution or twinning, while Aug2 appears to contain lamellae that remain dark under crossed polar illumination at all orientations. Micro-FTIR spectra of these lamellae are quite noisy compared to the rest of the augite sample, and show a broad reflectance peak at around 3900 cm^{-1} and a peak at 1015cm^{-1}. These spectral features indicate some type of clay, however the exact composition is difficult to discern. The FTIR spectrum of the whole sample does not show a 3900 cm^{-1} peak, indicating this is a relatively minor component. The diopside, hedenbergite, and augite compositions are shown on the ternary diagram in Figure 3.1. We cut each sample with a diamond saw blade so that one surface is parallel to the *a-c* plane (010) and the other perpendicular to it –– planes (001) or (100). We polished these surfaces to 0.25 μm surface roughness, and confirmed the orientations of the cut surfaces by single crystal XRD. XRD analysis involved collection of the preliminary set of frames (pre-experiment) for the determination of unit cell and the orientation matrix. Using this information, we indexed the faces of the crystal with the CrysAlisPRO software. We collected reflections for determination of the orientation matrix using a four-circle kappa Oxford Gemini diffractometer equipped with an Atlas detector (λ = 0.71073 Å).

3.4.2 Collection of mid and far-IR reflectance spectra

We acquired specular reflectance spectra on the Stony Brook University Vibrational Spectroscopy Laboratory's Nicolet 6700 Fourier Transform Infrared (FTIR) spectrometer using a FT–30 specular reflectance accessory with incidence and reflection angles of 30 degrees at a spectral sampling of 2 cm^{-1}. An InfraSpecs wire grid IR polarizer was placed in the beam path for collection of polarized reflectance spectra. For each sample, we measured reflectance spectra for four orientations of the crystal with respect to the incident polarized beam. Depending on whether the *a*– or *c*–axis was more readily identifiable, these orientations were 0°, 45°, 90° and

110° from the identified crystallographic axis. MIR spectra were collected over a range of 400–4000 cm^{-1} using a KBr beamsplitter and DTGS detector with a CsI window. Each spectrum is an average of 256 scans. Far-IR (FIR) spectra were acquired from 250–600 cm^{-1} using a Nicolet Solid Substrate beamsplitter and a DTGS detector with a polyethylene window. Each of these spectra is an average of 512 scans. The two wavelength ranges are joined at 600 cm^{-1} using the overlapping region (600 cm^{-1} – 400 cm^{-1}) to scale the spectral contrast of the FIR spectra. MIR and FIR spectral contrast varies by up to 10% due to slight differences in measurement conditions and/or a few degree error in crystal orientation. Samples were placed on a holder that acts as a mask, controlling the spot size. We chose the largest spot size that can be completely covered by the polished surface of the sample. The bottom of the sample holders is coated with paraffin soot to reduce stray reflectance off of the holder into the sample chamber. For the smaller spot-sizes (<0.5 cm diameter) we subtracted a spectrum of the sample holder without a sample or standard placed on top. While the sample holder does not affect the mid-IR reflectance, there is a steep upward slope starting at around 400 cm^{-1} which rapidly increases from 0.01 to several percent reflectance at ~100 cm^{-1}.

3.4.3 Modeling of optical constants

The optical constants (*n*,*k*) are related to the wavelength-dependent dielectric function ($\varepsilon(\lambda)$) of the material ($\tilde{n} = \varepsilon^{1/2}$). Electron states in non-conducting materials can be modeled as damped harmonic oscillators, which exhibit spring-like behavior [*Griffiths*, 1999]. The E-field of the incoming beam acts as a driving force on the oscillators, which have resonant frequencies ν_j (cm^{-1}). The parameters s_j (cm^{-2}), γ_j (cm^{-1}) and ε_∞ are the oscillator strength, damping coefficient (proportional to the oscillator velocity) and infinite frequency dielectric constant respectively. These parameters are explained in more detail in Section 5.1.

For minerals of orthorhombic and higher symmetry, we can assume that these oscillations occur parallel to the crystallographic axes. In this case, optical constants can be determined using the approach of *Spitzer and Kleinman* [1961]. Reflectance spectra are acquired for each principal axis with the polarization parallel to each axis. Each spectrum is iteratively fit with estimated values of the oscillator parameters as input.

When a mineral is biaxial and the axes are not orthogonal, the oscillators cannot be assumed to be parallel to the crystallographic axes (Belousov and Pavinich 1978). In a monoclinic material, optical constants with E parallel to the *b*-axis (where the oscillators are parallel to the axis) can be determined in the same manner as the orthorhombic case. In the *a*–*c* plane, oscillators are coplanar with, but not parallel to the crystallographic axes. To determine the two remaining principle refractive indices, it is necessary to make measurements at three different angles (Ω) with respect to the crystallographic axes in the *a*-*c* plane [*Aronson et al*., 1983], with measurements at more angles providing more robust fits. This results in an additional oscillator parameters θ_j and φ_j. A useful diagram of such an experimental setup is given in Fig. 1 of *Ivanovski et al.* [2007]. The principle complex indices of refraction are the eigenvalues of the complex dielectric-permittivity tensor, which can be calculated as follows, where N is the number of oscillators:

$$E = (n + ik)^2 = \begin{pmatrix} \varepsilon_{\infty xx} & \varepsilon_{\infty xy} & \varepsilon_{\infty xz} \\ \varepsilon_{\infty yx} & \varepsilon_{\infty yy} & \varepsilon_{\infty yz} \\ \varepsilon_{\infty zx} & \varepsilon_{\infty zy} & \varepsilon_{\infty zz} \end{pmatrix} + \sum_{j=1}^{N} \frac{s_j}{\nu_j^2 - i\gamma_j\nu - \nu^2} \times \begin{pmatrix} \sin^2\theta_j\cos^2\varphi_j & \sin^2\theta_j\sin\varphi_j\cos\varphi_j & \sin\theta_j\cos\theta_j\cos\varphi_j \\ \sin^2\theta_j\sin\varphi_j\cos\varphi_j & \sin^2\theta_j\sin^2\varphi_j & \sin\theta_j\cos\theta_j\sin\varphi_j \\ \sin\theta_j\cos\theta_j\cos\varphi_j & \sin\theta_j\cos\theta_j\sin\varphi_j & \cos^2\theta_j \end{pmatrix} \quad (3.1)$$

The reflectance spectra for all Ω are fit simultaneously. Fixing the *b*-axis as the *z*-axis of the dielectric tensor, ε needs to be rotated with Ω, according to:

$$\varepsilon = \begin{pmatrix} \cos\Omega & \sin\Omega \\ -\sin\Omega & \cos\Omega \end{pmatrix} \begin{pmatrix} \varepsilon_{xx} & \varepsilon_{xy} \\ \varepsilon_{xy} & \varepsilon_{zz} \end{pmatrix} \begin{pmatrix} \cos\Omega & -\sin\Omega \\ \sin\Omega & \cos\Omega \end{pmatrix} \qquad (3.2)$$

Because of the additional complexity in measurement and calculation, optical constants have been derived from single crystal samples for only a few monoclinic materials, including gypsum and orthoclase [*Long et al.*, 1992; *Aronson et al.*, 1983, *Aronson*, 1986). A similar method for triclinic materials is outlined by *Aronson et al.* [1985]. However, substitution of the relevant variables in their equations for the reflection coefficients results in a singularity for the monoclinic case [*Mayerhofer et al.*, 2010] instead of reducing to the formulas given in *Aronson et al.* [1983]. In addition, Aronson et al.'s formulation applies only to the case of normal incidence. The Berreman 4x4 matrix formulation [*Berreman*, 1972] gives a more consistent approach for calculating the reflectance coefficients in low-symmetry cases [*Mayerhofer and Popp*, 2007].

Mayerhofer and Popp [2007] define a matrix $\widetilde{M}$ that can be used to calculate the reflection coefficients as a function of incidence angle (α):

$$\widetilde{M} = D_{\psi}^{-1}(0) D_{\psi}(1) \qquad (3.4)$$

$$r_{xx} = \frac{\widetilde{M}_{21}\widetilde{M}_{33} - \widetilde{M}_{23}\widetilde{M}_{31}}{\widetilde{M}_{11}\widetilde{M}_{33} - \widetilde{M}_{13}\widetilde{M}_{31}} \qquad (3.4a)$$

$$r_{xy} = \frac{\widetilde{M}_{41}\widetilde{M}_{33} - \widetilde{M}_{43}\widetilde{M}_{31}}{\widetilde{M}_{11}\widetilde{M}_{33} - \widetilde{M}_{13}\widetilde{M}_{31}} \qquad (3.4b)$$

$D\Psi(0)$ and $D\Psi(1)$ are the dynamical matrices of the incident and refracted waves [*Yeh*, 1979]:

$$D_{\Psi}^{-1}(0) = \frac{1}{2} \begin{pmatrix} 1 & 1/n\cos\alpha & 0 & 0 \\ 1 & -1/n\cos\alpha & 0 & 0 \\ 0 & 0 & 1/\cos\alpha & 1/n \\ 0 & 0 & -1/\cos\alpha & 1/n \end{pmatrix} \qquad (3.5)$$

$$D_\Psi(1) = \begin{pmatrix} \varepsilon_{xy}\left(1-\frac{k_y^2}{\varepsilon_{zz}}\right) & 0 & \varepsilon_{xy}\left(1-\frac{k_y^2}{\varepsilon_{zz}}\right) & 0 \\ \mathring{a}_{xy}\left(1-\frac{k_y^2}{\varepsilon_{zz}}\right)\gamma_1 & 0 & \varepsilon_{xy}\left(1-\frac{k_y^2}{\varepsilon_{zz}}\right)\gamma_3 & 0 \\ \left(1-\frac{k_y^2}{\varepsilon_{zz}}\right)[\gamma_1^2-(\varepsilon_{xx}-k_y^2)] & 0 & \left(1-\frac{k_y^2}{\varepsilon_{zz}}\right)[\gamma_3^2-(\varepsilon_{xx}-k_y^2)] & 0 \\ [\gamma_1^2-(\varepsilon_{xx}-k_y^2)]\gamma_1 & 0 & [\gamma_3^2-(\varepsilon_{xx}-k_y^2)]\gamma_3 & 0 \end{pmatrix} \quad (3.6)$$

where n is the index of refraction of the incident medium, k_y is the y-component of the wave-vector (the magnitude and direction of the incoming beam), and

$$\gamma_1 = \sqrt{-\frac{1}{2\varepsilon_{zz}}\left(K_1+\sqrt{K_1^2+K_2}\right)} \quad (3.7a)$$

$$\gamma_3 = \sqrt{\frac{1}{\varepsilon_{zz}}\left(-K_1+\sqrt{K_1^2+K_2}\right)} \quad (3.7b)$$

$$K_1 = -\varepsilon_{zz}(\varepsilon_{xx}+\varepsilon_{yy})+k_y^2(\varepsilon_{yy}+\varepsilon_{zz}) \quad (3.8a)$$

$$K_2 = -4\left[\varepsilon_{xy}^2+\varepsilon_{yy}\left(k_y^2-\varepsilon_{xx}\right)\right](k_y^2-\varepsilon_{zz})\varepsilon_{zz}. \quad (3.8b)$$

To perform the required calculations, we use the Matlab non-linear fitting routine lsqcurvefit, which allows us to set lower and upper bounds, ensuring that the final values for the oscillator parameters are positive. To produce the initial parameters for this model, we first fit the spectrum for each Ω as if it is orthorhombic and at normal incidence. The parameters ν_j and γ_j can be estimated reasonably by visual inspection, while s_j is estimated as in *Pavinich and Belousov* [1978]. Reflectance spectra for all orientations are then fit simultaneously, using the Ω where s_j is the largest for a given ν_j as an initial guess for φ_j.

We attempt to fit the reflectance spectrum with the minimum number of oscillators necessary. Starting with the number of main peaks, modes are added until a reasonable fit is obtained for any overlapping peaks or shoulders (a difference between the measured and modeled reflectance of less than 10%). Sometimes modes can be at the same frequency or very

close in frequency, with different θ_j. In this case, although there is only one peak, the fit will be poor without an additional oscillator.

3.4.4 Oscillator parameter error estimates

The model fit is commonly assessed using the standard error of the oscillator parameters. We report the standard error ($\sigma(\nu)$, $\sigma(\gamma)$ etc.) for each parameter in Tables 3.2-3.6. This does not reflect the impact of the initial guesses of the oscillator parameters on the final reflectance fit. Poor initial estimates of starting values may result in slow convergence, non-convergence or convergence on a local rather than global minimum in our model. For each sample, we used five different sets of starting values centered around those produced by the fit to the orthorhombic model to qualitatively evaluate how much the final *n* and *k* values depended on the initial estimates. Those that gave the best reflectance fit were used to calculate the optical constants. As an additional test, we independently varied the sets of ν_j , γ_j, s_j, and φ_j parameters for a gem-quality orthoclase sample to determine which had the largest impact on the final *n* and *k* values. Large (± 30 cm^{-1} for ν_j and ± 50% for all others) variations in the other parameters do not appear to have a major effect on the fit (see Figures 3.2–3.5). Figure 3.6 shows the final fits when all parameters are varied by these amounts (top) as well the 95% confidence bounds based of the standard error of the parameters (bottom). The two measures of uncertainty appear to diverge from the calculated optical constants at different wavenumbers.

3.5. Results

For each sample we present the measured and modeled reflectance and the plots of *n* and *k* as a function of wavelength derived from the reflectance fit. The measured and modeled spectra, as well as the derived optical constants and oscillator parameters are available at http://aram.ess.sunysb.edu/tglotch/optical_constants.html.

3.5.1 Augite 1

Measured reflectance and model are shown in Figure 3.7, with incident E-field polarization parallel to the *a-c* plane (top three) and parallel to b (bottom). Derived values of *n* and *k* are shown in Figure 3.8. In Figure 3.8 n1, n2 and k1, k2 are the optical constants for the rays whose polarization direction is parallel to the *a-c* plane, while nb and kb are the optical constants for the rays with polarization direction along the b crystallographic axis. Oscillator parameters for this sample are given in Table 3.2.

3.5.2 Augite 2

Measured reflectance and model are shown in Figure 3.9, with incident E-field polarization parallel to the *a-c* plane (top three) and parallel to b (bottom). Derived values of *n* and *k* are given in Figure 3.10. In Figure 3.10 n1, n2 and k1, k2 are the optical constants for the rays whose polarization direction is parallel to the *a-c* plane, while nb and kb are the optical constants for the rays with polarization direction along the b crystallographic axis. Oscillator parameters for this sample are given in Table 3.3.

3.5.3 Diopside

Measured reflectance and model are shown in Figure 3.11, with incident E-field polarization parallel to the *a-c* plane (top three) and parallel to b (bottom). Derived values of *n* and *k* are shown in Figure 3.12. In Figure 12 n1, n2 and k1, k2 are the optical constants for the rays whose polarization direction is parallel to the *a-c* plane, while nb and kb are the optical constants for the rays with polarization direction along the b crystallographic axis. Oscillator parameters for this sample are given in Table 3.4.

3.5.4 Hedenbergite

Measured reflectance and model are shown in Figure 3.13, with incident E-field polarization parallel to the *a-c* plane (top three) and parallel to b (bottom). Derived values of *n* and *k* are shown in Figure 3.14. In Figure 14 n1, n2 and k1, k2 are the optical constants for the rays whose polarization direction is parallel to the *a-c* plane, while nb and kb are the optical constants for the rays with polarization direction along the b crystallographic axis.Oscillator parameters for this sample are given in Table 3.5.

3.5.5 Orthoclase

Measured reflectance and model are shown in Figure 3.15, with incident E-field polarization parallel to the *a-c* plane (top three) and parallel to b (bottom). Derived values of *n* and *k* are shown in Figure 3.16 as well as those from Aronson et al. (1986). In Figure 3.16 n1, n2 and k1, k2 are the optical constants for the rays whose polarization direction is parallel to the a-c plane, while nb and kb are the optical constants for the rays with polarization direction along the b crystallographic axis. Oscillator parameters for this sample are given in Table 3.6.

3.6. Discussion

3.6.1 Interpretation of dispersion parameters

The optical constants n and k are related to the polarizability (α), the dependence of the magnitude of the dipole moment on an applied electric field, and conductivity (σ), the ability of a material to carry a current, which are both properties of the material. The dependence of the polarizability and conductivity and hence the optical constants on wavelength are given by dispersion relations. To derive these dispersion relations, Lorentz postulated that insulating materials contain electrons that are bound to atoms or molecules by Hooke's law forces (Seitz 1940), so that the binding force is proportional to the charge displacement. The motion of the bound electron is described as a harmonic oscillator subject to a periodic electric field ($\mathbf{E}=\mathbf{E_0}e^{-2\pi\iota\nu t)}$) and damped by a force proportional to the electron's velocity ($m_e\gamma\frac{dx}{dt}$) giving:

$$\frac{d^2x}{d^2t}+2\pi\gamma\frac{dx}{dt}+4\pi^2\nu_0^2x=\frac{-q_e}{m_e}E_0e^{2\pi i\upsilon t} \qquad (3.9)$$

$$x=\frac{q_e}{4\pi^2m_e}\frac{E_0e^{-2\pi i\upsilon t}}{\nu_0^2-\nu^2-i\gamma\nu} \qquad (3.10)$$

The resonant frequency of the oscillator is ν_0 and the damping constant is $2\pi m_e\gamma$. As ν passes through the value ν_0, there is a peak in the absorption coefficient with a half-width of roughly γ. The order of magnitude of γ can be estimated by the following [*Seitz,* 1940]:

$$\gamma\sim\frac{4\pi\nu^2q_e^2}{3m_ec} \qquad (3.11)$$

Where q_e is in statcoulombs, ν is in wavenumbers, m_e is in grams and c is in cm/s. Looking at Eq (3.10) and assuming the dipole moment has a linear response to the electric field (**p**=$\varepsilon_0\alpha$**E**), results in:

$$\alpha = \frac{q_e^2}{4\pi^2 m_e \varepsilon_0} \frac{1}{\nu_0^2 - \nu^2 - i\gamma\nu} \qquad (3.12)$$

Using a form of the Clausius-Mosotti relation $\varepsilon = \varepsilon_\infty + 4\pi\chi = \varepsilon_\infty + 4\pi N\alpha$ [*Spitzer et al.,* 1959] gives the dispersion relation for a single resonance.

Of course, for a given material, there will not be just one resonant frequency, but several ν_j each with a different damping constant γ_j. The quantum mechanical approach to this problem deals with this and also gives one additional parameter oscillator "strength" (f_j), a weighting for each oscillator that relates to the absorption or transition probability [*Seitz,* 1940; *Spitzer and Kleinman,* 1961; *Born and Wolf,* 1970). The parameter s_j used in Eq (3.1) can be defined in terms of f_j as shown in *Spitzer and Kleinman* [1961].

$$s_j = 4\pi\rho_j\nu_j^2 = \frac{Nq_e^2}{\pi m_e} f_j \qquad (3.13)$$

While educated guesses can be made, the oscillator parameters (ν_j, γ_j, and s_j) are difficult to derive exactly from first principles, which is why an iterative technique is normally used. The infinite frequency dielectric constant ε_∞ can be estimated from the square of the visible-wavelength index of refraction [*Roush et al*., 1991].

3.6.2 Comparison with previously derived Orthoclase optical constants

Optical constants for orthoclase have been derived from oriented single crystal reflectance spectra by previous workers [*Aronson et al*., 1986]. Figure 3.16 shows the values found in this study along with those from *Aronson et al.* [1986]. The optical constants for the E-field polarization parallel to b orientation (nb and kb) are very similar, while the optical constants (n1,n2 and k1,k2) for the E-field parallel to the *a-c* plane have slight differences. Variations between the two data sets may be due to either compositional differences in the samples or uncertainties in orientation. Our orthoclase sample had a small amount of Fe^{3+} substituting for Al^{3+} (see Table 3.1). However, without any compositional information on the sample used in the *Aronson et al.* [1986] study, it is difficult to make inferences about specific bands.

3.6.3 *Dependence of optical constants on crystal structure and chemistry*

Isometric minerals will have one set of optical constants for each wavelength. Because most minerals are anisotropic, the polarizability and conductivity will be directionally as well as wavelength dependent and therefore so will the optical constants. Dispersion in uniaxial and biaxial minerals is described by a dielectric tensor rather than just a dielectric constant. The number of oscillator parameters necessary to fit the reflectance spectrum generally increases with decreasing crystal symmetry. Figure 3.17 shows averaged optical constants in the MIR for several minerals that belong to different crystal systems. It is also important to measure optical constants for several different chemical compositions within the same mineral group. As shown in this work, optical constants vary considerably with chemistry. Simply using one composition of olivine, for example, may produce poor fits for mineralogical abundance as shown in *Liu* [2012] at VNIR wavelengths.

For silicates, there is a steep absorption edge in the UV-range after which *k*-values drop by orders of magnitude and remain low through the VNIR. As a result, after the UV-edge, dispersion is low until the MIR, where the fundamental vibrational bands occur. There is a steep rise in *k* between 8 and 10 μm (1250cm^{-1}–1000cm^{-1}), with the maximum *k* occurring where *n*=1 or slightly lower than 1. This is known as the Christiansen feature and is associated with a minimum in reflectance and a maximum in emission. This feature is the means by which Diviner data are used to identify lunar silicates [*Greenhagen et al*., 2010]. Following the Christiansen feature, there is a steep drop-off in *k* and rise in *n*, causing a drop-off in emission followed by Reststrahlen features. For pyroxenes, spectral features in the ~8–22 μm (~1250cm^{-1}–450cm^{-1}) range are mainly due to Si–O stretching, Si–O–Si bending and modes of the cation-O_6 octahedra. The positions of absorptions at these wavelengths vary with Mg # (defined as Mg/(Mg+Fe)) [*Jäger et al.,* 1998; *Hamilton,* 2000; *Bowey et al.,* 2007; *Lane et al.,* 2011], likely due to the effect of the substitution on the octahedral layer, which in turn alters the Si-O vibrations [*Hamilton,* 2000; *Klima,* 2007]. To demonstrate these effects, Figure 3.18 shows the reflectance and optical constants for olivine (from *Zeidler et al.* [2011]) ranging from the UV

through the MIR, with the major spectroscopic features labeled. This figure also demonstrates that *n* and *k* values of silicates vary considerably in the mid-IR as compared with other wavelengths.

Amorphous pyroxenes produced by vapor phase condensation and synthetic glasses of pyroxene composition will lack many of the spectroscopic features of a crystalline pyroxene. As a result, the optical constants of these materials will have broader and fewer peaks than crystalline pyroxene. To date, little work has been done on oriented crystalline samples [*Jäger et al.,* 1998], and none has been done to date on clinopyroxene. Figure 3.19 demonstrates the difference between optical constants of crystalline versus amorphous phases. Additionally, oriented single crystal spectra are preferable to orientation-averaged data acquired from pellets pressed from powders, as the lower maxima of the specular reflectance peaks of pellets results in lower maxima of derived optical constants when compared to orientation-averaged single crystal optical constants [*Roush,* 1991].

3.7. Implications

Radiative transfer models of planetary surfaces require optical constants for each component that may be present. Applying these models is difficult in the MIR due to the absence of optical constants for many important minerals in the monoclinic and triclinic crystal systems. We have applied the Berreman 4x4 matrix method to derive the MIR optical constants of 5 different pyroxenes for which oriented single-crystal data were not previously reported in the literature. Four spectra with a polarized incident beam at different orientations were acquired for each sample, resulting in three sets of optical constants that can be used to estimate n and k for a randomly oriented powdered sample. These data are necessary to improve compositional estimates of planetary regolith based on radiative transfer models.

The data presented here, in conjunction with a coupled optical-thermal model, such as that of *Milan et al.* [2011], can be used to model MIR emissivity spectra in a vacuum environment relevant to airless solar system bodies. Modeled emission spectra can be compared to emissivity

of the lunar surface derived from Diviner Lunar Radiometer data. These optical constants are also applicable to any MIR data from Mars or any airless solar system objects including: existing spectra of asteroids from ISO, Spitzer and any future data from James Webb Space Telescope (JWST) or the OSIRIS-REx mission. Future work will include expanding the current version of the code to include the triclinic case. This code for triclinic minerals will be applied to obtain feldspar optical constants. The Matlab scripts developed for this work will be made publicly available to other researchers at http://aram.ess.sunysb.edu/tglotch/

Acknowledgements

We thank D. Lindsley for providing two of the samples used in this work. This work was supported by NSF award # AST-1150652 made to T. D. G. XRD analysis including face-indexation was supported by the U.S. Department of Energy, Office of Science, Office of Basic Energy Science, under contract DE-FG02-09ER46650. Diffraction data were collected on Stony Brook University Single-Crystal Diffractometer, obtained through the support of NSF (CHE-0840483).

References

Allen, C.C., Greenhagen, B.T., Donaldson Hanna, K.L. and Paige, D.A. (2011), Analysis of lunar pyroclastic deposit FeO abundances by LRO Diviner, *Journal of Geophysical Research: Planets, 117*(E12).

Arnold, J.A., Glotch, T.D., Greenhagen, B.T., Thomas, I.R., and Bowles, N.E. (2013), Enhanced compositional analysis of the Moon using Diviner's long wavelength channels, *European Planetary Science Conference*, abstract 686.

Aronson, J.R., Emslie, A.G., Miseo, E.V., Smith, E.M., Strong, P.F. (1983), Optical constants of monoclinic anisotropic crystals: gypsum, *Applied Optics, 22*(24), 4093–4098.

Aronson, J.R., Emslie, A.G., Strong, P.F. (1985), Optical constants of triclinic anisotropic crystals: blue vitriol, *Applied Optics, 24*(8), 1200–1203.

Aronson, J.R. (1986), Optical constants of monoclinic anisotropic crystals: Orthoclase, *Spectrochimica Acta Part A: Molecular Spectroscopy, 42*(2–3), 187–190.

Bandfield, J.L., Hamilton, V.E., and Christensen, P.R. (2000), A Global View of Martian Surface Compositions from MGS-TES, *Science, 287*(5458), 1626–1630.

Beintema, D.A. (1997), PAH's and crystalline silicates in planetary nebula, *Astrophysics and Space Science, 225*(1-2), 507–512.

Belousov, M.V. and Pavinich, V.F. (1978), Infrared reflection spectra of monoclinic crystals, *Optics and Spectroscopy, 45*(5), 771–774.

Berreman , D.W. (1972), Optics in Stratified and Anisotropic Media: 4 × 4–Matrix Formulation, *Journal of the Optical Society of America, 62*(4), 502–510.

Bouwman, J., Meeus, G., de Koter, A., Hony, S., Dominik, C., Waters, L.B.F.M. (2001), Processing of silicate dust grains in Herbig Ae/Be systems, *Astronomy and Astrophysics, 375*, 950–962.

Born, M. and Wolf, E. (1999), Principles of Optics, p. 840, Cambridge University Press, UK.

Bowey, J.E., Morlock, A., Kohler, M. and Grady, M. (2007), 2–16 um spectroscopy of micron-sized enstatite $(Mg,Fe)_2Si_2O_6$ silicates from primitive chondritic meteorites, *Monthly Notices of the Royal Astronomical Society, 376*(3), 1367–1374.

Braatz, A., Ott, U., Henning, Th., Jäger, C. and Jeschke, G. (2000), Infrared, ultraviolet, and electron paramagnetic resonance measurements on presolar diamonds: Implications for optical features and origin, *Meteoritics & Planetary Science*, *35*(1), 75–84.

Bradley, J. P., Brownlee, D. E., and Veblen, D. R. (1983), Pyroxene whiskers and platelets in interplanetary dust - Evidence of vapour phase growth, *Nature*, *301*, 473–477.

Chapman, C.R., Morrison, D., and Zellner, B. (1975), Surface properties of asteroids: A synthesis of polarimetry, radiometry, and spectrophotometry, *Icarus, 25*(1), 104–130.

Conel, J.E. (1969), Infrared emissivities of silicates: Experimental results and a cloudy atmosphere model of Spectral emission from condensed particulate mediums, *Journal of Geophysical Research, 74*(6), 1614–1634

De Sanctis, M.C., Ammannito, E. Capria, M.T., Tosi, F., Capaccioni, F., Zambon, F., Carraro, F., Fonte, S., Frigeri, A., Jaumann, R., Magni, G., Marchi, S., McCord, T.B., McFadden, L.A., McSween, H.Y., Mittlefehldt, D.W., Nathues, A., Palomba, E., Pieters, C.M., Raymond, C.A., Russell, C.T., Toplis, M.J., and Turrini, D. (2012), Spectroscopic Characterization of Mineralogy and Its Diversity Across Vesta, *Science, 336*(6082), 697–700.

Donaldson Hanna, K.L., Thomas, I.R., Bowles, N.E., Greenhagen, B.T., Pieters, C.M., Mustard, J.F., Jackson, C.R.M. and Wyatt, M.B. (2012), Laboratory emissivity measurements of the plagioclase solid solution series under varying environmental conditions, *Journal of Geophysical Research, 117*(E11004), 7pp.

Dorschner, J., Begemann, B., Henning, T., Jaeger, C., and Mutschke, H. (1995), Steps toward interstellar silicate mineralogy. II. Study of Mg–Fe-silicate glasses of variable composition, *Astronomy and Astrophysics*, *300*, 503–520.

Dyar, M. D., Sklute, E. C., Menzies, O. N., Bland, P. A., Lindsley, D., Glotch, T., Lane, M. D., Schaefer, M. W., Wopenka, B., Klima, R., Bishop, J. L., Hiroi, T., Pieters, C., and Sunshine, J. (2009), Spectroscopic characteristics of synthetic olivine: An integrated multi-wavelength and multi-technique approach, *American Mineralogist, 94*(7), 883–898.

Fabian, D., Henning, T., Jäger, C., Mutschke, H., Dorschner, J., Wehrhan, O. (2001), Steps toward interstellar silicate mineralogy, *Astronomy & Astrophysics, 378*(1), 228–238.

Glotch, T. D. and Rossman, G. R. (2009), Mid-infrared reflectance spectra and optical constants of six iron oxide/oxyhydroxide phases, *Icarus, 204*(2), 663–671.

Glotch, T.D. and Rogers, A.D. (2013), Evidence for magma-carbonate interaction beneath Syrtis Major, Mars, *Journal of Geophysical Research: Planets, 118*, 126–137.

Glotch, T. D., Christensen, P. R., and Sharp, T. G. (2006), Fresnel modeling of hematite crystal surfaces and application to martian hematite spherules, *Icarus, 181*, 408–418.

Glotch, T.D., Rossman, G.R., and Aharonson, O. (2007), Mid-infrared (5-100 μm) reflectance spectra and optical constants of 10 phyllosilicate minerals, *Icarus, 192*, 605–62.

Glotch, T.D., Lucey, P.G., Bandfield, J.L., Greenhagen, B.T., Thomas, I.R., Elphic, R.C., Bowles, N.E., Wyatt, M.B., Allen, C.C., Donaldson Hanna, K.L., and Paige, D.A. (2010), Highly Silicic Compositions on the Moon, *Science, 329*(5998), 1510–1513.

Glotch, T. D., Hagerty, J. J. Lucey, P. G., Hawke, B. R. Giguere, T. A., Arnold, J. A., Williams, J.-P. Jolliff, B. L., and Paige, D. A. (2011), The Mairan Domes: Silicic volcanic constructs on the Moon, *Geophys. Res. Lett., 38*(L21204), doi:10.1029/2011GL049548.

Greenhagen, B.T., Lucey, P.G., Wyatt, M.B., Glotch, T.D., Allen, C.C., Arnold, J.A., Bandfield, J.L., Bowles, N.E., Hanna, K.L.D., Hayne, P.O., Song, E., Thomas, I.R., and Paige,

D.A. (2010), Global Silicate Mineralogy of the Moon from the Diviner Lunar Radiometer, *Science, 329*(5998), 1507–1509.

Griffiths, D.J. (1999), Introduction to Electrodynamics, 3rd ed., 576p, Prentice Hall, Upper Saddle River, New Jersey.

Hamilton, V.E. (2000), Thermal infrared emission spectroscopy of the pyroxene mineral series, *Journal of Geophysical Reasearch, 105*(E4), 9701–9716.

Hamilton, V.E., Christensen, P.R., McSween, H.Y., and Bandfield, J.L. (2001), Searching for the source regions of martian meteorites using MGS TES: Integrating martian meteorites into the global distribution of igneous materials on Mars, *Meteoritics & Planetary Science, 38*(6), 871–885.

Hanner, M.S., Lynch, D.K., and Russel, R.W. (1994), The 8–13 micron spectra of comets and the composition of silicate grains, *Astrophysical Journal, Part I, 425*(1), 274–285.

Hapke, B. (1993a), Theory of Reflectance and Emittance Spectroscopy, 472 p, Cambridge University Press, Cambridge, U.K.

Hapke, B. (2012), Theory of Reflectance and Emittance Spectroscopy, 528 p, Cambridge University Pres, Cambridge, U.K. 2nd edition.

Henning, T. and Mutschke, H. (1997), Low-temperature infrared properties of cosmic dust analogues, *Astronomy and Astrophysics, 327*, 743–754.

Jäger, C., Molster, F.J., Dorschner, J., Henning, Th., Mutschke, H., and Waters, L.B.F.M. (1994), Steps toward interstellar silicate mineralogy. IV. The crystalline revolution, *Astronomy and Astrophysics, 339*, 904–916.

Jäger, C., Mutschke, H., Begemann, B., Dorschner, J., and Henning, T. (1998), Steps toward interstellar silicate mineralogy. 1: Laboratory results of a silicate glass of mean cosmic composition, *Astronomy and Astrophysics, 292*(2), 641–655.

Jäger, C., Dorschner, J., Mutschke, H., Posch, T., and Henning, T. (2003), Steps toward interstellar silicate mineralogy. VII. Spectral properties and crystallization behaviour [sic] of magnesium silicates produced by the sol-gel method, *Astronomy and Astrophysics, 408,* 193-204.

Johnson, E.A., Rossman, G.R., Dyar, M.D., and Valley J.W. (2002), Correlation between OH concentration and oxygen isotope diffusion rate in diopsides from the Adirondack Mountains, New York, *American Mineralogist, 87*(7), 899–908.

Karner, J., Papike, J.J. and Shearer, C.K. (2006), Comparative planetary mineralogy: Pyroxene major- and minor-element chemistry and partitioning of vanadium between pyroxene and melt in planetary basalts, *American Mineralogist, 91*(10), 1574–1582.

Klima, R. L., Pieters, C. M., and Dyar, M. D. (2007), Spectroscopy of synthetic Mg-Fe pyroxenes I: spin-allowed and spin-forbidden crystal field bands in the visible and near-infrared, *Meteoritics & Planetary Science, 42*(2), 235-253.

Kilma, R.L., Pieters, C.M., and Dyar, M.D. (2008), Characterization of the 1.2 μm M1 pyroxene band: Extracting cooling history from near-IR spectra of pyroxenes and pyroxene-dominated rocks, *Meteoritics & Planetary Science, 43*(10), 1591–1604.

Klima, R.L., Pieters, C.M., Boardman, J.W., Green, R.O., Head, J.W. III, Isaacson, P.J., Mustard, J.F., Nettles, J.W., Petro, N.E., Staid, M.I., Sunshine, J.M., Taylor, L.A., Tompkins, S. (2011), New insights into lunar petrology: Distribution and composition of prominent low-Ca

pyroxene exposures as observed by the Moon Mineralogy Mapper (M^3), *Journal of Geophysical Research, 116*(E00G06), 13 pp.

Lane, M.D. (1999), Midinfrared optical constants of calcite and their relationship to particle size effects in thermal emission spectra of granular calcite, *Journal of Geophysical Research—Planets, 104*, 14099–14108.

Liu, D. (2012), An improved radiative transfer model for estimating mineral abundance of immature and mature lunar soils, *LPSC XLIII*.

Logan, L.M., Hunt, G.R., Salisbury, J.W., and Balsamo, S.R. (1973), Compositional implications of Christiansen frequency maximums for infrared remote sensing applications, *Journal of Geophysical Research, 78*(23), 4983-5003.

Long, L. L., Querry, M. R., Bell, R. J., and Alexander, R. W. (1992), Optical propertied of calcite and gypsum in crystalline and powedered form in the infrared and far-infrared, *Infrared Physics, 34*(2), 191-201.

Lucy, P.G. (1998), Model near-infrared optical constants of olivine and pyroxene as a function of iron content, *Journal of Geophysical Research: Planets, 103*(E1), 1703–1713.

Lumme, K. and Bowell, E. (1981), Radiative transfer in the surfaces of atmosphereless bodies. I. Theory, *The Astronomical Journal, 86*(11), 1694–1721.

Mackinnon, I.D.R. and Rietmeijer, F.J.M. (1987), Mineralogy of chondritic interplanetary dust particles, *Review of Geophysics, 25*(7), 1527–1553.

Mayerhofer and Popp (2007), Employing spectra of polycrystalline materials for the verification of optical constants obtained from corresponding low-symmetry single crystals, *Applied Optics, 46*(3), 327–334.

Mayerhofer, T.G., Weber, S., and Popp, J. (2010), Simplified formulas for non-normal reflection from monoclinic crystals, *Optics Communications, 284*(3), 719–723.

McCord, T.B., Adams, J.B., Johnson, T.V. (1970), Asteroid vesta: spectral reflectivity and compositional implications, *Science, 168*(3938), 1445–1447.

Milan, L., Thomas, I., Bowles, N. (2011), Lunar regolith thermal gradients and emission spectra: Modeling and validation, *Journal of Geophysical Research, 116*(E12).

Mishchenko, M.I., Dlugach, J.M., Yanovitskij, E.G. and Zakharova, N.T. (1999), Bidirectional reflectance of flat, opticallt thick particulate layers; an efficient radiative transfer solution and applications to snow and soil surfaces, *Joural of quantitative spectroscopy and radiative transfer, 63*(2-6), 409–432.

Molster, F. and Kemper, C. (2004), Crystalline Silicates, *Space Science Reviews, 119*(1–4), 3–28.

Molster, F.J., Waters, L.B.F.M., Tielens, A.G.G.M., Barlow, M.J. (2002), Crystalline silicate dust around evolved stars, *Astronomy and Astrophysics, 382*, 184–221.

Mustard, J.F., Poulet, F., Gendrin, A., Bibring, J.P., Langevin, Y., Gondet, B., Mangold, N., Bellucci, G., and Altieri, F. (2005), Olivine and Pyroxene Diversity in the Crust of Mars, *Science, 30(*5715), 1594–1597.

Mutschke, H., Andersen, A.C., Jäger, C., Henning, T., and Braatz, A. (2004), Optical data of meteoritic nano-diamonds from far-ultraviolet to far-infrared wavelengths, *Astronomy and Astrophysics, 423*, 983–993.

Ody, A., Poulet, F., Langevin, Y., Bibring, J.P., Bellucci, G., Altieri, F., Gondet, B., Vincendon, M., Carter, J., and Manaud, N. (2012), Global maps of anhydrous minerals at the surface of Mars from OMEGA/MEx, *Journal of Geophysical Research: Planets, 117*(E11).

Paige, D.A., Foote, M.C., Greenhagen, B.T., Schofield, J.T., Calcutt, S., Vasavada, A.R., Preston, D.J., Taylor, F.W., Allen, C.C., Snook, K.J., Jakosky, B.M., Murray, B.C., Soderblom, L.A., Jau, B., Loring, S., Bulharowski, J., Bowles, N.E., Thomas, I.R., Sullivan, M.T., Avis, C., Jong, E.M., Hartford, W., and McCleese, D.J. (2010), The Lunar Reconnaissance Orbiter Diviner Lunar Radiometer Experiment, *Space Science Reviews, 150*(1-4), 125–160.

Pavinich, V.F. and Belousov, M.V. (1978), Dispersion analysis of reflection spectra of monoclinic crystals, Optics and Spectroscopy 45, 881. Translated from Opt. Spektrosk. 45, 1114.

Ramsey, M.S. and Christensen, P.R. (1998), Mineral abundance determination: Quantitative deconvolution of thermal emission spectra, *Journal of Geophysical Research, 103*(B1), 577–596.

Rogers, A.D. and Christensen, P.R. (2007), Surface mineralogy of Martian low–albedo regions from MGS–TES data: Implications for upper crustal evolution and surface alteration, *Journal of Geophysical Research, 112*(E01003).

Rogers, A.D., Bandfield, J.L., and Christensen, P.R (2007), Global spectral classification of Martian low-albedo regions with Mars Global Surveyor Thermal Emission Spectrometer (MGS-TES) data, *Journal of Geophysical Research, 112*(E02004).

Roush, T., Pollack, J., Orenberg, J. (1991), Derivation of midinfrared (5–25 μm) optical constants of some silicates and palagonite, *Icarus, 94*(1), 191–208.

Salisbury, J.W. (1972), Spectroscopic remote sensing of lunar surface composition, *Earth, Moon and Planets, 5*(3-3), 332–347.

Seitz, F. (1940), Modern theory of solids, McGraw-Hill, New York.

Shkuratov, Y., Starukhina, L., Hoffman, H. and Arnold, G. (1999), A model of spectral albedo of particulate surfaces: implications for optical properties of the moon, *Icarus, 137*(2), 235–246.

Shkuratov, Y.G., Kaydash, V.G. and Pieters, C.M. (2004), Lunar Clinopyroxene and Plagioclase: Surface Distribution and Composition, *Solar System Research, 39*(4), 255–266. Translated from *Astronomicheskii Vestnik, 39*, 4, 2005, 291–303 (in Russian).

Song, E., Bandfield, J.L., Lucey, P.G., Greenhagen, B.T., Paige, D.A. (2013), Bulk mineralogy of lunar crater central peaks via thermal infrared spectra from the Diviner Lunar Radiometer: A study of the Moon's crustal composition at depth, *Journal of Geophysical Research: Planets, 118*(4), 689–707.

Sogawa, H., Koike, C., Chihara, H., Suto, H., Tachibaba, S., Tsuchiyama, A., and Kozasa, T. (2006), Infrared reflection specra of forsterite crystal, *Astronomy & Astrophysics, 451*, 357–361.

Spitzer, W.G., Kleinman, D.A. and Walsh, D. (1959), Infrared properties of hexagonal silicon carbide, *Physical Review, 113*(1), 127–132.

Spitzer, W.G. and Kleinman, D.A. (1961), Infrared lattice bands of quartz, *Physical Review, 121*(5,) 1324–1335.

Sunshine, J.M., Bus, J., McCoy, T.J., Burbine, T.H., Corrigan, C.M., and Binzel, R.P. (2004), High–calcium pyroxene as an indicator of igneous differentiation in asteroids and meteorites, *Meteoritics & Planetary Science, 39*(8), 1343–1357.

Suto, H., Koike, C., Sogawa, H., Tsuchiyama, A., Chihara, H., and Mizutani, K. (2002), Infrared spectra of fayalite crystal, *Astronomy & Astrophysics, 389*, 568–571.

Tompkins, S., and Pieters, C.M. (1999), Mineralogy of the lunar crust: Results from Clementine, *Meteroritics and Planetary Science*, *34*, 25–41.

Wenrich, M. L., and Christensen, P. R. (1996), Optical constants of minerals derived from emission spectroscopy: Application to quartz, *Journal of Geophysical Research: Solid Earth, 101*, 15921–15931.

Yeh, P. (1979), Optics of anisotropic layered media: A new 4 × 4 matrix algebra, *Surface Science, 96(*1-3), 41–53.

Zeidler, S., Posch, T., Mutschke, H., Richter, H., and Wehrhan, O. (2011), Near-infrared absorption properties of oxygen-rich stardust analogs. The influence of coloring metal ions, *Astronomy & Astrophysics, 526*(68).

Zeidler, S., Posch, T., and Mutschke, H. (2013), Optical constants of refractory oxides at high temperatures. Mid-infrared properties of corundum, spinel, and alpha-quartz, potential carriers of the 13 mum feature, *Astronomy & Astrophysics*, *553*(81).

Tables and Figures

Table 3.1. Information for pyroxenes and orthoclase included in this study.

Sample	Source (location)	Chemical formula
augite(Aug1)	SBU (Indian Well, AZ)	$Na_{0.11}K_{0.10}Mg_{0.54}Fe_{0.46}Ti_{0.13}Ca_{0.46}Al_{0.48}Si_{1.79}O_6$
diopside(Diop1)	Kelly's Rocks (Magog, QC)	$Na_{0.04}Mg_{0.64}Fe_{0.18}Mn_{0.01}Ca_{0.92}Al_{0.03}Si_{2.09}O_6$
clinopyx(Aug2)	SBU	$Na_{0.02}Mg_{0.57}Fe_{0.40}Ti_{0.02}Ca_{0.69}Al_{0.13}Si_{2.06}O_6$
hedenbergite(Hed1)	SBU	$Na_{0.03}Mg_{0.29}Fe_{0.51}Mn_{0.07}Ca_{0.83}Al_{0.08}Si_{2.08}O_6$
orthoclase	GGGems (Itrongay, Madagascar)	$K_{0.96}Na_{0.04}Al_{0.96}Fe_{0.04}Si_3O_8$

Table 3.2. Oscillator parameters for Augite (Aug1). The parameters ν, γ, s, ϕ and θ are those described in section 5.1. The standard error, σ, is given for each parameter.

j	ν_i	$\sigma(\nu_i)$	γ_i	$\sigma(\gamma_i)$	s_i	$\sigma(s_i)$	φ_i	$\sigma(\varphi_i)$	θ_i
1	1106.3575	0.4039	13.6440	1.4160	4710.7187	519.6075	33.7390	2.2315	90
2	1082.0787	0.7336	22.4311	2.8987	8993.4843	1526.8844	57.9436	2.2866	90
3	1049.0371	0.1930	34.2430	0.6058	179324.6400	2855.2145	71.6003	0.2040	90
4	1010.1750	0.5134	20.6827	1.4914	15743.7790	1164.9098	33.9720	1.4204	90
5	973.9422	1.2439	39.3002	2.5816	61647.1074	7198.6643	100.6033	1.9936	90
6	952.8605	0.6238	33.8723	1.1586	115080.9250	3657.2602	76.5908	1.6294	90
7	911.9700	1.9049	60.9354	5.4555	84647.1159	6815.1152	69.0827	1.9607	90
8	944.8770	0.6580	48.8271	2.4135	96156.4057	6739.0871	130.0419	2.5202	90
9	864.4122	0.4977	43.8169	1.0250	236251.8770	364.8184	1.5422	0.5618	90
10	855.2310	0.9153	31.8268	2.0963	73587.6460	1012.5941	148.5916	2.1071	90
11	768.1230	1.8893	89.4754	7.2442	55510.9508	4229.1492	106.3017	2.6079	90
12	628.8353	0.2212	18.0435	0.7495	33689.7859	1649.9417	101.0689	0.8103	90
13	558.8928	0.5426	20.5635	1.7036	3907.3075	383.2433	-1.2976	4.3107	90
14	527.2604	0.5724	24.0277	2.0407	10163.0101	1027.2230	2.9381	3.4734	90
15	511.0346	0.6194	42.7838	2.2268	48307.6346	3153.4361	113.9736	1.4942	90
16	588.4716	5.8446	86.0548	18.4170	24961.4935	5574.7554	89.6034	3.3377	90
17	487.9342	0.3804	27.1740	1.2809	59799.8695	3570.4805	-7.2227	0.8682	90
18	452.2373	0.2418	29.8619	0.7627	256324.4190	4869.1466	-7.2227	0.1871	90
19	378.5617	0.2780	36.6437	1.4695	53084.6470	8107.2438	84.8518	6.4041	90
20	380.5842	1.0044	53.7977	4.0509	72332.4613	6006.1467	25.3526	6.0986	90
21	316.6041	0.1706	22.8939	0.3635	121807.2190	1236.6558	76.0592	0.3385	90
22	285.8952	0.3018	26.1164	0.7252	78823.7304	1650.5374	141.5585	0.5527	90
23	1066.2639	0.1892	30.6764	0.2559	222090.2320	1434.7913	0	--	0

24	963.3500	0.2452	24.6545	0.6687	89492.5772	2397.4128	0	--	0
25	900.8600	0.5216	61.1955	1.6569	210326.1180	4518.3363	0	--	0
26	673.6817	1.2406	34.7883	3.7145	19978.7527	1653.7995	0	--	0
27	547.9000	0.4589	18.9619	1.7624	6433.4126	786.4962	0	--	0
28	503.9100	0.2723	37.6983	0.8500	148239.2660	4230.4820	0	--	0
29	473.3900	0.2018	18.3338	0.6366	104023.2710	2914.9693	0	--	0
30	408.0200	0.4402	21.1392	1.4232	26911.5056	1472.1208	0	--	0
31	367.1695	1.0108	22.6618	4.1379	12240.3510	2468.8277	0	--	0
32	333.8303	0.7396	37.0955	2.4841	44673.8703	2939.0821	0	--	0
ε_{xx}=2.3418(0.0040)			ε_{xy}=0.0263(0.0036)		ε_{yy}=2.3934(0.0030)			ε_{zz}= 2.6441(0.0043)	

Table 3.3. Oscillator parameters for Augite (Aug 2). The parameters ν, γ, s, ϕ and θ are those described in section 5.1. The standard error, σ, is given for each parameter.

j	ν_i	$\sigma(\nu_i)$	γ_i	$\sigma(\gamma_i)$	s_i	$\sigma(s_i)$	φ_i	$\sigma(\varphi_i)$	θ_i
1	1061.3863	1.6775	16.7945	3.5355	24107.2736	9108.7181	109.9541	3.0586	90
2	1045.6266	1.0695	17.4601	4.5891	49146.8143	15451.7954	118.8724	1.4748	90
3	1021.4581	1.8514	25.7043	6.2705	46430.9850	12385.4430	125.3247	2.1043	90
4	992.3639	1.1743	36.2713	3.4181	26819.2312	2845.9399	4.0808	7.8728	90
5	950.6749	1.8544	56.3535	3.6006	350600.2530	198.6376	92.4733	1.0478	90
6	873.6918	3.5412	73.3247	7.0740	198501.9250	4841.0644	103.9087	5.7859	90
7	852.6279	0.9302	56.1304	2.4576	384449.5580	21164.2827	-0.0526	2.7969	90
8	768.7863	3.5090	100.1498	11.8050	351227.4630	80.4223	-35.0603	1.7465	90
9	600.0011	3.0444	103.2869	9.5882	345195.2700	27533.1404	-49.3688	1.6754	90
10	686.4430	3.5464	112.2921	13.4456	157635.0660	22704.7234	15.7006	3.6531	90
11	625.9819	1.2538	25.3481	4.3195	31759.5593	5445.8591	73.3052	5.5194	90
12	520.0000	1.4388	20.2592	3.8818	55527.2990	8895.0274	82.9539	8.5934	90
13	533.0903	2.2436	17.2663	6.5846	26237.0233	1283.3818	179.8287	8.5146	90
14	501.7328	1.5229	22.9771	4.8641	168521.7630	27.0692	8.2681	4.3965	90
15	479.9509	0.7686	16.6904	2.6651	294597.8250	25.7761	4.6831	2.0602	90
16	461.8681	0.8220	14.9005	1.5448	258672.0850	1733.0123	5.0887	1.8157	90
17	403.8875	1.6247	34.3784	4.1294	86703.4089	6799.8357	99.5010	4.3104	90
18	360.1886	6.2701	27.2829	19.1020	17351.0619	11466.8151	-7.5571	14.6287	90
19	332.0028	1.0169	21.7865	3.0345	38951.2369	4767.2072	72.8595	5.0749	90
20	281.8601	1.4334	41.1500	3.7859	226289.1590	41.8564	32.8478	1.1554	90
21	250.0777	4.5801	15.2753	5.7124	41555.6458	23085.6849	74.3621	10.3421	90
22	1077.2920	0.4198	22.8731	0.6367	149503.0950	2402.3553	0	--	0
23	964.0978	1.2006	48.8749	4.5997	138155.7890	15182.2000	0	--	0

24	899.9383	3.5474	106.4168	7.3552	286332.2180	24390.6181	0	--	0
25	684.1713	5.8182	108.5547	25.4532	66276.4418	26720.9365	0	--	0
26	557.1254	1047.5670	15.2229	666.7554	3104.1971	177321.3230	0	--	0
27	541.0487	3.4361	17.7469	31.3527	9273.8041	161727.1810	0	--	0
28	524.2434	1.6431	18.0151	10.7360	19617.9937	16815.8158	0	--	0
29	507.6945	0.5276	18.0932	2.3374	67758.0486	12997.2329	0	--	0
30	480.6085	0.8391	31.0358	2.9332	173741.2560	16787.0322	0	--	0
31	411.3853	5.8307	45.1586	20.6277	61591.7484	47708.6593	0	--	0
32	370.1525	19.3001	44.4246	135.0416	23586.7622	91495.5373	0	--	0
33	325.5302	12.2621	65.4127	22.8392	72943.9747	51540.5930	0	--	0
34	257.0514	0.9801	12.4295	2.7168	16853.4601	3824.3130	0	--	0
ε_{xx}=3.1888(0.0147)		ε_{xy}=0.0050(0.0168)			ε_{yy}=2.8116 (0.0157)			ε_{zz}= 2.6090 (0.0109)	

Table 3.4. Oscillator parameters for Diopside (Diop 1). The parameters ν, γ, s, ϕ and θ are those described in section 5.1. The standard error, σ, is given for each parameter.

j	ν_i	$\sigma(\nu_i)$	γ_i	$\sigma(\gamma_i)$	s_i	$\sigma(s_i)$	φ_i	$\sigma(\varphi_i)$	θ_i
1	1053.3492	0.2690	9.8041	0.5202	161807.4260	8449.4644	95.0619	0.5386	90
2	1038.6875	0.4434	11.9789	1.1319	102002.5840	8297.6460	81.8839	0.7175	90
3	987.1730	1.1344	22.0697	2.3375	43276.2855	8424.1418	-58.3177	1.7571	90
4	961.9418	0.5321	21.8740	1.4044	328246.2610	13426.1056	107.2574	0.4212	90
5	908.9778	1.2771	34.1717	3.7573	112024.9180	10847.7536	88.2555	1.2813	90
6	851.9349	0.7393	52.0897	1.8660	276075.0410	8603.7134	40.6706	1.1639	90
7	799.5717	2.9359	82.3099	8.5987	133499.1160	11910.3499	140.7057	2.6738	90
8	694.3785	2.9357	139.0056	9.4790	184063.9650	11455.4558	35.9865	1.6679	90
9	625.9676	0.6184	20.9614	1.1518	85562.6394	3066.4869	111.9229	0.8129	90
10	526.8297	1.7909	48.7469	3.7816	97271.7196	11572.2554	45.1962	1.4457	90
11	509.9354	0.7947	14.1122	2.1296	16820.8129	2318.7730	-38.9575	4.1582	90
12	488.7702	1.0874	25.2207	3.2101	102617.7860	14753.3418	51.9415	1.9863	90
13	462.0420	0.8680	37.2480	2.3266	302939.5670	16231.8191	21.2456	0.8955	90
14	379.4407	0.6114	32.5722	1.2839	117538.4980	4685.8259	112.1053	0.9140	90
15	326.4878	0.9753	26.4854	2.6635	108243.6900	14930.1059	-66.8801	1.1360	90
16	297.4023	1.4361	27.9642	5.2131	98661.8029	17147.5147	-59.4064	4.2180	90
17	293.0303	0.7230	16.9140	1.9692	26130.5743	3123.2116	20.9335	12.1318	90
18	236.8182	2.6280	14.3421	3.0202	49054.5289	8115.4718	10.1390	6.1075	90
19	1065.2649	61.4940	50.5334	1.8536	136867.0000	139.1562	0	--	0
20	954.2127	50.9689	35.3480	3.5371	65646.0001	54.6979	0	--	0
21	913.3331	114.3238	31.7870	6.9236	42070.0001	24.6549	0	--	0
22	863.7441	367.8407	126.8820	24.7606	195784.2720	54551.0765	0	--	0
23	737.9597	2678.3443	140.9497	56.2231	92809.1745	52723.1287	0	--	0

24	636.0029	552.8693	93.0399	9.7740	89888.9079	17968.0509	0	--	0
25	504.2384	645.0038	31.7429	1.4460	163435.8470	13745.7938	0	--	0
26	472.0973	792.9559	28.4750	1.9606	276342.9090	15861.7259	0	--	0
27	413.8197	324.9801	26.0624	3.2501	70136.7282	7278.4287	0	--	0
28	249.2397	277.7731	9.7763	1.2649	18139.7810	2824.9225	0	--	0
ε_{xx}=2.2120(0.0092)		ε_{xy}=0.0084(0.0109)			ε_{yy}=3.2076(0.0107)			ε_{zz}= 2.3310(0.0111)	

Table 3.5. Oscillator parameters for Hedenbergite (Hed 1). The parameters ν, γ, s, ϕ and θ are those described in section 5.1. The standard error, σ, is given for each parameter.

j	ν_j	$\sigma(\nu_j)$	γ_j	$\sigma(\gamma_j)$	s_j	$\sigma(s_j)$	φ_j	$\sigma(\varphi_j)$	θ_j
1	1085.5086	1.0619	53.6032	2.0797	71057.9148	10.0624	77.0368	1.6560	90
2	1059.2960	0.5518	45.6650	1.1514	159377.0460	3792.4402	-48.5292	0.5769	90
3	993.1131	1.1689	26.9090	3.5555	9922.7969	2381.2746	38.0265	7.7690	90
4	967.4469	0.8350	45.8181	2.5602	95361.6473	4969.2601	84.6362	1.1185	90
5	904.4503	1.5764	39.7557	4.0140	17736.2350	2895.3918	9.7179	4.8795	90
6	854.4819	0.3215	34.8501	0.7845	359324.3050	3685.3273	8.2315	0.2746	90
7	627.1273	0.4077	18.5918	0.9474	22454.7292	809.0312	70.7968	1.0661	90
8	554.0051	0.8223	20.0375	2.2529	11125.4731	935.6338	80.3744	1.5719	90
9	498.4405	0.5100	36.7979	1.1952	47045.1989	1737.4115	31.5953	0.6441	90
10	444.5136	0.2360	25.4438	0.5064	259681.5030	2531.5769	7.0115	0.1641	90
11	365.7561	0.4065	40.0052	1.1436	115793.2740	2579.3708	-17.1310	0.3263	90
12	316.5364	0.2868	17.5481	0.7074	79478.0308	2327.4479	146.8989	0.4168	90
13	295.8607	0.2829	11.2035	0.8214	38037.8982	2341.3446	-10.7030	0.9746	90
14	269.8787	0.2434	11.4372	0.5673	24979.2863	1003.2629	31.7790	0.9470	90
15	1058.5000	0.1466	13.5591	0.1493	298081.4700	1586.6960	0	--	0
16	954.2000	0.1756	15.9576	0.3435	155456.8690	2858.5771	0	--	0
17	905.3000	0.3818	37.5829	1.0258	283403.9260	5357.2963	0	--	0
18	661.1000	1.2062	61.1123	3.4700	68518.4267	3042.9618	0	--	0
19	509.4000	0.2300	25.7632	0.3148	236134.3190	3062.6966	0	--	0
20	471.8000	0.2540	14.0770	0.6940	81073.6183	2729.1871	0	--	0
21	398.1000	0.3743	23.0772	1.0692	64178.4958	2420.5236	0	--	0
22	363.7127	0.6361	14.3740	2.4526	17497.1025	3048.7496	0	--	0
23	330.9739	1.4859	43.8902	5.1669	49615.4221	5331.1122	0	--	0
24	277.0999	0.3965	9.3079	1.2061	11291.1774	1162.9514	0	--	0

ε_{xx}=2.323433(0.005738)	ε_{xy}=0.011083(0.004933)	ε_{yy}=1.811383(0.004054)	ε_{zz}= 3.476333(0.0063)

Table 3.6. Oscillator parameters for Orthoclase (Orth 1). The parameters ν, γ, s, ϕ and θ are those described in section 5.1. The standard error, σ, is given for each parameter.

j	ν_j	$\sigma(\nu_j)$	γ_j	$\sigma(\gamma_j)$	s_j	$\sigma(s_j)$	φ_j	$\sigma(\varphi_j)$	θ_j
1	1128.3686	0.3431	31.2995	0.7423	54556.3167	2123.2030	144.4339	1.2192	90
2	1108.8571	0.5588	31.1108	0.5308	212226.6890	3795.8550	24.3628	0.4137	90
3	1027.3708	0.3793	33.1247	0.6044	363554.0780	18.0570	96.9297	1.5021	90
4	1037.7416	0.5378	30.7390	1.3144	141912.7300	17.9877	4.6421	2.7087	90
5	1009.9518	0.4677	22.2564	1.0482	172752.3130	5177.9700	175.9980	1.8392	90
6	991.7254	0.5793	24.2304	2.0259	150428.1450	11517.6300	103.3195	1.8847	90
7	765.4734	3.4041	42.0367	10.9087	15482.5298	3241.5640	5.9023	6.1221	90
8	718.5118	1.2856	27.2765	3.9460	20263.4125	2306.1400	-51.0158	3.5496	90
9	638.1094	0.4900	17.9200	1.1941	28666.8966	1392.3170	145.0234	1.2033	90
10	578.8337	1.6291	24.5589	1.0170	42223.7579	9406.2510	43.3327	1.7890	90
11	570.6447	0.5394	11.6388	0.7779	73786.7114	488.4382	42.3799	1.2196	90
12	563.4729	0.7157	9.2861	1.9959	35232.0422	9229.9400	39.1535	2.2532	90
13	415.7642	0.5353	34.7887	0.7423	114579.3000	1911.6290	-41.7658	0.4592	90
14	1135.3801	0.8506	39.8303	2.1129	14854.1612	1579.1328	0	--	0
15	1102.8937	0.5060	42.5629	2.0172	32799.5356	2104.3277	0	--	0
16	1020.6898	0.5366	42.7108	0.7767	259002.7780	13008.0113	0	--	0
17	992.4225	0.2744	32.1287	0.8942	387229.1360	12639.2520	0	--	0
28	774.4806	1.3876	22.3337	4.0335	15639.1124	4074.5787	0	--	0
19	752.3726	1.4388	23.5478	7.5651	15823.7692	6397.6618	0	--	0
20	725.7595	1.3542	25.5395	3.9808	18424.9031	3558.0395	0	--	0
21	610.5486	0.5855	17.5118	1.7004	11599.0969	836.4948	0	--	0
22	543.0700	0.2560	16.9498	0.6631	31705.6149	1032.8273	0	--	0

ε_{xx}=2.0658(0.0111)	ε_{xy}=0.0043(0.0085)	ε_{yy}=2.0126(0.0107)	ε_{zz}=2.4461(0.0033)

Figure 3.1. Ternary of pyroxene compositions in mole % included in this study.

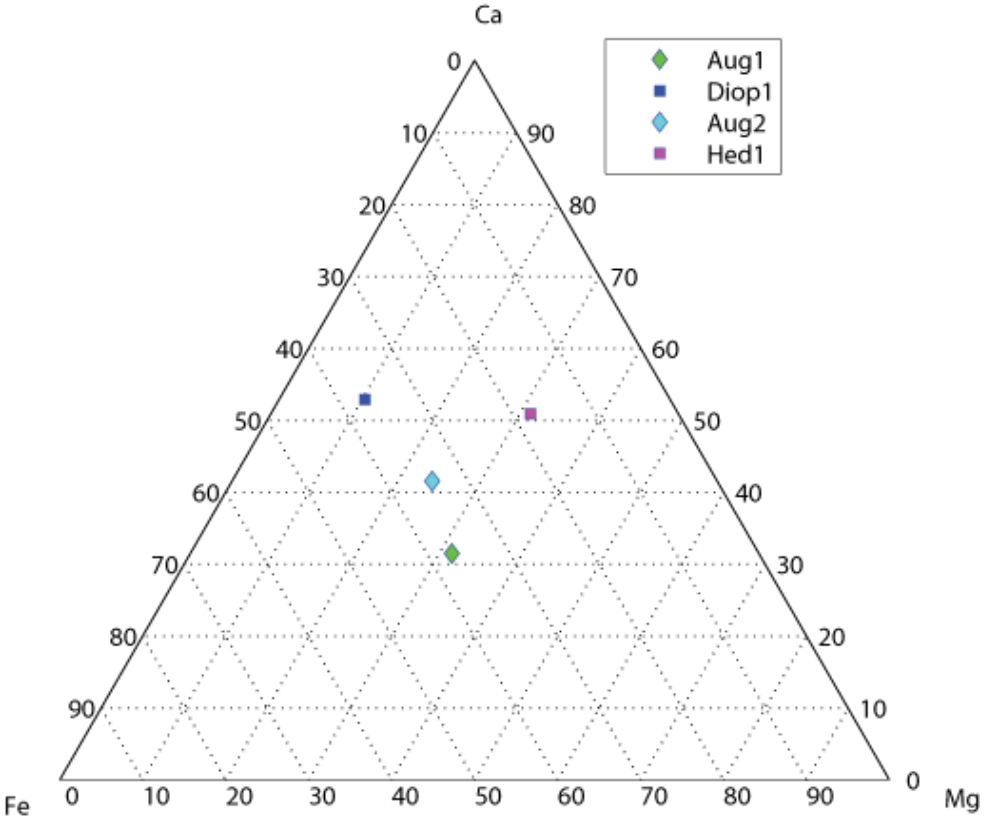

Figure 3.2. Changes in modeled optical constants (*n*, *k*) of orthoclase with initial estimates of ν_j shifted by 30 cm^{-1}.

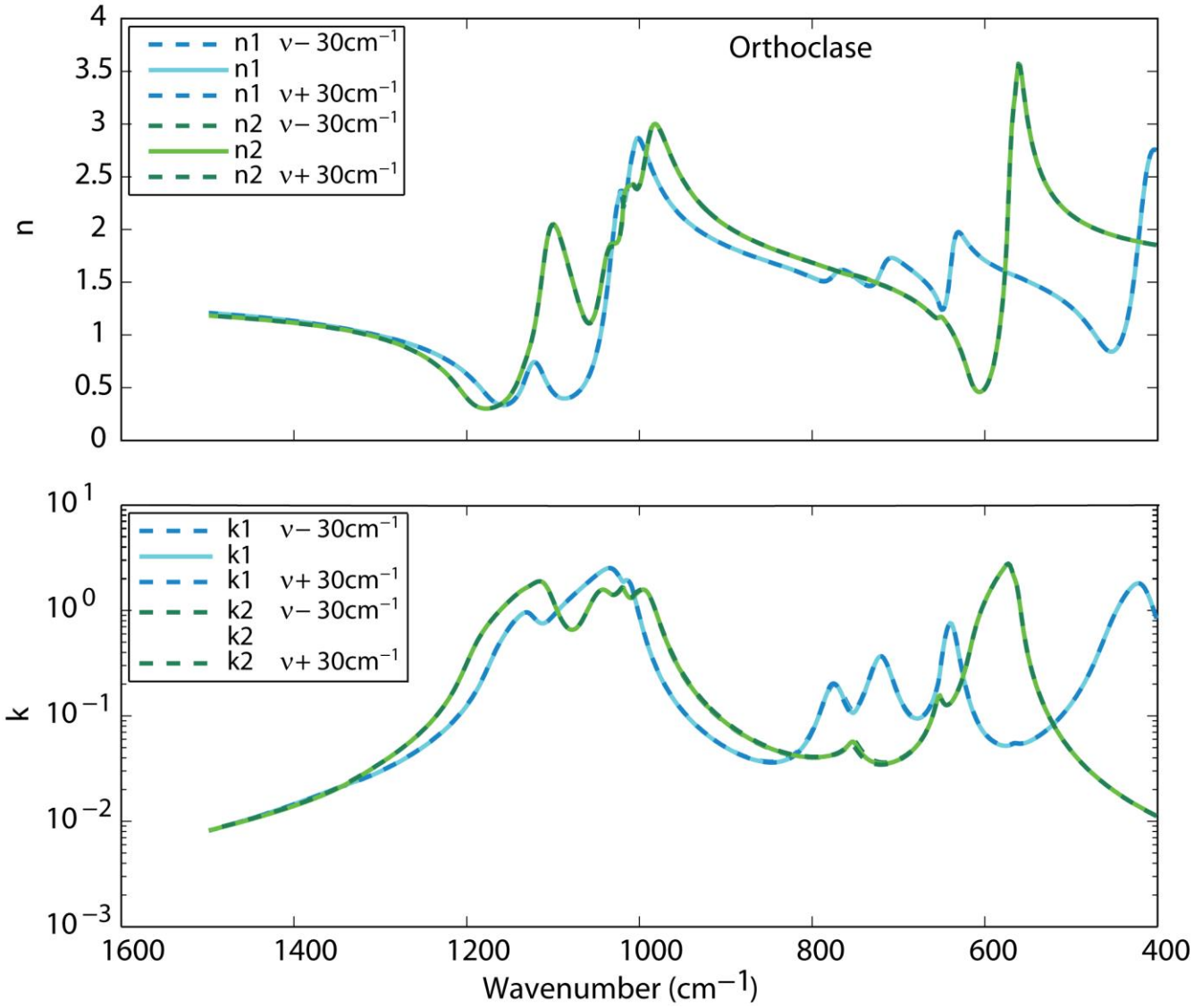

Figure 3.3. Changes in modeled optical constants (*n*, *k*) of orthoclase with initial estimates of γ_j shifted by ±50%.

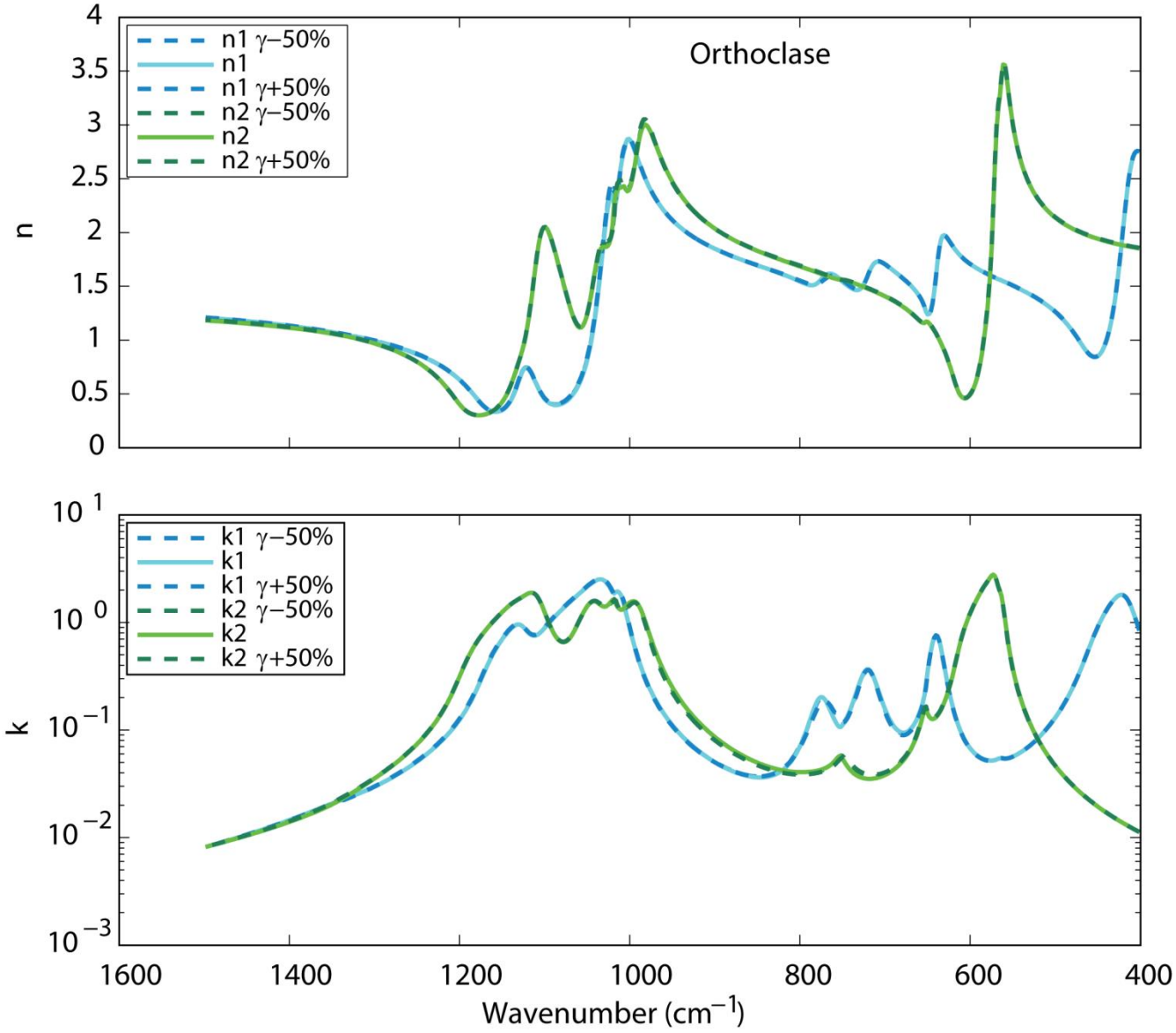

Figure 3.4. Changes in modeled optical constants (n, k) of orthoclase with initial estimates of s_j shifted by ±50%.

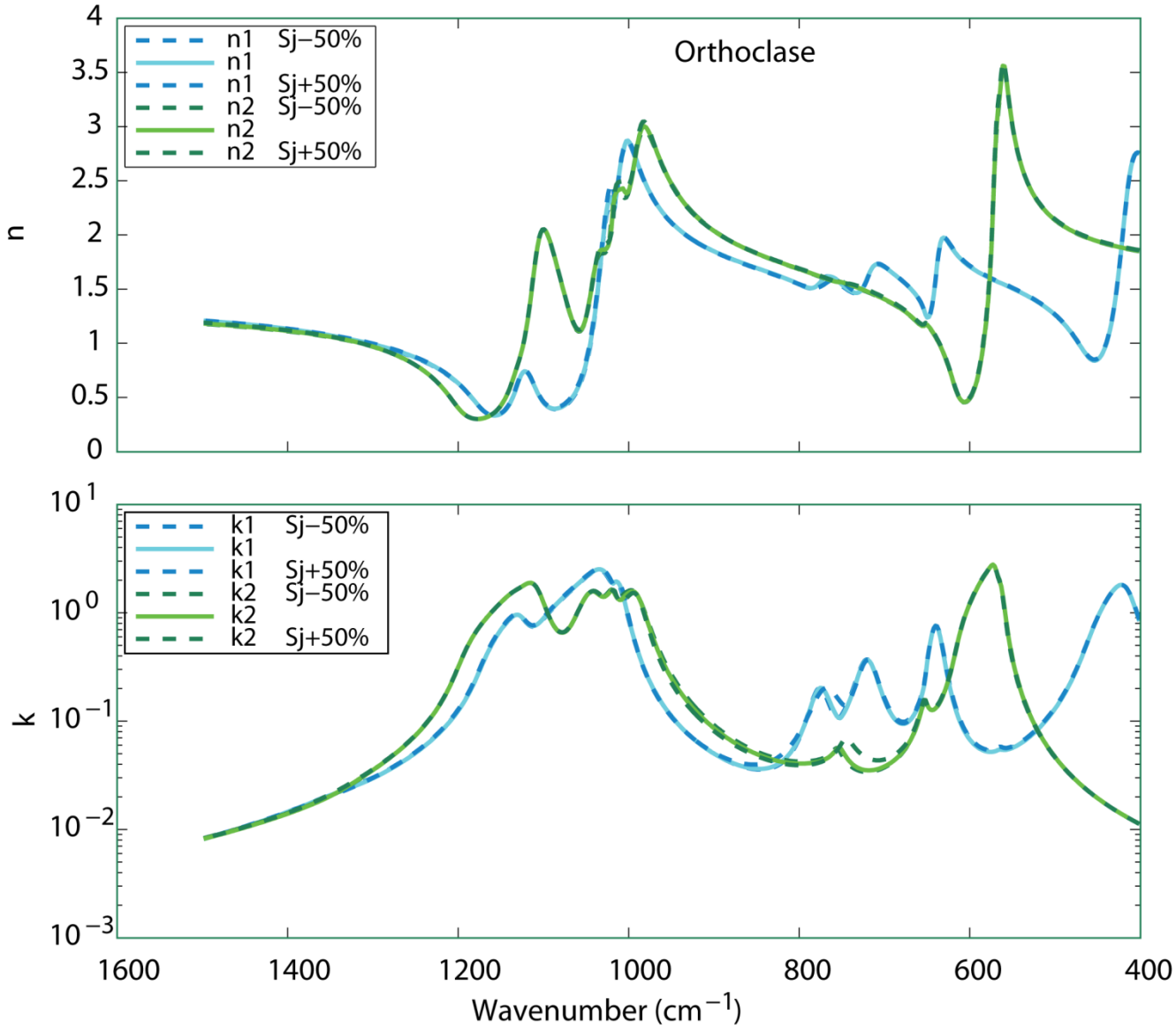

Figure 3.5. Changes in modeled optical constants (*n*, *k*) of orthoclase with initial estimates of φ_j shifted by ±50%.

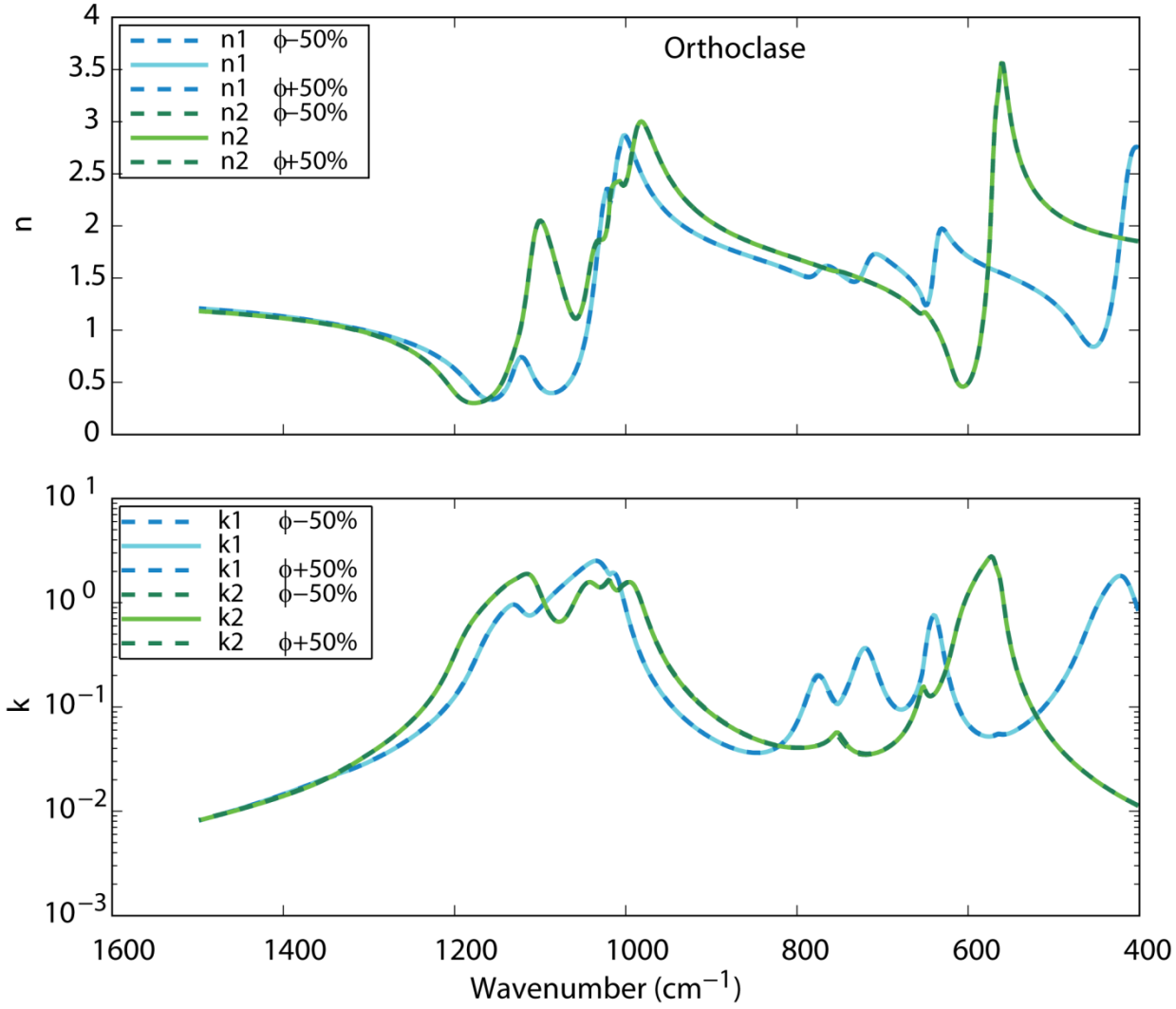

Figure 3.6. Changes in modeled optical constants (*n*, *k*) of orthoclase with initial estimates of ν_j shifted by 30 cm^{-1} and ν_j, γ_j s_j and φ_j shifted by ±50% (top). Optical constants plotted with 95% confidence bounds (bottom).

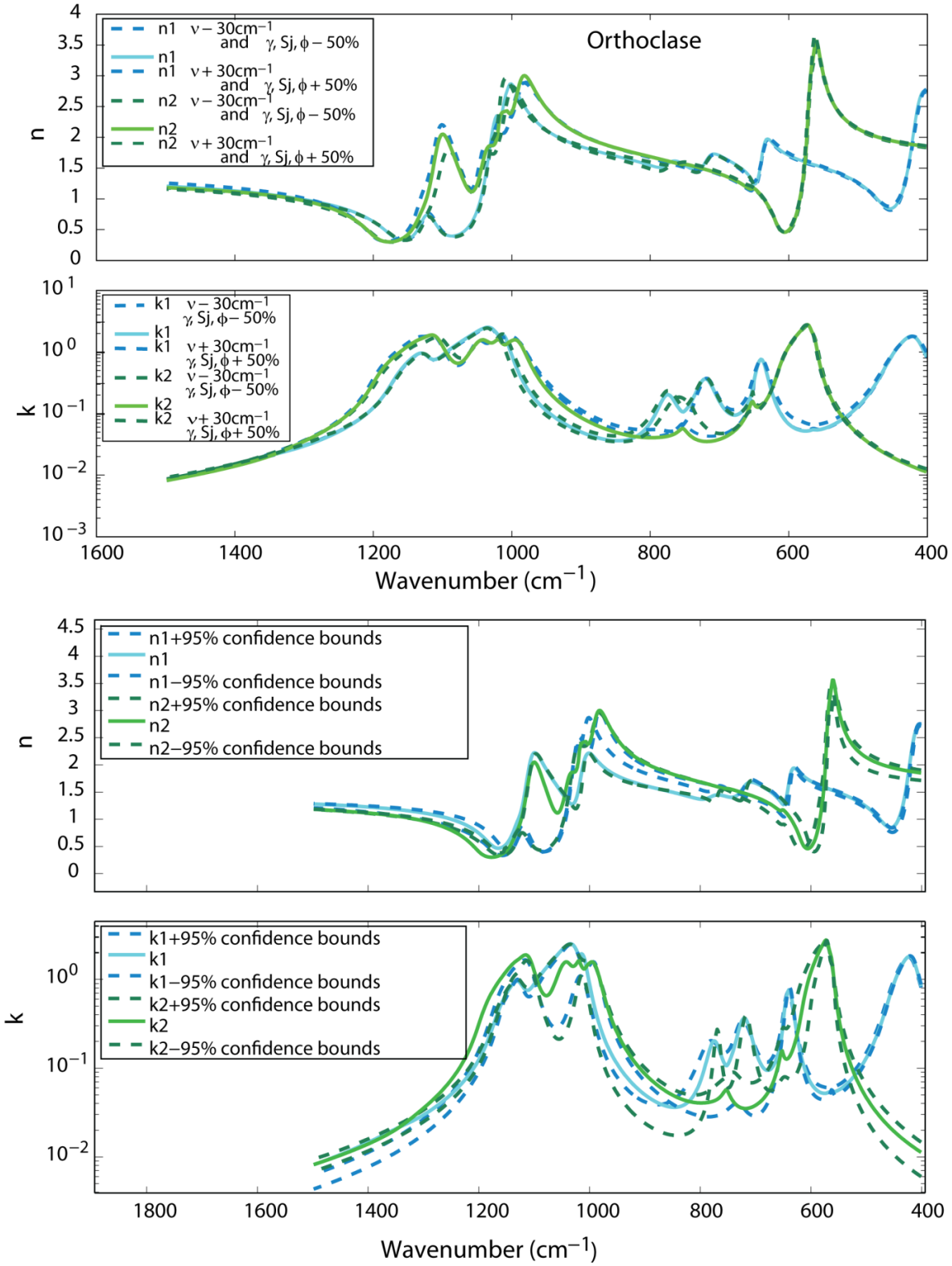

Figure 3.7. Measured and modeled reflectance spectra of augite (Aug1) with incident E-field polarization parallel to *a*-*c* plane at different polarization angles ϕ (top three) and parallel to b (bottom).

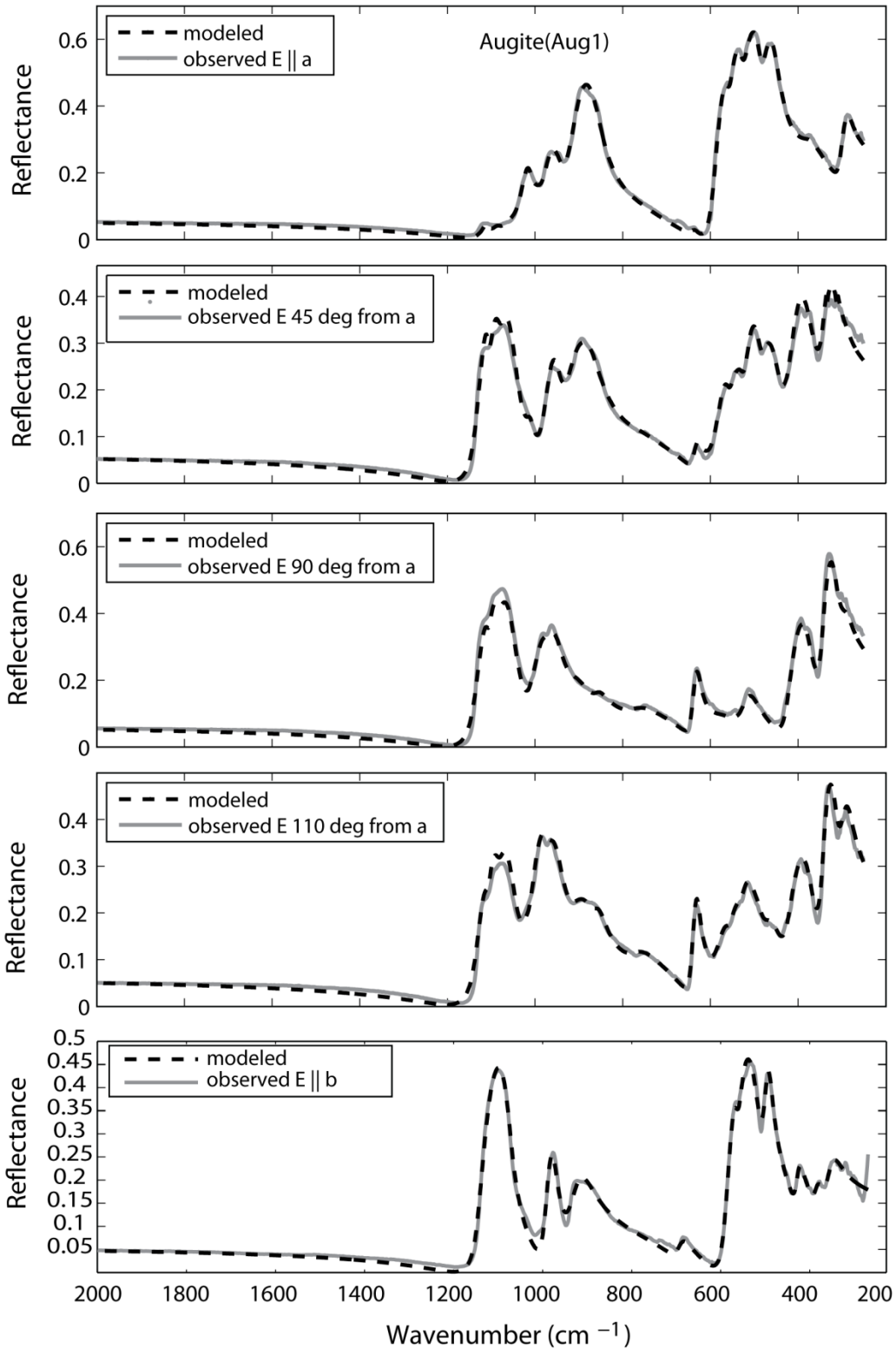

Figure 3.8. Optical constants (*n*, *k*) of augite (Aug1). In this figure, n1, n2 and k1, k2 are the optical constants for the rays whose polarization direction is parallel to the *a*-*c* plane, while nb and kb are the optical constants for the rays with polarization direction along the b crystallographic axis.

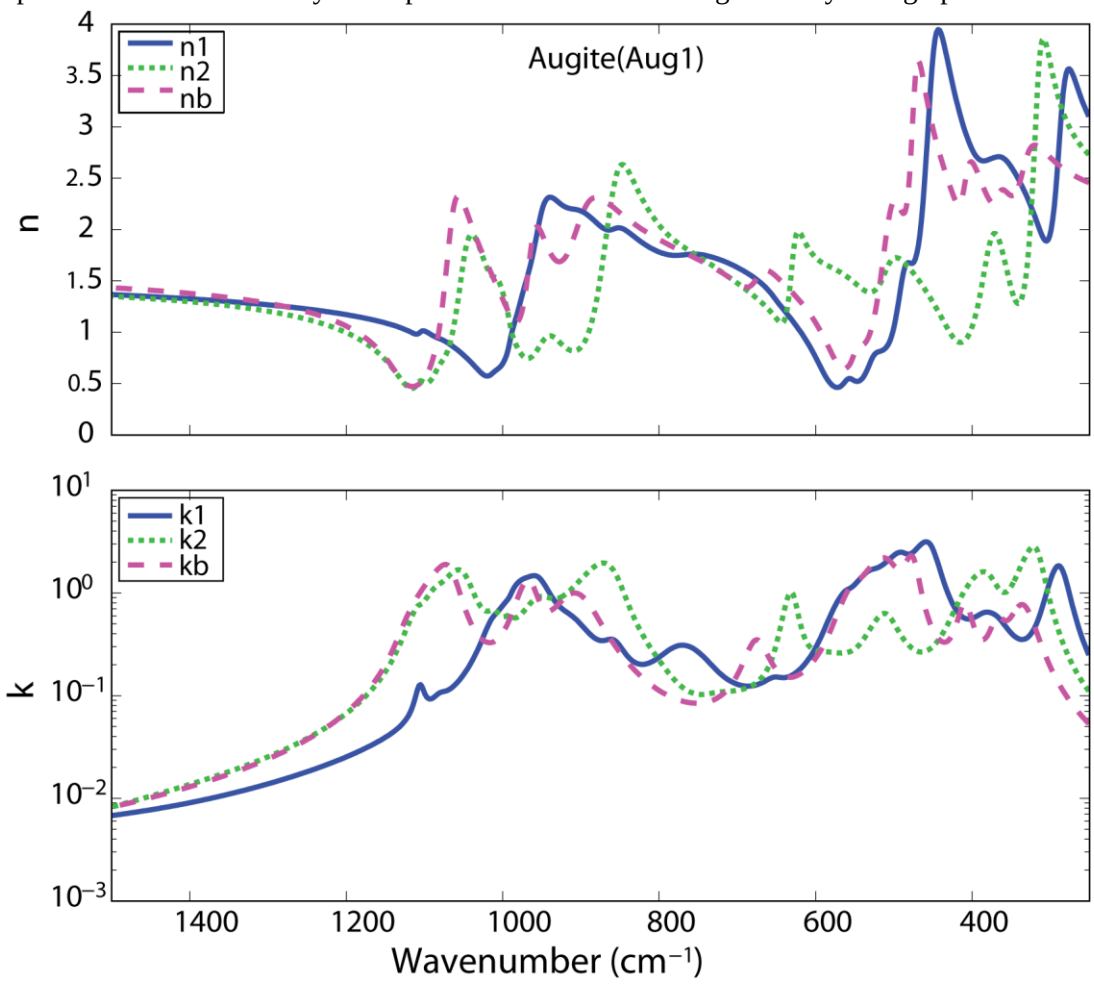

Figure 3.9. Measured and modeled reflectance spectra of augite (Aug2) with incident E-field polarization parallel to *a*-*c* plane at different polarization angles ϕ (top three) and parallel to b (bottom).

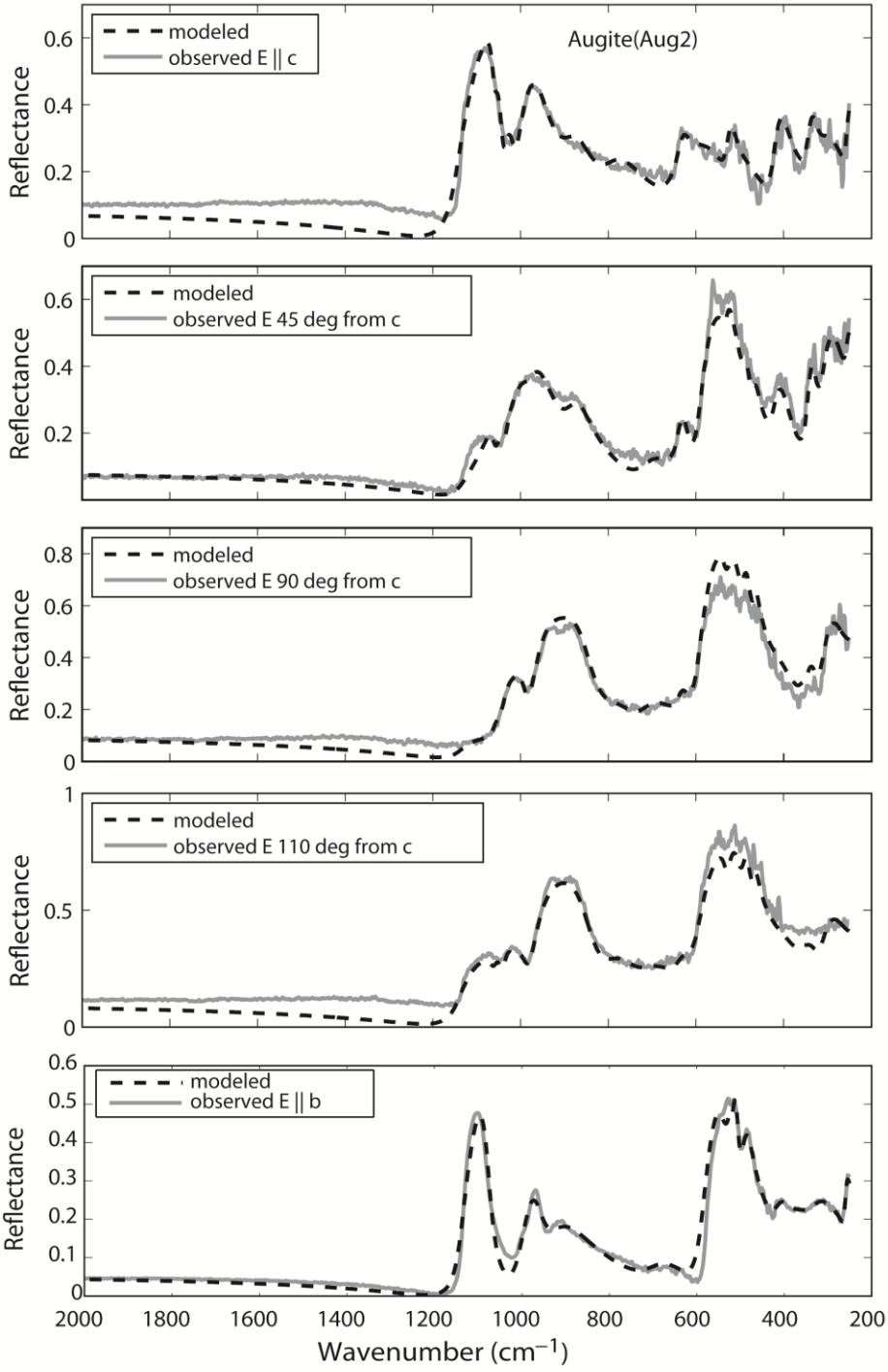

Figure 3.10. Optical constants (*n*, *k*) of augite (Aug2). In this figure, n1, n2 and k1, k2 are the optical constants for the rays whose polarization direction is parallel to the *a*-*c* plane, while nb and kb are the optical constants for the rays with polarization direction along the b crystallographic axis.

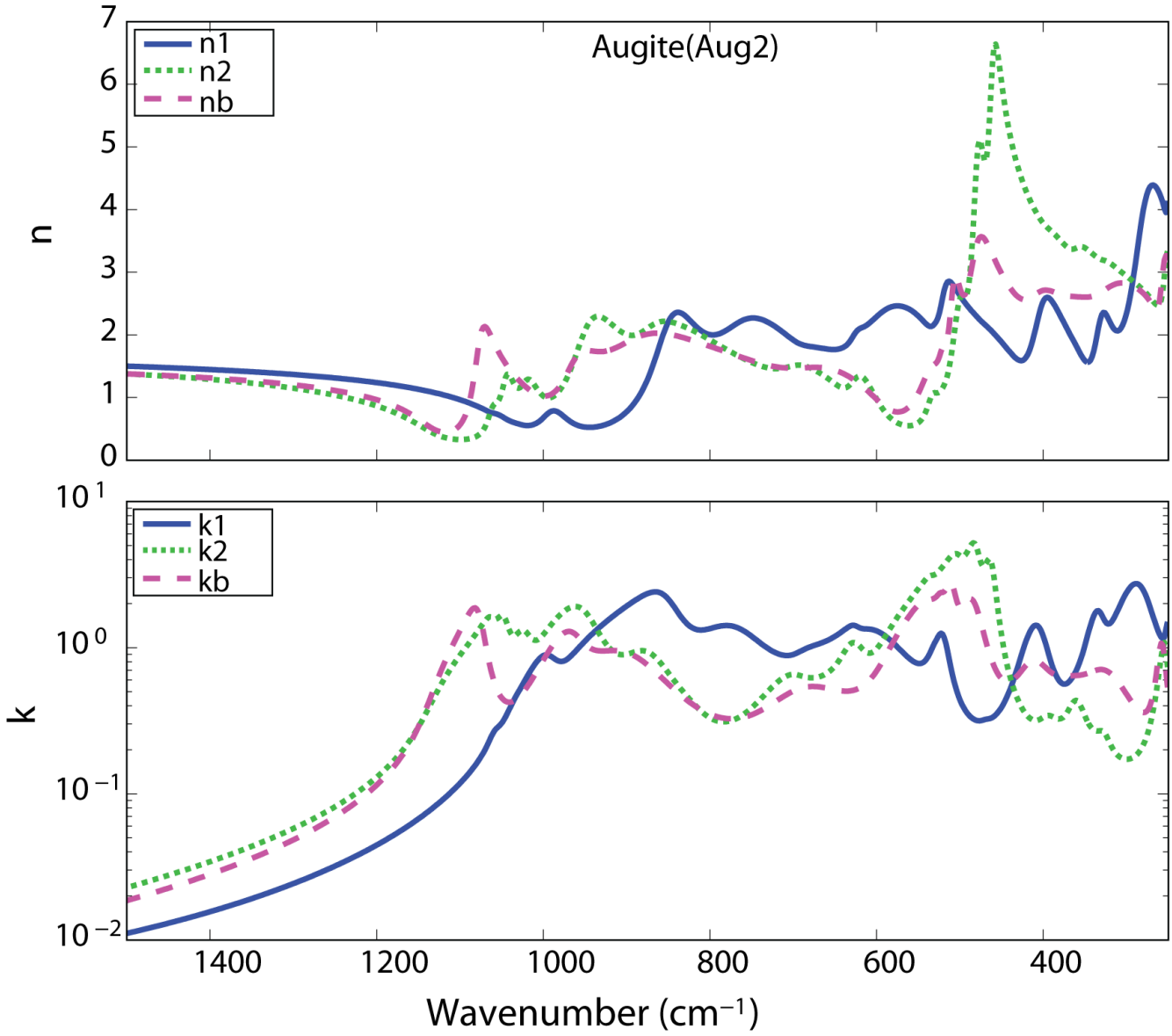

.**Figure 3.11.** Measured and modeled reflectance spectra of diopside (Diop1) with incident E-field polarization parallel to *a-c* plane at different polarization angles ϕ (top three) and parallel to b (bottom).

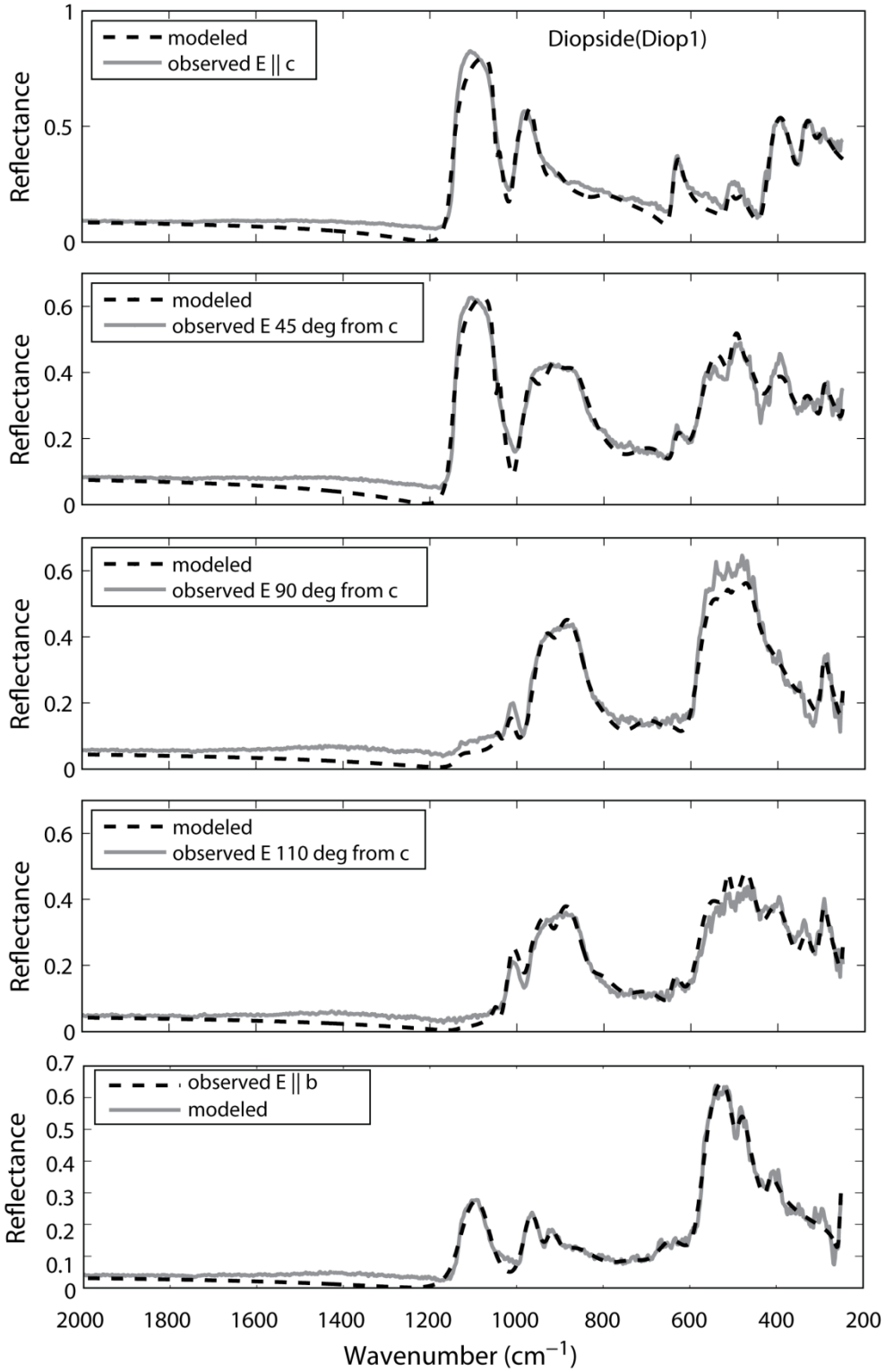

Figure 3.12. Optical constants (*n*, *k*) of diopside (Diop1). In this figure, n1, n2 and k1, k2 are the optical constants for the rays whose polarization direction is parallel to the *a*-*c* plane, while nb and kb are the optical constants for the rays with polarization direction along the b crystallographic axis.

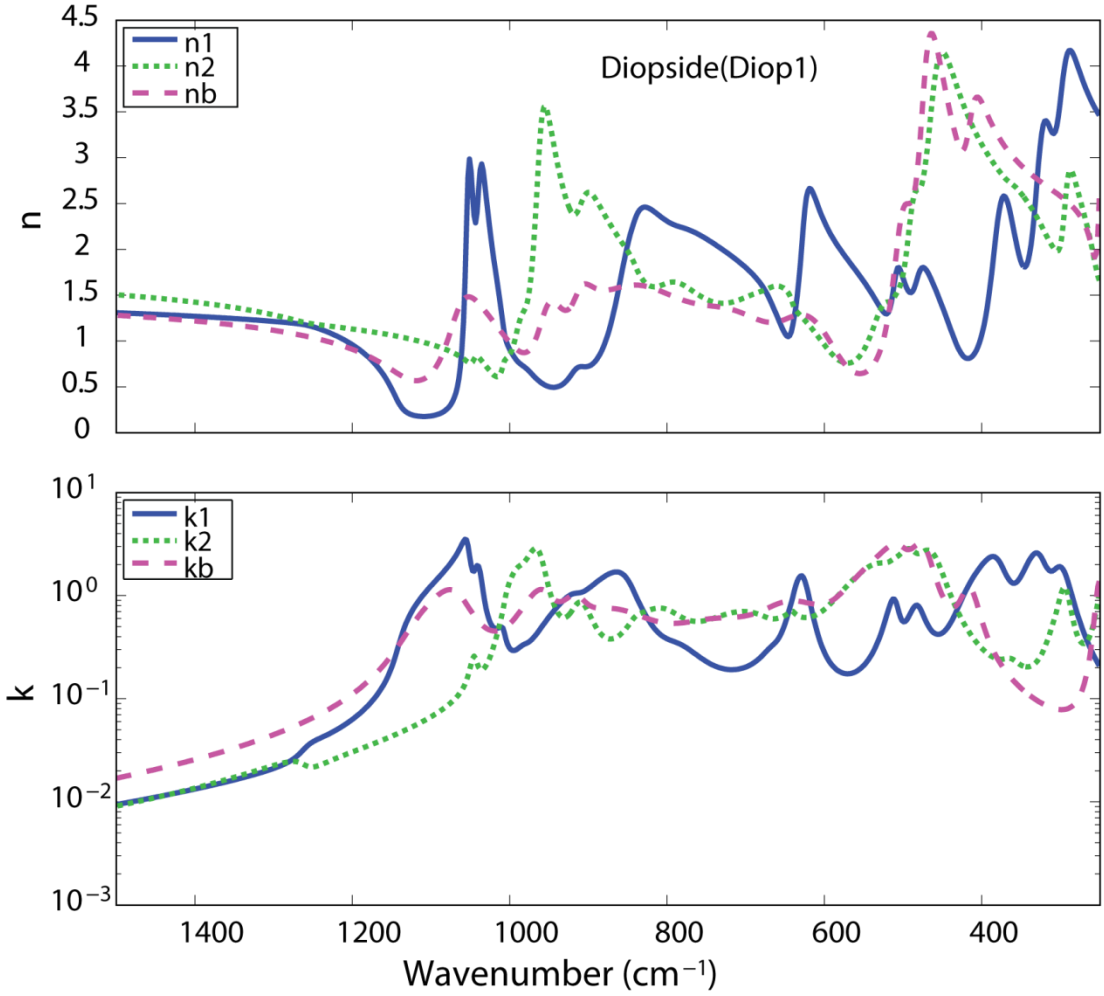

Figure 3.13. Measured and modeled reflectance spectra of hedenbergite (Hed1) with incident E-field polarization parallel to *a*-*c* plane at different polarization angles ϕ (top three) and parallel to b (bottom).

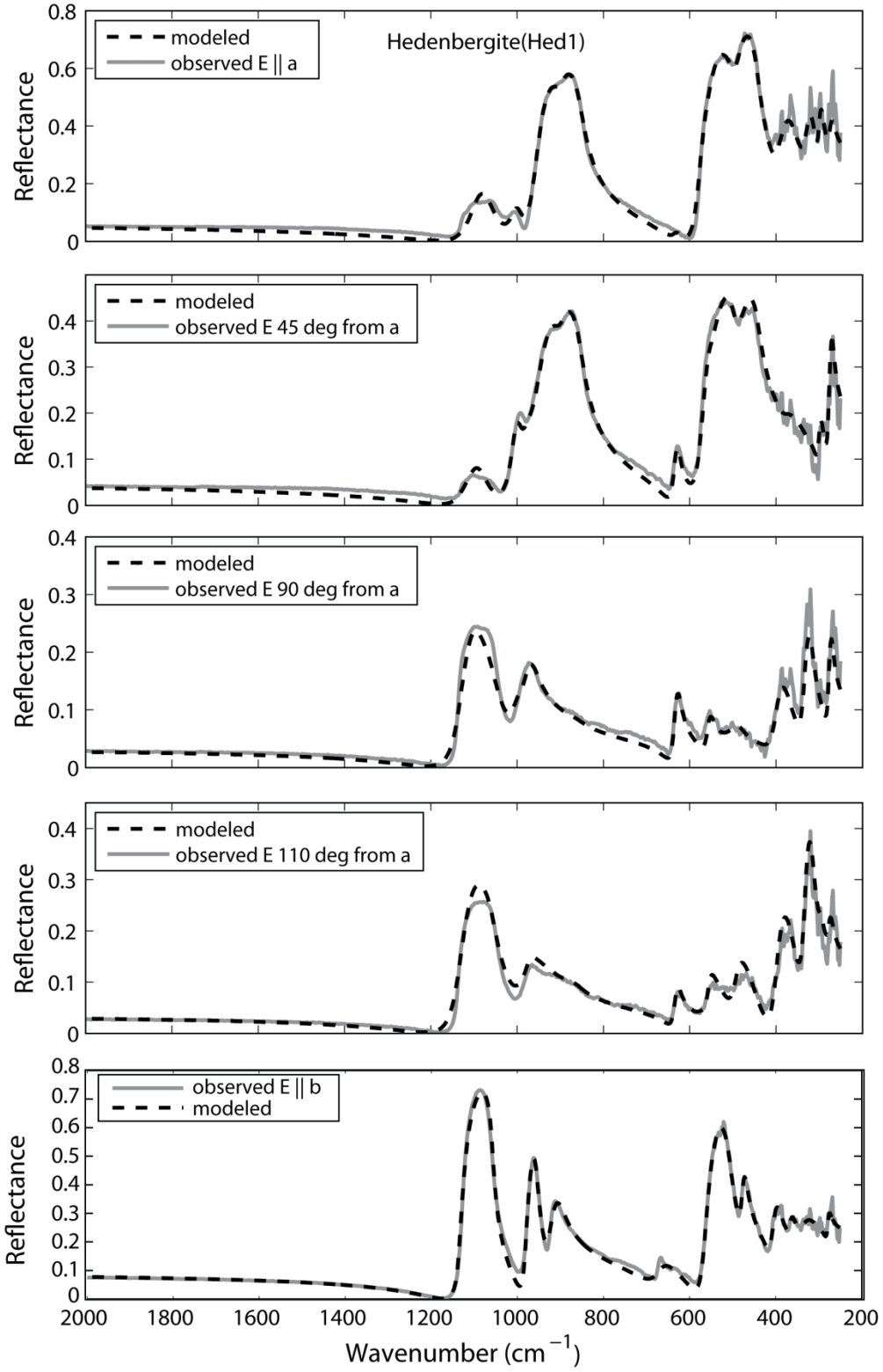

Figure 3.14. Optical constants (*n*, *k*) of hedenbergite (Hed1). In this figure, n1, n2 and k1, k2 are the optical constants for the rays whose polarization direction is parallel to the *a*-*c* plane, while nb and kb are the optical constants for the rays with polarization direction along the b crystallographic axis.

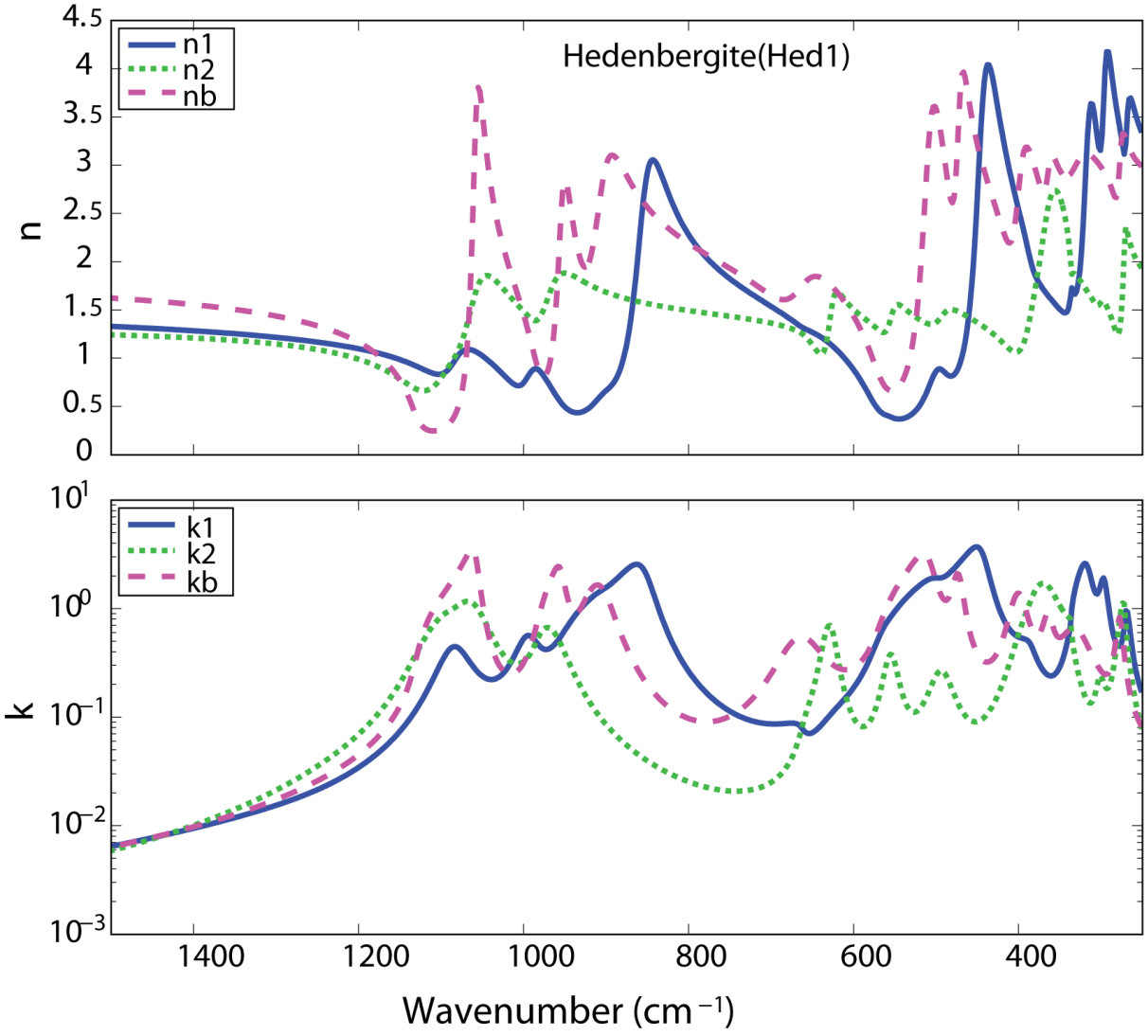

Figure 3.15. Measured and modeled reflectance spectra of orthoclase (Orth1) with incident E-field polarization parallel to *a*-*c* plane at different polarization angles ϕ (top three) and parallel to b (bottom).

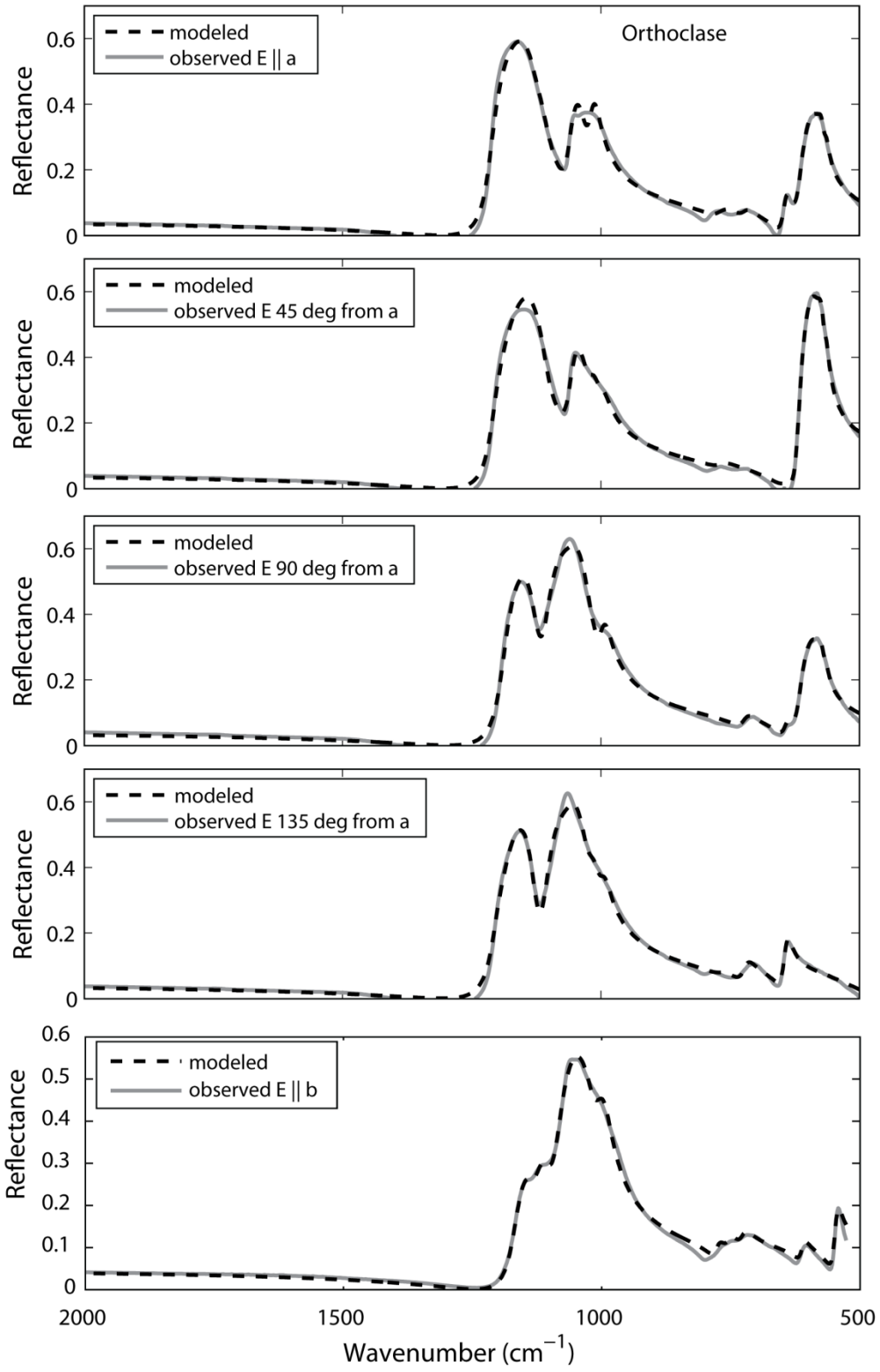

Figure 3.16. Optical constants (*n*, *k*) of orthoclase (Orth1) calculated in this work are in the solid lines (n1,k1,n2,k2,nb,kb), while the optical constants derived in Aronson et al. (1986) are in the dashed lines (na1,ka1,na2,ka2,nab,kab).

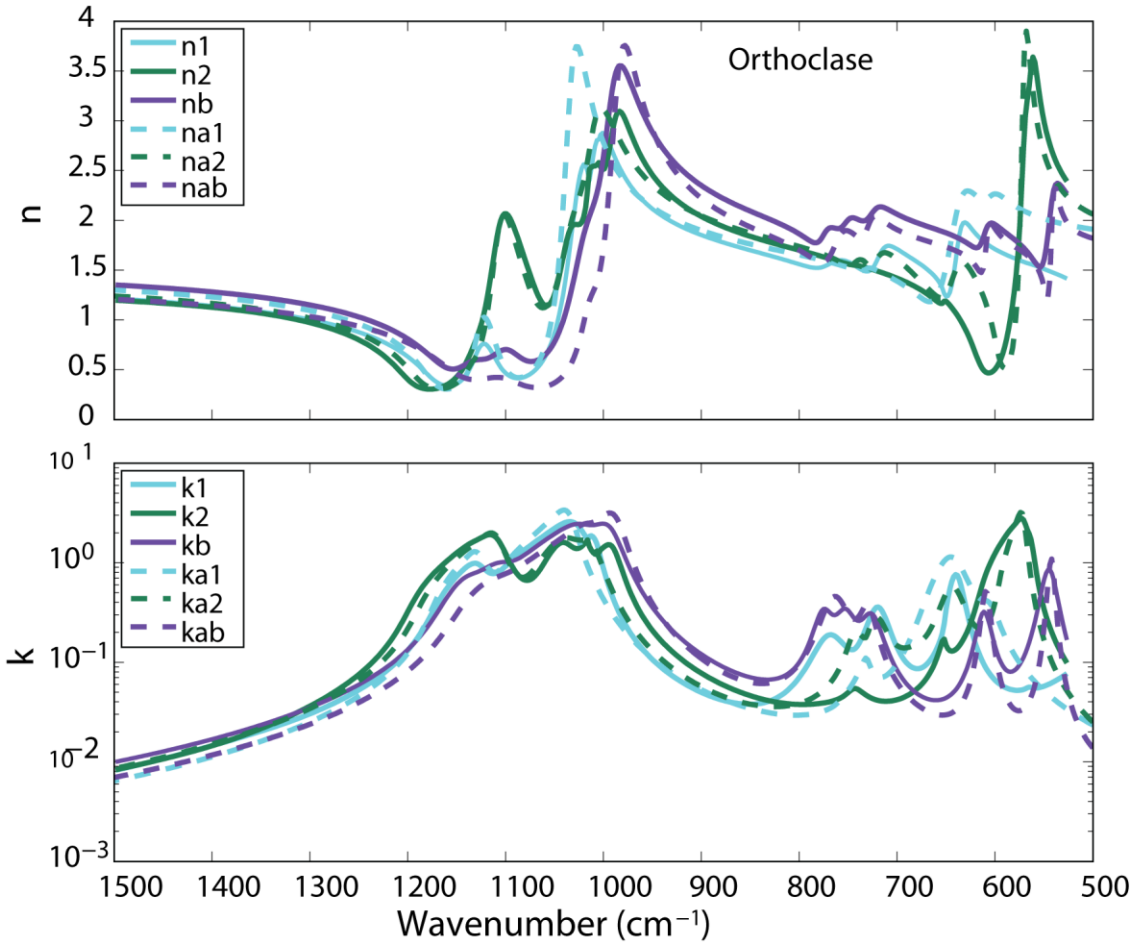

Figure 3.17. Orientation–averaged optical constants in the MIR for several minerals that belong to various crystal systems. Nano-diamonds from a Murchison meteorite (cubic), quartz (hexagonal), olivine (orthorhombic), and diopside (monoclinic).

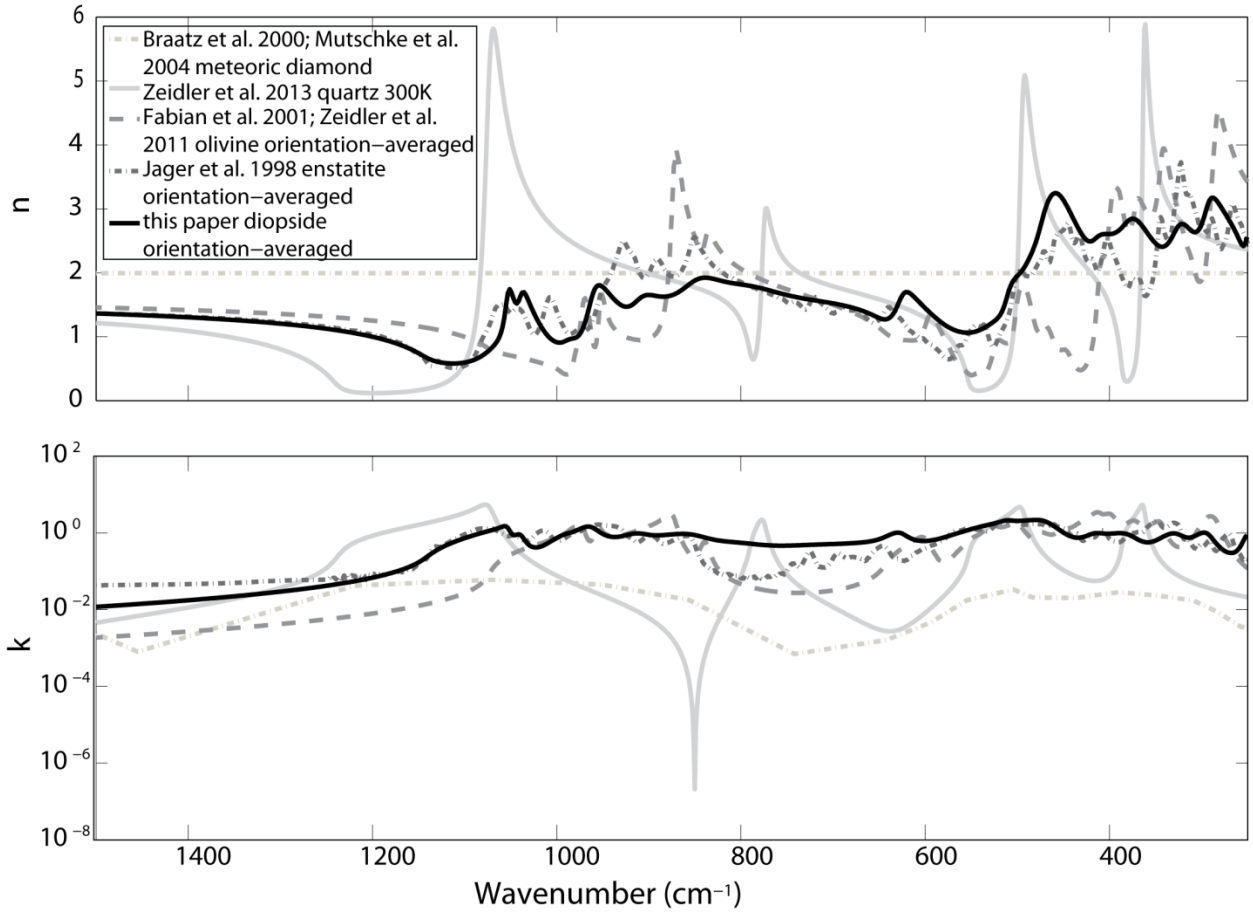

Figure 3.18. Orientation–averaged optical constants (*n*,*k*) of high–Mg olivine ($Mg_{1.9}Fe_{0.1}SiO_4$) from UV to FIR wavelengths (Zeidler et al. 2011). Reflectance spectrum calculated from *n*, *k* values. Labels: Christiansen feature (CF), Reststrahlen bands (RB), highlighted in grey.

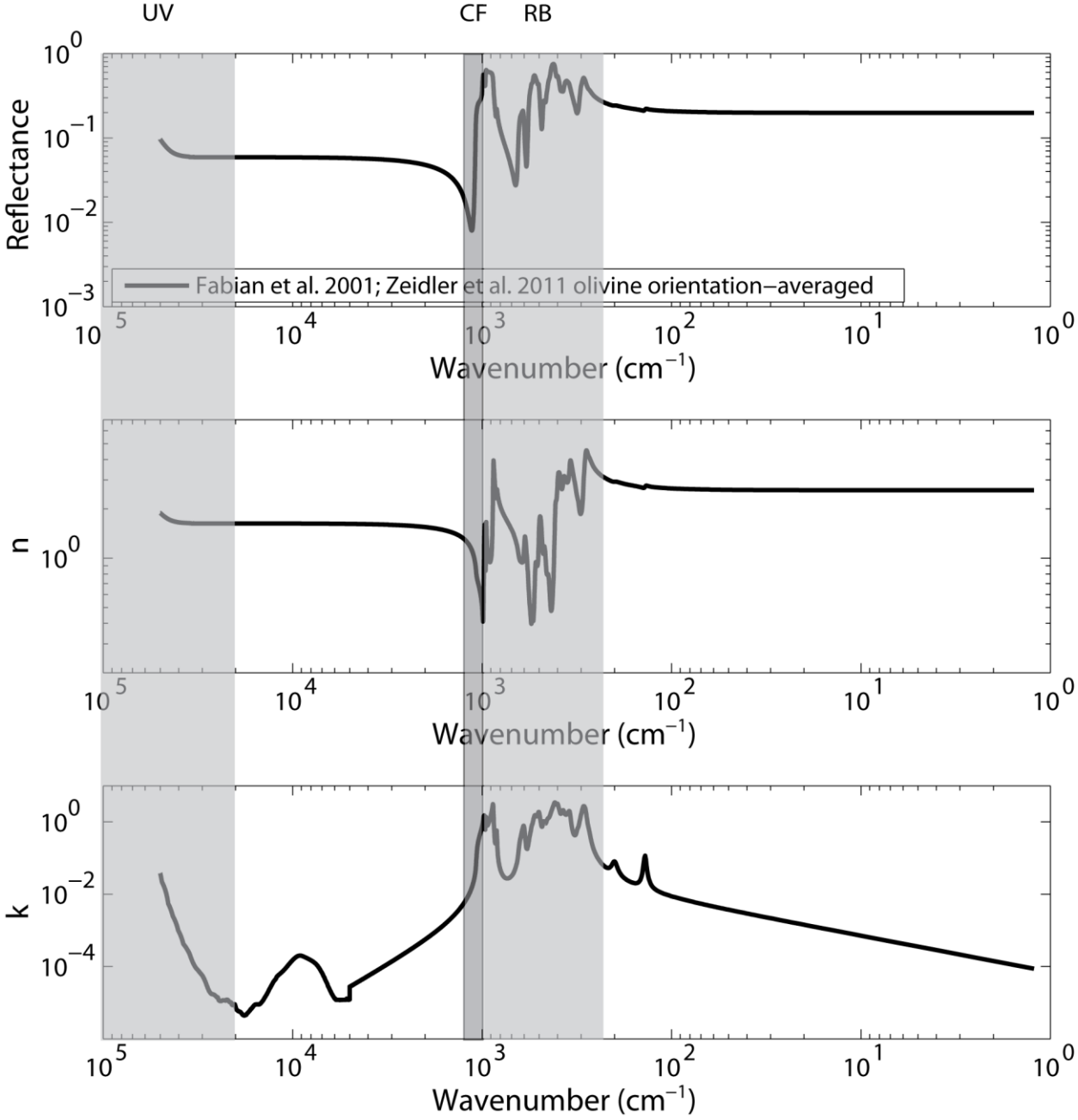

Figure 3.19. A comparison of single–crystal (enstatite and diopside) vs. amorphous (enstatite and a glass of pyroxene composition) pyroxene optical constants.

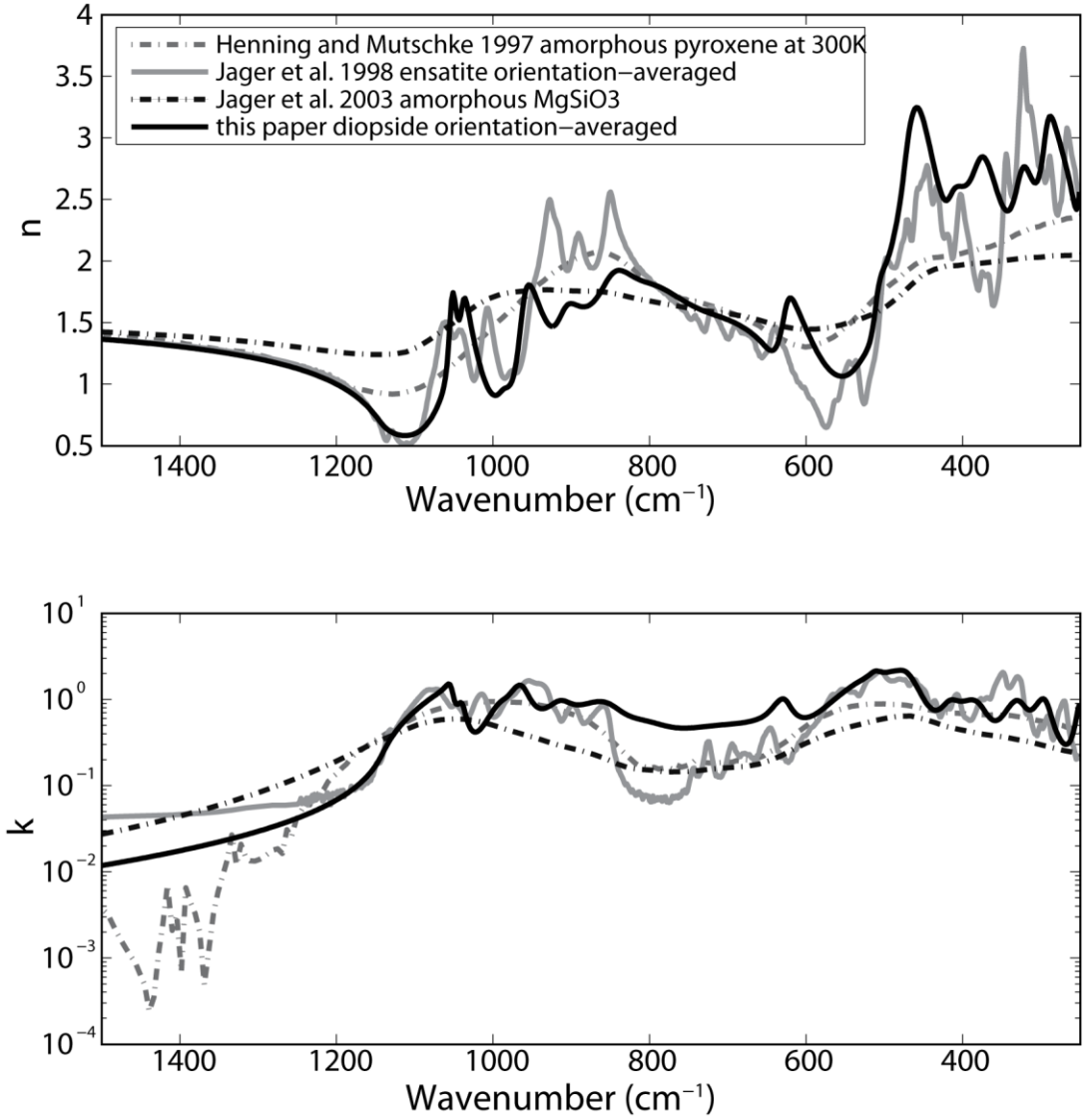

Chapter 4: Lunar olivine as seen by Diviner and M^3: A comparison of MIR and VNIR spectral data

This chapter will undergo minor revisions and be submitted to Geophysical Research Letters with co-authors T.D. Glotch, E.Song, P.G. Lucey, I.R Thomas and N.E. Bowles.

"She borrows light, that, through the night, mankind may all acclaim her!
And, truth to tell, she lights up well; So I, for one, don't blame her."— The Mikado

4.1 Introduction

Locations on the Moon with olivine-bearing, pyroxene-poor lithologies have been detected by visible near-IR (VNIR) instruments such as the Chandrayaan-1 Moon Mineralogy Mapper (M^3) [*Mustard et al.*, 2011; *Pieters et al.*, 2009; *Powell et al.*, 2012] and Kaguya Spectral Profiler (SP) [*Yamamoto et al.*, 2010; 2012]. Prior to this, olivine-bearing exposures had been detected in a handful of areas including the central peak of Copernicus and ejecta of Aristarchus crater with both telescopic data [*Lucey et al.*, 1986; *Pieters*, 1982] and the Clementine UVVIS camera [*Tompkins and Pieters*, 1999].

At VNIR wavelengths, it is straightforward to detect olivine and other mafics in the presence of plagioclase, but relative abundances are difficult determine [*Sunshine et al.*, 1990]. Olivine, pyroxene, and plagioclase all have overlapping bands in the 1-1.3 μm wavelength region that complicate spectral interpretation. Olivine is identified at VNIR wavelengths by three overlapping Fe^{2+} bands near 1.1 μm whose positions shift slightly with Mg# [*Dyar et al.*, 2009;

Isaacson et al., 2014; *Sunshine and Pieters*, 1998]. Pyroxene exhibits two sets of Fe^{2+} bands: one shortward of 1 μm, centered near 900 nm for low-Ca pyroxene and drifting to longer wavelengths with increasing Ca content [*Adams and McCord*, 1972; *Klima et al.*, 2008], and one at 2μm. Crystalline plagioclase has a weak absorption feature that ranges from 1.1 μm to 1.3 μm, depending on composition, with albite at the shortward end of the range, bytownite at the long-ward end, and a value of roughly 1.25 μm for anorthite [*Adams and Goullaud*, 1978]. In lunar samples, this is primarily due to substitution of small amounts of Fe^{2+} for Ca^{2+} [*Pieters*, 1996]. The plagioclase absorption is masked in mixtures by deep absorption features even for small amounts of olivine or pyroxene [*Isaacson et al.*, 2011; *Klima et al.*, 2008]. The 1 μm band of pyroxene diminishes the relative strength of the 1.25 μm band of plagioclase after the addition of only a few weight percent pyroxene [*Ohtake et al.*, 2009]. Although plagioclase, pyroxene and olivine abundances can be derived from VNIR spectra through nonlinear spectral unmixing (typically using the Hapke- or Shkuratov-based implementations of radiative transfer theory), plagioclase abundance tends to be underestimated, while no single phase is correspondingly over-estimated [*Cahill et al.*, 2010].

Because the mid-IR is sensitive to bulk SiO_2 content [*Conel*, 1969; *Logan et al.*, 1973; *Salisbury and Walter*, 1989; *Salisbury et al.*, 1987], we use the unique capabilities of the Lunar Reconnaissance Orbiter Diviner Lunar Radiometer Experiment (Diviner) instrument along with simulated lunar environment laboratory emissivity spectra of plagioclase-forsterite mixtures to constrain the compositions of lunar olivine-bearing regions. Since the Kaguya SP survey [*Yamamoto et al.*, 2010] is the most complete to date, we chose to focus this work on exposures identified by that instrument. *Yamamoto et al.* [2010] report that SP spectra (0.5–2.6 μm) fit with a radiative transfer-based intimate mixture model [*Denevi et al.*, 2008] are consistent with a

"dunite" model containing 45.3%-76.8% Fo_{90} olivine 2.3%-7.8% $Fe_{15}Mg_{85}Ca_0$ orthopyroxene, along with 16.4%-46.9% of an agglutinate component with the same chemical composition as the olivine and orthopyroxene components. Since pyroxene is a minor component in these areas, olivine abundance is estimated from Diviner data using two-component olivine-plagioclase mixtures. Using data from Diviner and our laboratory experiments, we found that some of these areas are significantly olivine-enriched while others, notably Aristarchus, are not substantially enriched in olivine, despite the wide spatial extent of the area exhibiting a 1 μm band in SP and M^3 data. In addition, after applying an albedo-based space weathering correction to the Diviner data [*Lucey et al.*, 2000; *Lucey et al.*, 2010], we find that none of the areas are consistent with concentrations of forsterite exceeding 90 wt%. We applied factor analysis and target transformation (FATT), a principal components-based technique [*Malinowski*, 1991], to M^3 reflectance data of five of our study areas to assess the range of olivine Mg# consistent with these data.

4.2 Data, Methods and Samples

4.2.1 Remote sensing data and methods

4.2.1.1 Diviner instrument and data

Diviner has three channels centered near 8μm located at wavelengths 7.80 μm (Ch 3), 8.25 μm (Ch 4), and 8.55 μm (Ch 5), chosen to help pinpoint the position of the Christiansen feature (CF) that can be used to characterize the silicate mineralogy of the lunar surface [*Greenhagen et al.*, 2010]. Diviner's spatial resolution is ~250 m per pixel. In this work, we also use one of the thermal channels at 12.5-25μm (Ch 6) to define a spectral index that can be used to identify areas of olivine enrichment. The position of the CF is related to the degree of polymerization of the

silicate structure and to a lesser extent, structural changes resulting from cation substitution, resulting in lower wavelength CF positions for tectosilicates such as feldspar (~7.33-7.84μm), and higher wavelength CF positions for orthosilicates such as olivine (~8.5-9.0μm) [*Nash et al.*, 1993]. The CF also changes with particle size [*Logan et al.*, 1973] and space weathering [*Lucey et al*., 2010; Glotch et al., in review]. However, the spectrum of the lunar surface is dominated by the smaller size fractions (<30μm), so that the shift of the CF position with particle size will be much smaller than the shifts due to composition [*Aronson and Emslie*, 1973; *Ruff and Christensen*, 2002; *Ruff et al.*, 1997; *Salisbury and Wald*, 1992]. Other physical properties such as particle packing cause significant changes to the spectral contrast of the reststrahlen bands, but a small impact on the CF position [*Donaldson Hanna et al.*, 2014; *Logan et al.*, 1973]

4.2.1.2 Moon mineralogy mapper (M^3) instrument and data

We used near-IR (430-3000nm) data from M^3 to confirm the location of olivine-bearing regions detected by Kaguya SP [*Yamamoto et al.*, 2010]. SP data covers the 500-2600 nm wavelength range with a spectral resolution of 6-8 nm and a spatial resolution of 500 m per pixel. M^3, a push broom imaging spectrometer, had high spatial (70 m per pixel) and spectral (10 nm sampling) resolution [*Goswami and Annadurai*, 2008]. The M^3 dataset was chosen for two reasons: 1) availability of the dataset and 2) because it is an imager rather than a profiler, the dataset allows direct regional comparison to Diviner.

4.2.1.3 M^3 and Diviner data processing

For each area of interest, we generated index maps of the 1- and 2-μm integrated band depths from the relevant M^3 reflectance data. Band depths are calculated by summing the difference between the actual reflectance and the continuum as fit by a line over the absorption band

[*Mustard et al.*, 2011]. We used the accompanying M^3 location files to extract the coordinates of spots with a high 1-μm band depth index value, but low 2-μm band depth index and a large enough spatial extent to be visible at Diviner's spatial resolution. Using M^3 locations of these spots as a guide, we then extracted mid-IR emissivity derived from Diviner radiance measurements for all locations where data was available. To minimize thermal effects, we only used daytime data constrained to less than 50° latitude from the equator and applied a solar incidence angle correction as described in [*Greenhagen et al.*, 2011]. Even with the latitude and daytime spatial coverage restrictions, Diviner data is available for 27 of the 33 SP regions of interest. Some locations had a few areas of interest within the M^3 data near the SP spots, and including these, we collected CF data for 45 total spots. We binned the Diviner data at either 128 or 256 pixels per degree for regional analysis. Emissivity data was obtained by dividing the measured radiance of each channel by the black body radiance of the maximum brightness temperature of all the channels for each pixel. Diviner emissivity and M^3 reflectance spectra were extracted from and averaged over polygons covering nearly identical spots on the lunar surface (Figure 4.1). We used visible wavelength images from the Lunar Reconnaissance Orbiter Camera (LROC) Wide Angle Camera (WAC) to verify the location and make small adjustments (a few pixels) to the area of Diviner data extraction when necessary.

4.2.1.4 FATT method

FATT was used to determine if olivine composition (Mg #) can be constrained using the M^3 dataset. Factor analysis is a principal components-based approach of spectral analysis that assumes that spectra within a scene can be reproduced by linear addition of components. We use R-mode factor analysis [*Malinowski*, 1991] to reduce M^3 spectra into mutually orthogonal eigenvectors, each of which has an associated eigenvalue. Eigenvalues are used to rank the

relative importance of each eigenvector derived from the data in the scene. The maximum possible number of components is equal to the number of samples in the spectrum, but only the number of components needed to reproduce the original spectra within the noise level is chosen for comparison with library spectra. Typically for a hyperspectral data set, less than 10 eigenvectors are needed, which greatly reduces the dimensionality of the data set. Once the relevant number of eigenvectors has been selected through factor analysis, the target transformation technique produces linear least-squares fit to the library spectrum using the set of eigenvectors. If a library spectrum can be adequately reproduced by target transformation, it is a possible end-member. While this technique has typically been used for mid-IR data sets [*Bandfield et al.*, 2000; *Glotch et al.*, 2006; *Malinowski*, 1991], it has also recently been shown to be effective for the analysis of hyperspectral VNIR data sets [*Che and Glotch*, 2014; *Friedlander and Glotch*, 2014; *Thomas and Bandfield*, 2013].

4.2.2 Lunar environment laboratory data, methods and samples

The thermal environment created by vacuum conditions results in substantial changes in the characteristics of emissivity spectra when compared with ambient or even martian (~6 millibars) surface pressures [*Logan et al.*, 1973; *Salisbury and Walter*, 1989]. These changes include an increase in spectral contrast with decreasing pressure and deepened absorption in the reststrahlen band region, which results in a CF shift to shorter wavelengths [*Logan et al.*, 1973; *Nash et al.*, 1993]. Within solid materials or finely particulate materials under a substantial atmosphere, conduction is the dominant form of heat transfer. This is not the case for finely particulate materials under very low pressure conditions, where the observed increase in spectral contrast is due to steep thermal gradients produced by radiative cooling at the surface. [*Henderson and Jakosky*, 1994; *Logan et al.*, 1973]. To characterize these effects, several researchers have

measured simulated lunar environment (SLE) spectra for mineral end-members [*Donaldson Hanna et al.*, 2012; *Greenhagen et al.*, 2010] and assessed the changes in CF within the plagioclase solid solution series [*Donaldson Hanna et al.*, 2012].

In this work we address the behavior of changes in CF for mineral mixtures under simulated lunar conditions. In order to understand how the CF position responds to mixture composition, we have acquired laboratory emissivity spectra of fine-grained (< 63μm) two-component mixtures of anorthite/forsterite and anorthite/augite of varying anorthite weight percentages in a lunar environment chamber. Details of the sample preparation, data acquisition, and calibration are described in *Thomas et al.* [2010].

The olivine sample used in this study consists of millimeter-sized forsterite grains from San Carlos, AZ obtained from Ward's Science and was determined by electron microprobe analysis to be roughly Fo_{93}. Augite was obtained from Ward's and its composition was measured with both electron microprobe and powder x-ray diffraction. The anorthite sample consists of ~1 cm single crystals and originated from Miyake Isla, Japan. Based on the measured CF, the anorthite is ~An 80-90. The pure minerals were ground and dry-sieved to < 63 μm. Seven samples were prepared ranging from 100 wt.% anorthite to 100 wt.% olivine and 4 samples ranging from 100 wt.% anorthite to 100 wt.% augite (listed in Table 1).

We acquired laboratory emissivity measurements in two configurations for each sample (Figure 4.2). First, an ambient temperature spectrum was acquired in a 1 bar N_2 atmosphere with the sample cup heated from below to 80 °C and no illumination. Then a simulated lunar environment (SLE) spectrum was acquired at high vacuum pressure ($<10^{-3}$ mbar) with the

chamber cooled to ~ –120 °C, the sample cup heated from below to 120 °C, and a lamp illuminating the sample from above.

4.3 Results

4.3.1 Comparison of laboratory and remote sensing data

For direct comparison between laboratory and Diviner remote sensing data, we convolved the full-resolution spectra to Diviner's filter functions for Channels 3-9. We calculated the CF position of each mixture based on the convolved emissivities in the same manner as the Diviner data. Full spectral resolution SLE spectra of the end-members and mixture samples are shown in Figure 4.2a and convolved spectra are shown in Figure 4.2c. In both ambient and SLE conditions, the spectra and calculated CF's deviate from a linear mixing trend; however the shape of the CF curves are different in each case (Figure 4.2d). Though the calculated CF's of the SLE mixture spectra are close to the linear mixing trend derived from the end-members for lower weight percentages of anorthite, there is a significant departure for greater than 50 wt. % anorthite. This could be due to the high albedo of pure anorthite, which makes it difficult to reach the desired sample temperature, thus affecting the acquired emissivity spectrum.

4.3.2 Plagioclase-olivine ratios from Diviner CF

Most olivine-enriched areas that we have investigated have a weak or absent 2μm band in the VNIR spectra, indicating that these regions have low pyroxene abundances, allowing us to model them as a two-component olivine-plagioclase system based on the SLE laboratory data. Space weathering processes impact the CF position, shifting it to longer wavelengths with increasing optical maturity [*Lucey et al.*, 2010]. To account for this, we applied an optical maturity

correction derived from Kaguya multiband imager (MI) 750nm and 950nm albedo data [*Lucey et al.*, 2010] to the Diviner CF. This is an updated version of the Clementine optical maturity (OMAT) index, which is based on a linear relationship between the 950 nm/750 nm ratio and the 750 nm reflectance for lunar soil samples. More mature lunar soils trend towards the redder (higher 950 nm/750 nm ratio) and darker (lower 750 nm reflectance) end of this linear relationship [*Lucey et al.*, 2000]. The empirical correction to the CF based on the OMAT index is CF_{corr}=CF+OMAT-0.4. This correction brings the Diviner CF values in line with measured laboratory values of immature lunar soils. The anorthite abundance versus SLE CF plot (Figure 4.2d) was fit with the Matlab piecewise cubic interpolation (pchip) function. We used the resulting abundance versus CF curve to estimate olivine abundance from the Diviner CF. Based on this rough estimate, the areas in this study have a wide range of calculated olivine abundances, ranging from ~25% up through >85% (Figure 4.3). These numbers represent *upper limits*, as the CF of more fayalitic olivine occurs at longer wavelengths, driving down the necessary abundance of olivine to produce the observed CF position. Figure 4.3a shows how these abundance estimates change if the olivine end-member is more Fe-rich, with a CF position of 9 μm. We assess the likelihood of the presence of lunar Fe-rich olivine in section 4.3.3.

4.3.3 Factor analysis and target transformation (FATT) and olivine spectral index

We used the SLE laboratory data to develop a spectral index for olivine, which includes the longer-wavelength Diviner Channel 6 (12.5-25μm). Although Ch 6 is relatively broad-band, it occurs within a wide region of absorption due to the reststrahlen bands (RB) and transparency features of these minerals, and can be used to give some indication of the shape of this region. See Figure 4.2 for comparison of full resolution lunar environment emissivity spectra with the ranges of Ch 3-5 and Ch 6. Using a concavity index similar to that of *Glotch et al.* [2010a], but

for Ch 4, 5, and 6 rather than Ch 3, 4, and 5 (see Figure 4.4a and 4.4b), we found that pure anorthite is strongly concave up (negative index value), pure augite is weakly concave down (small positive index value), and olivine is strongly concave down (larger positive index value). While this index cannot be used to directly calculate abundance, it is a useful method for locating areas of relative olivine enrichment. Figure 4.5 shows side-by-side maps of this index and CF position for the southeast rim of Aristarchus. Figure 4.6 is a plot of Ch 456 index versus CF for the same region.

We also applied the FATT technique to M^3 spectra of five of our study areas, one of which is consistent with a high (>90) Fo# olivine, and three of which have visual fits and RMS values that are consistent with a wide range of values (~Fo50-90). While the synthetic Fo_{100} laboratory spectrum typically gives the lowest RMS errors, this may simply be due to the near absence of any 1 μm bands, making it easy for the target transformation algorithm to fit this spectrum. See Table 4.2 for RMS values and appendix 4.A for FATT fits. The remaining area in the Nectaris basin has a high estimated olivine abundance of 85% based on our SLE emissivity data for forsterite, so we expect this site to contain more Fe-rich olivine. Fits of FATT-derived end-members for this region confirm this, with low RMS values and the best model fits by visual inspection for compositions less than Fo_{30}.

4.4 Discussion

While the olivine used in this study has a composition of Fo93, lunar olivine consists of a wide range of Fo# e.g., mare basalts (Fo30-80) [*Lucey et al.*, 2006], alkali-suite (Fo40-80), Mg-troctolite (Fo73-90) and dunite (Fo87-89) [*Wieczorek et al.*, 2006]. Fayalite has a CF position long-ward of Ch 5 (8.55 μm) and would be distinguishable by its concave up spectral shape in Ch 3-5, with Ch 5 emissivity greater than Ch 3 [*Greenhagen et al.*, 2010]. Both the longer-

wavelength CF position and unique spectral shape would lower the threshold for olivine detectability by Diviner. However, the only region consistent with lower-Fo# olivine that has been identified so far is the small crater within the Nectaris basin described in Section 4.3.3.

Previous studies have looked at the distribution of olivine-bearing lithologies, showing that they are concentrated near the edges of large impact basins, mostly within the ejecta, walls, and central peaks of small impact craters [*Powell et al.*, 2012; *Yamamoto et al.*, 2010; 2012]. Here, we characterize the olivine abundance at the locations reported in *Yamamoto et al.* [2010] and find that there is a wide range of olivine/plagioclase ratios, most of which are comparable to troctolite (10-60% plagioclase, 40-90% olivine, and less than 10% pyroxene). Possible mechanisms for the occurrence of these rock types at the lunar surface include: 1) exposure of the olivine-rich lunar mantle through impact processes, or 2) intrusion of olivine-rich plutons into the crust that have been excavated by impacts.

Yamamoto et al. [2012] favor the first option and suggest a sequence of events that could bring olivine-bearing, upper mantle material to the lunar surface: (1) some basin-forming impacts were large enough to melt material from the crust and upper mantle [e.g. *Stewart*, 2011]; (2) differentiated melt sheets were produced with olivine-rich materials at the bottom; (3) subsequent impacts excavated material from the lower layers of the melt sheet, exposing them at the surface. This model would explain the patchy distribution of these olivine-enriched sites.

An additional constraint on olivine detection in the VNIR is that these surfaces must be relatively fresh, or the 1μm band will be diminished by space weathering processes. *Yamamoto et al.* [2012] suggest this is another possible reason for the heterogeneous distribution of VNIR olivine detections. However, a surprising result from Diviner is that in the mid-IR, space

weathering has a tendency to drive the CF to longer wavelengths [*Greenhagen et al.*, 2010; *Lucey et al.*, 2010]; this effect was not expected [*Nash et al.*, 1993; *Salisbury et al.*, 1997]. Therefore, if there were large amounts of heavily space-weathered olivine-rich material, we would expect areas with anomalously high CF values, but weak or absent 1μm absorptions. This has not been observed anywhere on the lunar surface to date.

The second possible mechanism is that the olivine-bearing regions originate from Mg-suite plutons that were excavated by impacts. A large number of models for the both the formation of the Mg-suite and the troctolites in particular, have been proposed [*Griffiths and Campbell*, 1990; *Hess*, 1994; 1998; 2000; *Longhi*, 2003; *Ryder*, 1991; *Ryder et al.*, 1997; *Shearer and Papike*, 2005]. The main difficulty that has led to the profusion of models is the incorporation of a KREEP-like concentration of incompatible elements, while retaining a high Mg/Fe ratio. A hybrid source model for Mg-rich magmas such as the one suggested by *Elardo et al.* [2011] is another possibility.

Hess [1994] reviews the problems with the Mg-suite formation models that had been proposed to date, and considers an impact origin as an alternative [*Grieve et al.*, 1991]. However, *Hess*[1994] does not favor the impact scenario because it would not explain the gap in An# versus Mg# trends between the ferroan anorthositic suite and the Mg-suite, although it is possible this gap would close if we had more samples.

In summary, it is difficult to distinguish between 1) the crystalized product of an impact-generated melt that chemically mixed upper mantle with crust, and 2) pre-existing troctolite and/or dunite plutons that were exposed, and have likely mechanically mixed with the anorthositic crust, during or post-impact. Complicating things further is the possibility that

troctolites *are the result of the former*, rather than magmatic processes [*Grieve et al.*, 1991; *Hess*, 1994; *Lucey*, 2010]. In either case we would expect these sites to have a wide distribution of olivine/plagioclase ratios, as we have found, and the detection of dunite would not favor either model.

4.5 Conclusions

Using mid-IR Diviner data we have placed constraints on olivine abundance within olivine-bearing regions detected by VNIR instruments. Of the 45 locations investigated, 12 are consistent with dunite assuming a rather high Fo#, while the rest have olivine/plagioclase ratios within the range of troctolite. Additionally, we applied FATT analysis to a selection of M^3 spectra. While the FATT results were not conclusive in all cases, we were able confirm the presence of fayalitic olivine in the walls and ejecta of a small crater in Nectaris that has an anomalously high CF position.

References

Adams, J. B., and T. B. McCord (1972), Electronic spectra of pyroxenes and interpretation of telescopic spectral reflectivity curves of the moon, paper presented at Lunar and Planetary Science Conference Proceedings.

Adams, J. B., and L. H. Goullaud (1978), Plagioclase feldspars-Visible and near infrared diffuse reflectance spectra as applied to remote sensing, paper presented at Lunar and Planetary Science Conference Proceedings.

Aronson, J. R., and A. G. Emslie (1973), Spectral Reflectance and Emittance of Particulate Materials. 2: Application and Results, *Appl. Opt.*, *12*(11), 2573-2584.

Bandfield, J. L., P. R. Christensen, and M. D. Smith (2000), Spectral data set factor analysis and end-member recovery: Application to analysis of Martian atmospheric particulates, *Journal of Geophysical Research: Planets*, *105*(E4), 9573-9587.

Cahill, J. T. S., P. G. Lucey, K. R. Stockstill-Cahill, and B. R. Hawke (2010), Radiative transfer modeling of near-infrared reflectance of lunar highland and mare soils, *Journal of Geophysical Research: Planets*, *115*(E12), E12013.

Che, C., and T. D. Glotch (2014), Thermal alteration: A possible reason for the inconsistency between OMEGA/CRISM and TES detections of phyllosilicates on Mars?, *Geophysical Research Letters*.

Conel, J. E. (1969), Infrared emissivities of silicates: Experimental results and a cloudy atmosphere model of Spectral emission from condensed particulate mediums, *Journal of Geophysical Research*, *74*(6), 1614-1634.

Denevi, B., P. Lucey, and S. Sherman (2008), Radiative transfer modeling of near-infrared spectra of lunar mare soils: Theory and measurement, *Journal of Geophysical Research: Planets (1991–2012)*, *113*(E2).

Donaldson Hanna, K., I. Thomas, B. Greenhagen, N. Bowles, and C. Pieters (2014), Characterization of Apollo Soil Samples Under Simulated Lunar Conditions, paper presented at Lunar and Planetary Institute Science Conference Abstracts.

Donaldson Hanna, K. L., M. B. Wyatt, I. R. Thomas, N. E. Bowles, B. T. Greenhagen, A. Maturilli, J. Helbert, and D. A. Paige (2012), Thermal infrared emissivity measurements under a

simulated lunar environment: Application to the Diviner Lunar Radiometer Experiment, *Journal of Geophysical Research: Planets*, *117*(E12), E00H05.

Dyar, M., E. Sklute, O. Menzies, P. Bland, D. Lindsley, T. Glotch, M. Lane, M. Schaefer, B. Wopenka, and R. Klima (2009), Spectroscopic characteristics of synthetic olivine: An integrated multi-wavelength and multi-technique approach, *American Mineralogist*, *94*(7), 883-898.

Elardo, S. M., D. S. Draper, and C. K. Shearer Jr (2011), Lunar Magma Ocean crystallization revisited: Bulk composition, early cumulate mineralogy, and the source regions of the highlands Mg-suite, *Geochimica et Cosmochimica Acta*, *75*(11), 3024-3045.

Friedlander, L., and T. Glotch (2014), Phyllosilicate Spectra Identified at Mawrth Vallis by Factor Analysis and Target Transformation are Consistent with Impact-Related Spectral Change, paper presented at Lunar and Planetary Institute Science Conference Abstracts.

Glotch, T. D., J. L. Bandfield, P. R. Christensen, W. M. Calvin, S. M. McLennan, B. C. Clark, A. D. Rogers, and S. W. Squyres (2006), Mineralogy of the light-toned outcrop at Meridiani Planum as seen by the Miniature Thermal Emission Spectrometer and implications for its formation, *Journal of Geophysical Research: Planets*, *111*(E12), E12S03.

Glotch, T. D., P. G. Lucey, J. L. Bandfield, B. T. Greenhagen, I. R. Thomas, R. C. Elphic, N. Bowles, M. B. Wyatt, C. C. Allen, and K. D. Hanna (2010a), Highly silicic compositions on the Moon, *Science*, *329*(5998), 1510-1513.

Glotch, T. D., et al. (2010b), Highly Silicic Compositions on the Moon, *Science*, *329*(5998), 1510-1513.

Goswami, J. N., and M. Annadurai (2008), Chandrayaan-1 mission to the Moon, *Acta Astronautica*, *63*(11), 1215-1220.

Greenhagen, B. T., P. Lucey, J. Bandfield, P. Hayne, J. Williams, and D. Paige (2011), The Diviner Lunar Radiometer compositional data products: Description and examples, paper presented at Lunar and Planetary Institute Science Conference Abstracts.

Greenhagen, B. T., et al. (2010), Global Silicate Mineralogy of the Moon from the Diviner Lunar Radiometer, *Science*, *329*(5998), 1507-1509.

Grieve, R. A. F., D. Stoffler, and A. Deutsch (1991), The Sudbury structure - controversial or misunderstood, *J. Geophys. Res.-Planets*, *96*(E5), 22753-22764.

Griffiths, R. W., and I. H. Campbell (1990), Stirring and structure in mantle starting plumes, *Earth and Planetary Science Letters*, *99*(1–2), 66-78.

Henderson, B. G., and B. M. Jakosky (1994), Near-surface thermal gradients and their effects on mid-infrared emission spectra of planetary surfaces, *Journal of Geophysical Research: Planets*, *99*(E9), 19063-19073.

Hess, P. C. (1994), Petrogenesis of lunar troctolites, *Journal of Geophysical Research: Planets*, *99*(E9), 19083-19093.

Hess, P. C. (1998), Source regions to lunar troctolite parent magmas, paper presented at Lunar and Planetary Institute Science Conference Abstracts.

Hess, P. C. (2000), Petrogenesis of lunar troctolites-Implications for the Moon and its evolution, paper presented at Lunar and Planetary Institute Science Conference Abstracts.

Isaacson, P. J., R. L. Klima, J. M. Sunshine, L. C. Cheek, C. M. Pieters, T. Hiroi, M. D. Dyar, M. Lane, and J. Bishop (2014), Visible to near-infrared optical properties of pure synthetic olivine across the olivine solid solution, *American Mineralogist*, *99*(2-3), 467-478.

Isaacson, P. J., et al. (2011), Remote compositional analysis of lunar olivine-rich lithologies with Moon Mineralogy Mapper (M3) spectra, *Journal of Geophysical Research: Planets*, *116*(E6), E00G11.

Klima, R. L., C. M. Pieters, and M. D. Dyar (2008), Characterization of the 1.2 μm M1 pyroxene band: Extracting cooling history from near-IR spectra of pyroxenes and pyroxene-dominated rocks, *Meteoritics & Planetary Science*, *43*(10), 1591-1604.

Kokhanovsky, A. A. (2006), *Light Scattering Reviews: Single and Multiple Light Scattering*, Springer.

Logan, L. M., G. R. Hunt, J. W. Salisbury, and S. R. Balsamo (1973), Compositional implications of Christiansen frequency maximums for infrared remote sensing applications, *Journal of Geophysical Research*, *78*(23), 4983-5003.

Longhi, J. (2003), A new view of lunar ferroan anorthosites: Postmagma ocean petrogenesis, *Journal of Geophysical Research: Planets*, *108*(E8), 5083.

Lucey, P. G. (2010), Planetary science: Mantle of the Moon exposed?, *Nature Geosci*, *3*(8), 517-518.

Lucey, P. G., D. T. Blewett, G. J. Taylor, and B. R. Hawke (2000), Imaging of lunar surface maturity, *Journal of Geophysical Research: Planets*, *105*(E8), 20377-20386.

Lucey, P. G., B. R. Hawke, C. M. Pieters, J. W. Head, and T. B. McCord (1986), A compositional study of the Aristarchus Region of the Moon using near-infrared reflectance spectroscopy, *Journal of Geophysical Research: Solid Earth*, *91*(B4), 344-354.

Lucey, P. G., D. Paige, B. Greenhagen, J. Bandfield, and T. Glotch (2010), Comparison of Diviner Christiansen Feature position and visible albedo: Composition and space weathering implications, paper presented at Lunar and Planetary Institute Science Conference Abstracts.

Lucey, P. G., et al. (2006), Understanding the Lunar Surface and Space-Moon Interactions, *Reviews in Mineralogy and Geochemistry*, *60*(1), 83-219.

Lyon, R. J. P. (1965), Analysis of rocks by spectral infrared emission (8 to 25 microns), *Economic Geology*, *60*(4), 715-736.

Malinowski, E. R. (1991), Factor analysis in chemistry.

Mustard, J. F., et al. (2011), Compositional diversity and geologic insights of the Aristarchus crater from Moon Mineralogy Mapper data, *Journal of Geophysical Research: Planets*, *116*(E6), E00G12.

Nash, D. B., J. W. Salisbury, J. E. Conel, P. G. Lucey, and P. R. Christensen (1993), Evaluation of infrared emission spectroscopy for mapping the moon's surface composition from lunar orbit, *Journal of Geophysical Research: Planets*, *98*(E12), 23535-23552.

Ohtake, M., et al. (2009), The global distribution of pure anorthosite on the Moon, *Nature*, *461*(7261), 236-240.

Pieters, C. M. (1982), Copernicus Crater Central Peak: Lunar Mountain of Unique Composition, *Science*, *215*(4528), 59-61.

Pieters, C. M. (1996), Plagioclase and maskelynite diagnostic features, paper presented at Lunar and Planetary Institute Science Conference Abstracts.

Pieters, C. M., et al. (2009), The Moon Mineralogy Mapper (M3) on Chandrayaan-1, *Current Science (00113891)*, *96*(4), 500-505.

Powell, K., P. McGovern, and G. Kramer (2012), Olivine Detections at the Rim of Crisium Basin with Moon Mineralogy Mapper, paper presented at Lunar and Planetary Institute Science Conference Abstracts.

Ruff, S. W., and P. R. Christensen (2002), Bright and dark regions on Mars: Particle size and mineralogical characteristics based on Thermal Emission Spectrometer data, *Journal of Geophysical Research: Planets*, *107*(E12), 5119.

Ruff, S. W., P. R. Christensen, P. W. Barbera, and D. L. Anderson (1997), Quantitative thermal emission spectroscopy of minerals: A laboratory technique for measurement and calibration, *Journal of Geophysical Research: Solid Earth (1978–2012)*, *102*(B7), 14899-14913.

Ryder, G. (1991), Lunar ferroan anorthosites and mare basalt sources - the mixed connection, *Geophysical Research Letters*, *18*(11), 2065-2068.

Ryder, G., M. D. Norman, and G. Jeffrey Taylor (1997), The complex stratigraphy of the highland crust in the Serenitatis region of the Moon inferred from mineral fragment chemistry, *Geochimica et Cosmochimica Acta*, *61*(5), 1083-1105.

Salisbury, J. W., and L. S. Walter (1989), Thermal infrared (2.5–13.5 μm) spectroscopic remote sensing of igneous rock types on particulate planetary surfaces, *Journal of Geophysical Research: Solid Earth*, *94*(B7), 9192-9202.

Salisbury, J. W., and A. Wald (1992), The role of volume scattering in reducing spectral contrast of reststrahlen bands in spectra of powdered minerals, *Icarus*, *96*(1), 121-128.

Salisbury, J. W., B. Hapke, and J. W. Eastes (1987), Usefulness of weak bands in midinfrared remote sensing of particulate planetary surfaces, *Journal of Geophysical Research: Solid Earth (1978–2012)*, *92*(B1), 702-710.

Salisbury, J. W., A. Wald, and D. M. D'Aria (1994), Thermal-infrared remote sensing and Kirchhoff's law: 1. Laboratory measurements, *Journal of Geophysical Research: Solid Earth (1978–2012)*, *99*(B6), 11897-11911.

Salisbury, J. W., A. Basu, and E. M. Fischer (1997), Thermal Infrared Spectra of Lunar Soils, *Icarus*, *130*(1), 125-139.

Shearer, C. K., and J. Papike (2005), Early crustal building processes on the moon: Models for the petrogenesis of the magnesian suite, *Geochimica et Cosmochimica Acta*, *69*(13), 3445-3461.

Stewart, S. (2011), Impact basin formation: The mantle excavation paradox resolved, paper presented at Lunar and Planetary Institute Science Conference Abstracts.

Sunshine, J. M., and C. M. Pieters (1998), Determining the composition of olivine from reflectance spectroscopy, *Journal of Geophysical Research: Planets*, *103*(E6), 13675-13688.

Sunshine, J. M., C. M. Pieters, and S. F. Pratt (1990), Deconvolution of mineral absorption bands: An improved approach, *Journal of Geophysical Research: Solid Earth*, *95*(B5), 6955-6966.

Thomas, I., N. Bowles, B. Greenhagen, T. Glotch, K. Donaldson Hanna, M. Wyatt, J. Bandfield, and D. Paige (2010), Emission measurements of lunar analogues for interpretation of returning data from the Diviner Lunar Radiometer on NASA's Lunar Reconnaissance Orbiter, paper presented at Lunar and Planetary Institute Science Conference Abstracts.

Thomas, N., and J. Bandfield (2013), Identification of Spectral Endmembers in CRISM Data Using Factor Analysis and Target Transformation, paper presented at Lunar and Planetary Institute Science Conference Abstracts.

Tompkins, S., and C. M. Pieters (1999), Mineralogy of the lunar crust: Results from Clementine, *Meteoritics & Planetary Science*, *34*(1), 25-41.

Wieczorek, M., B. Jolliff, A. Khan, M. Pritchard, B. Weiss, J. Williams, L. Hood, K. Righter, C. Neal, and C. Shearer (2006), New views of the moon, *Rev. Min. Geochem*, *60*, 221-364.

Yamamoto, S., et al. (2010), Possible mantle origin of olivine around lunar impact basins detected by SELENE, *Nature Geosci*, *3*(8), 533-536.

Yamamoto, S., et al. (2012), Olivine-rich exposures in the South Pole-Aitken Basin, *Icarus*, *218*(1), 331-344.

Tables and Figures

Table 4.1: Mixtures measured in lunar environment emissivity chamber

Plagioclase wt%	**0**	**12.6**	**25**	**50**	**75**	**87.4**	**100**
Forsterite	X	X	X	X	X	X	X
Augite	X			X	X		X

Table4.2 RMS values of fits for FATT-derived end-members to library spectra of synthetic olivines.

library spectrum	**B3 Crisium: Pr. Agarum**	**C6 Imbrium: Aristarcus**	**C3 Imbrium: Eratosthenes**	**D1 Humorum: small crater**	**G1 Nectaris: small crater**
Fo0	0.015	0.011	0.016	0.047	0.008
Fo10	0.018	0.012	0.019	0.060	0.009
Fo20	0.021	0.016	0.023	0.071	0.012
Fo30	0.013	0.008	0.014	0.050	0.007
Fo40	0.011	0.005	0.014	0.036	0.005
Fo50	0.006	0.004	0.009	0.020	0.005
Fo55	0.011	0.005	0.014	0.034	0.005
Fo60	0.016	0.008	0.017	0.056	0.017
Fo65	0.009	0.007	0.011	0.033	0.005
Fo70	0.010	0.006	0.014	0.027	0.007
Fo75	0.008	0.006	0.012	0.021	0.006
Fo80	0.011	0.010	0.015	0.026	0.009
Fo89.5	0.007	0.007	0.010	0.012	0.007
Fo100	0.002	0.002	0.002	0.003	0.002

Table 4.3

Information for areas examined in this study including: location, M^3 image number CF and OMAT values, and olivine abundance estimates. Standard CF values are before latitude/time of day correction.

Location	M3 Image number	Description/notes	Lat	Lon	Standard CF position	σ CF	Corrected CF position	σ CF	ppd	Npts averaged	MI-OMAT	σ MI-OMAT	Clementine-OMAT	CF + OMAT - 0.4	% olivine based on 2-component system
A: Mare Moscoviense															
A2	**M3G20090528T130108**	**S crater ejecta**	**28.10**	**145.30**	**8.51**	**0.12**	**8.42**	**0.06**	**256**	**42**	**0.1719**	**0.0332**	**--**	**8.1869**	**71**
A3	**M3G20090528T083319**	**v. small crater N wall?**	**21.20**	**147.55**	**8.34**	**0.12**	**8.35**	**0.04**	**256**	**20**	**0.1382**	**0.0203**	**--**	**8.0882**	**57**
A3	**M3G20090528T083319**	**S wall small crater**	**21.35**	**147.16**	**8.60**	**0.07**	**8.32**	**0.02**	**128**	**10**	**--**	**--**	**0.1702**	**8.0894**	**58**
A3	**M3G20090528T083319**	**NE wall small crater**	**21.07**	**147.36**	**8.32**	**0.01**	**8.42**	**0.05**	**128**	**10**	**--**	**--**	**0.1845**	**8.2016**	**73**
A4	**M3G20081229T022350**	**W crater wall ejecta**	**22.86**	**148.94**	**8.50**	**0.12**	**8.34**	**0.03**	**256**	**42**	**0.1182**	**0.0102**	**--**	**8.0582**	**52**
A5	**M3G20090528T083319**	**SW crater wall?**	**21.79**	**147.40**	**8.16**	**0.03**	**8.19**	**0.03**	**256**	**42**	**0.1644**	**0.0101**	**--**	**7.9544**	**21**
A6	**M3G20081229T022350**	**S crater wall**	**21.64**	**148.15**	**8.14**	**0.08**	**8.27**	**0.03**	**256**	**22**	**0.1471**	**0.0135**	**--**	**8.0171**	**42**
A7	**M3G20081229T180950**	**W crater wall**	**23.01**	**139.77**	**8.21**	**0.04**	**8.15**	**0.02**	**256**	**270**	**0.1609**	**0.0107**	**--**	**7.9109**	**12**
B: Mare Crisium															
B1	**M3G20090105T134845**	**Glaiser crater wall**	**13.24**	**49.14**	**8.24**	**0.06**	**8.22**	**0.06**	**256**	**440**	**0.1741**	**0.0178**		**7.9941**	**35**
B1	**M3G20090105T134845**	**WSW wall Glaisher crater**	**13.23**	**49.19**	**8.36**	**0.01**	**8.29**	**0.04**	**128**	**12**	**--**	**--**	**0.2093**	**8.1042**	**60**
B1	**M3G20090105T134845**	**N of Glaisher crater**	**13.66**	**49.19**	**8.33**	**0.02**	**8.14**	**0.02**	**128**	**8**	**--**	**--**	**0.2080**	**7.9482**	**20**
B1	**M3G20090105T134845**	**SE wall Glaisher crater**	**13.01**	**49.52**	**8.24**	**0.02**	**8.13**	**0.03**	**128**	**12**	**--**	**--**	**0.2190**	**7.9450**	**19**
B2	**M3G20090131T151551**	**SW crater ejecta**	**12.03**	**65.55**	**8.41**	**0.02**	**8.27**	**0.02**	**256**	**51**	**0.1393**	**0.0073**		**8.0093**	**40**
B3	**M3G20090104T062425**	**Pr. Agarum**	**14.25**	**66.15**	**8.40**	**0.10**	**8.35**	**0.07**	**256**	**105**	**0.1374**	**0.0116**	**--**	**8.0874**	**57**
B4	**M3T20090104T220845**	**NE crater ejecta?**	**8.42**	**58.69**	**8.43**	**0.03**	**8.33**	**0.04**	**256**	**55**	**0.1405**	**0.0122**	**--**	**8.0705**	**55**
B4	**M3T20090701T140225**	**nearby NW**	**8.85**	**59.13**	**8.50**	**0.06**	**8.37**	**0.03**	**256**	**196**	**0.1195**	**0.0415**	**--**	**8.0895**	**58**

		crater ejecta													
B5	M3G20090201T125453	NW crater wall (nothing obvious in M3)	24.11	54.20	8.10	0.01	8.20	0.01	256	31	0.1370	0.0056	--	7.9370	17
B5	M3G20090201T125453	SW crater wall	24.02	54.18	8.10	0.02	8.20	0.02	256	82	0.1336	0.0091	--	7.9336	16
B6	M3G20090201T165935	SW crater wall (noisy in M3)	11.95	52.41	8.94	0.58	8.43	0.40	256	215	0.1447	0.0097	--	8.1747	69
B7	M3G20090729T104424	v. small spot SE crater wall	18.81	49.63	8.16	0.05	8.22	0.04	256	54	0.1355	0.0041	--	7.9555	23
C: Mare Imbrium															
C1	M3G20090416T122951	Copernicus central peak	9.63	339.96	8.35	0.20	8.23	0.18	256	41	0.2235	0.0152		8.0535	51
C1	M3G20090416T122951	N wall Copernicus	10.96	339.97	8.37	0.03	8.25	0.02	128	12	--	--	0.2338	8.0865	57
C1	M3G20090416T122951	central peak Copernicus main	9.68	339.93	8.30	0.05	8.10	0.03	128	8	--	--	0.2795	7.9762	29
C1	M3G20090416T122951	central peak Copernicus small	9.65	340.00	8.26	0.02	8.14	0.02	128	12	--	--	0.2434	7.9878	33
C2	M3G20090608T125102	N-facing SP target	44.94	359.19	8.07	0.03	8.24	0.03	128	12	--	--	0.2274	8.0641	53
C2	M3G20090608T125102	S-facing M3 olv spot	44.85	359.18	8.20	0.01	8.20	0.02	128	8	--	--	0.2568	8.0519	51
C3	M3G20090609T101951	Eratosthenes crater central peak	14.63	348.88	8.56	0.24	8.44	0.10	256	42	0.1713	0.0106	--	8.2113	75
C4/5	M3G20090208T021836	crater wall?	48.20	329.20	8.26	0.21	8.22	0.02	256	42	0.1461	0.0084	--	7.9661	26
C6	M3G20090612T060502	Aristarchus crater rim	23.35	313.02	8.27	0.14	8.24	0.05	256	313	0.2967	0.0402	--	8.1367	64
D: Mare Humorum															
D1	M3G20090612T060502	W crater wall	-19.25	312.73	8.33	0.05	8.27	0.03	256	340	0.1722	0.0198	--	8.0422	49
D1	M3G20090209T054031	W crater wall	-19.30	312.78	8.34	0.03	8.34	0.03	128	15		--	0.2250	8.1649	68
G: Mare Nectaris															
G1	M3G20090107T011405	crater wall in mare	-14.45	30.07	8.58	0.20	8.48	0.10	256	171	0.2073	0.0301	--	8.2873	87
G2	M3G20090203T160452	central peak theophilus	-11.25	26.38	8.17	0.09	8.12	0.04	256	592	0.2309	0.0266	--	7.9509	21
H: Mare Serenitatis															

H1	**M3G20090108T044645**	**crater wall E**	**16.29**	**16.22**	**8.19**	**0.01**	**8.18**	**0.01**	**128**	**20**		**--**	**0.2131**	**7.9903**	**34**
I: Mare Humboldtianum															
I1	**M3G20090531T215442**	**Compton crater rim/wall S (unclear in M3, possibly CF artifact orbit 10514))**	**53.35**	**103.50**	**8.22**	**0.09**	**8.16**	**0.03**	**128**	**18**		**--**	**0.2492**	**8.0120**	**41**
J: Mare Australe															
J1	**M3G20090601T062753**	**small crater S wall/floor**	**-33.33**	**97.15**	**8.29**	**0.02**	**8.23**	**0.02**	**128**	**12**		**--**	**0.2284**	**8.0591**	**52**
J1	**M3G20090601T062753**	**small crater S rim**	**-33.54**	**97.25**	**8.36**	**0.03**	**8.25**	**0.01**	**128**	**12**		**--**	**0.1922**	**8.0394**	**48**
J1	**M3G20090601T062753**	**small crater S rim**	**-33.56**	**97.15**	**8.35**	**0.02**	**8.22**	**0.01**	**128**	**21**		**--**	**0.1965**	**8.0160**	**42**
J2	**M3G20090602T074711**	**Humboldt crater floor Small crater wall N (no SP)**	**-27.09**	**83.13**	**8.15**	**0.02**	**8.21**	**0.02**	**128**	**12**		**--**	**0.2335**	**8.0438**	**49**
J2	**M3G20090602T074711**	**Small crater rim S (SP)**	**-26.89**	**83.12**	**8.15**	**0.01**	**8.17**	**0.01**	**128**	**12**		**--**	**0.1958**	**7.9664**	**26**
K: Western side of Oceanus Procellarum															
K1	**M3G20090210T051732**	**Mare, SP spot N**	**33.99**	**300.82**	**8.40**	**0.03**	**8.26**	**0.01**	**128**	**15**		**--**	**0.2055**	**8.0658**	**54**
K1	**M3G20090210T051732**	**Mare, SP?**	**33.82**	**300.90**	**8.42**	**0.02**	**8.34**	**0.01**	**128**	**20**		**--**	**0.2021**	**8.1459**	**66**
L: Geminus															
L1	**M3G20090201T085853**	**crater wall N**	**35.40**	**56.57**	**8.51**	**0.46**	**8.22**	**0.05**	**128**	**30**		**--**	**0.2077**	**8.0278**	**45**
L1	**M3G20090201T085853**	**crater wall N**	**35.42**	**56.55**	**8.29**	**0.03**	**8.22**	**0.02**	**128**	**15**		**--**	**0.2117**	**8.0288**	**46**
L1	**M3G20090201T085853**	**crater wall N (M3 only)**	**35.42**	**56.83**	**8.21**	**0.01**	**8.28**	**0.01**	**128**	**12**		**--**	**0.2382**	**8.1143**	**61**

Figure 4.1

Example for area of interest in Mare Crisium, where red boxes indicate the area of data extraction. Left top: Diviner CF map. Left bottom: Diviner emissivity data. Right top: M^3 index map where red=1 μm band depth, green=2 μm band depth and blue=1578 nm reflectance. Right Bottom: M^3 raw reflectance spectrum and continuum removed reflectance spectrum.

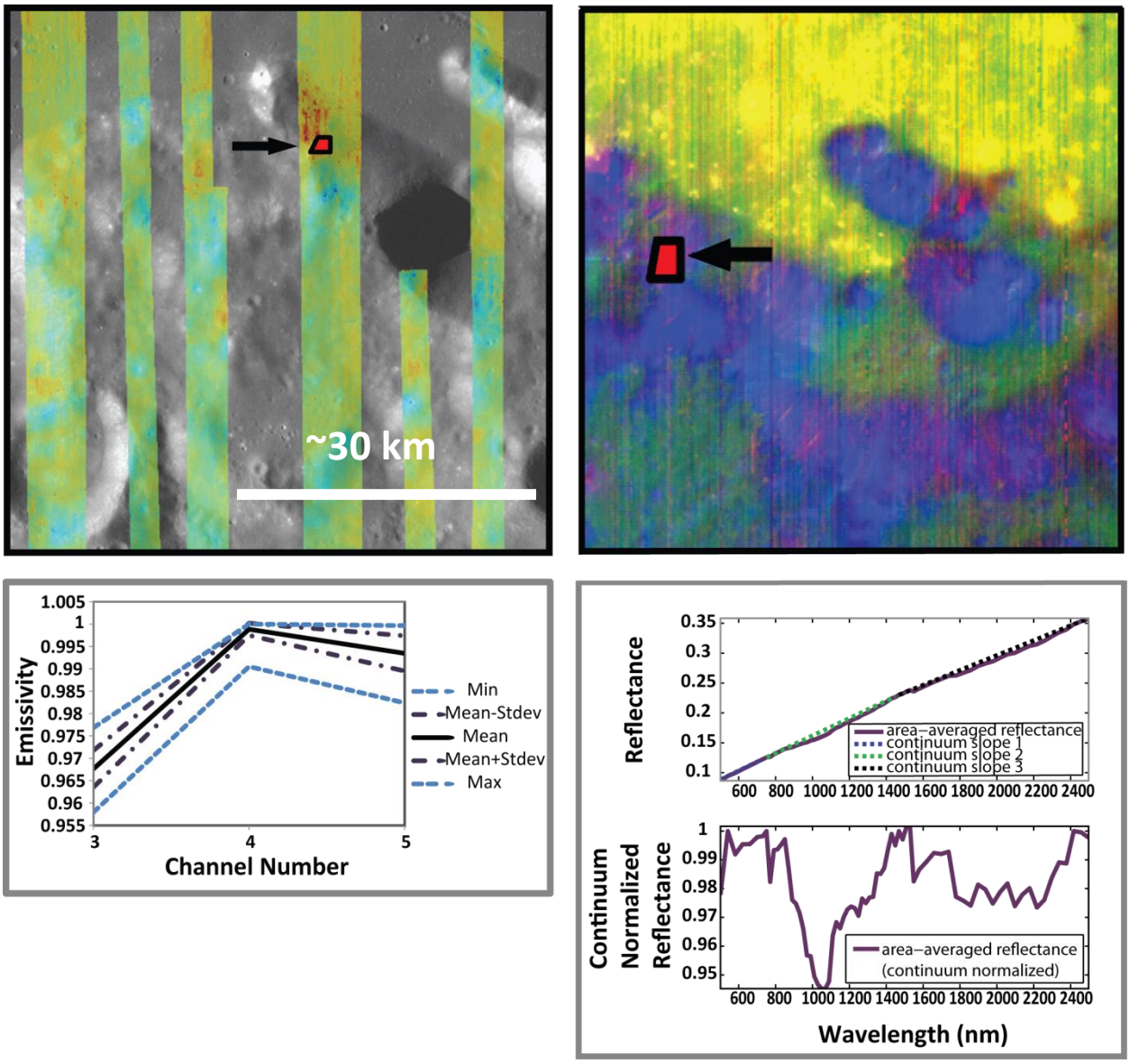

Figure 4.2

Emissivity data and calculated Diviner CF values for plagioclase-forsterite mixtures. (A) Full resolution lunar environment emissivity data. (B) Full resolution ambient environment emissivity data. (C) Lunar environment emissivity data convolved to Diviner channels 3-7. (D) Calculated Diviner CF values for both ambient and lunar environment data, along with the expected values resulting from linear mixing of the end-members.

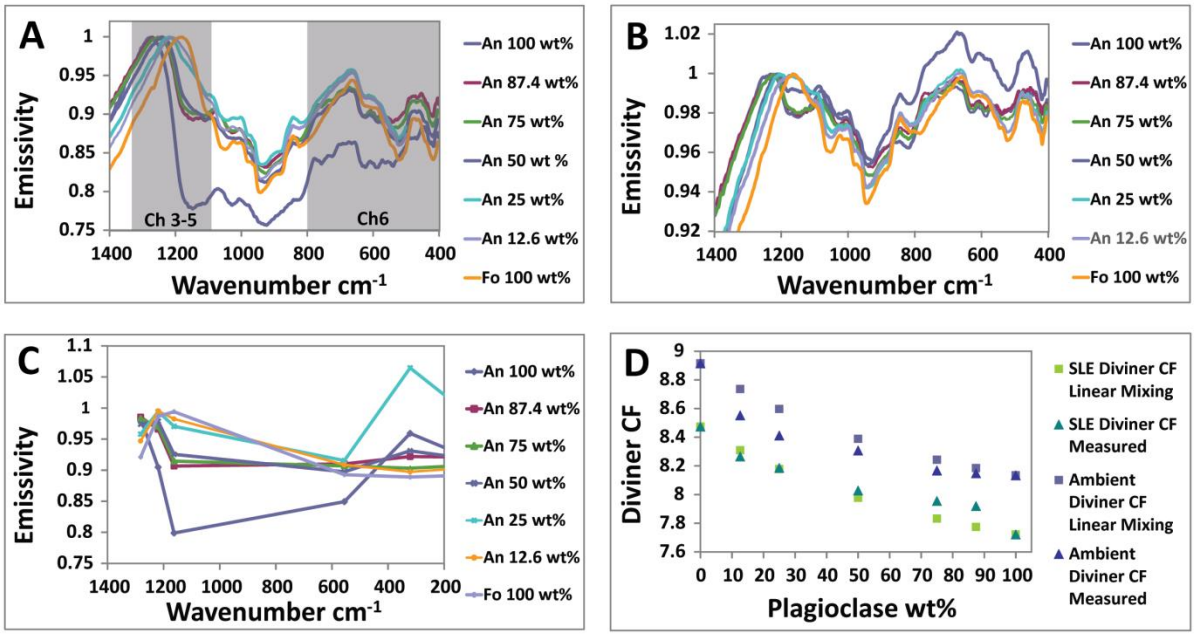

Figure 4.3

Histograms of (A) olivine abundance estimates and (B) CF values of the areas examined in this study. Three sets of abundance estimates are given based on (blue) CF values prior to optical maturity correction (red) CF values after optical maturity correction, and (green) CF values of a hypothetical olivine end-member with a CF of 9 μm.

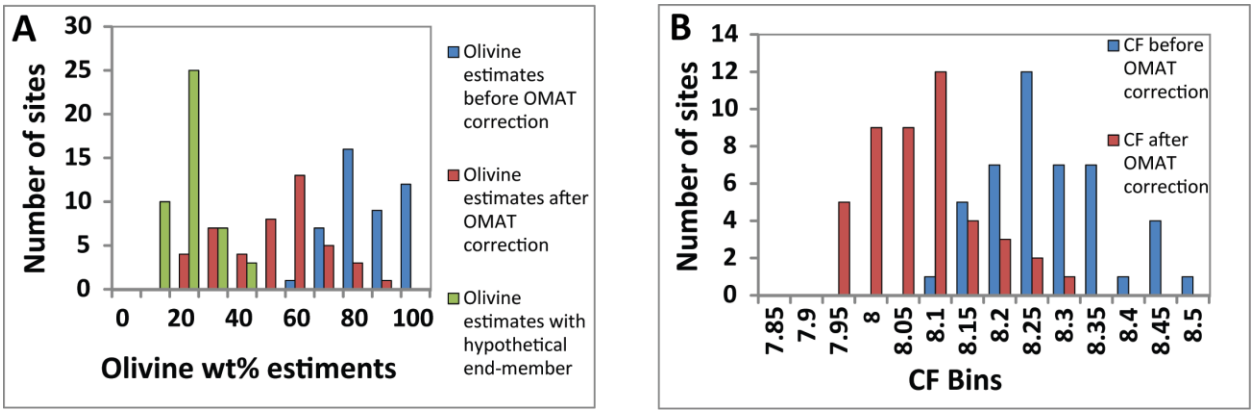

Figure 4.4

Figures explaining Ch 456 concavity index. (A) lunar environment emissivity spectra of plagioclase-forsterite mixtures convolved to Diviner channels, showing the change in concavity of Ch 456 with mixture composition. (B) lunar environment emissivity spectra for selected plagioclase-forsterite and plagioclase-augite mixtures convolved to Diviner channels 4-6.

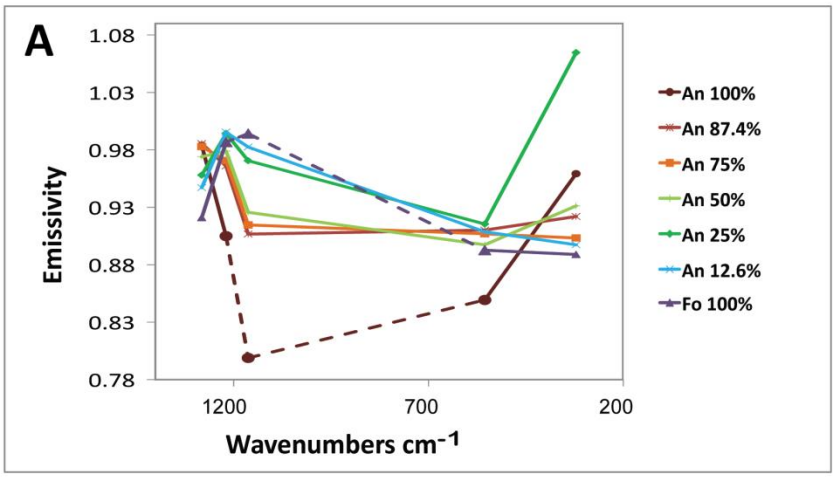

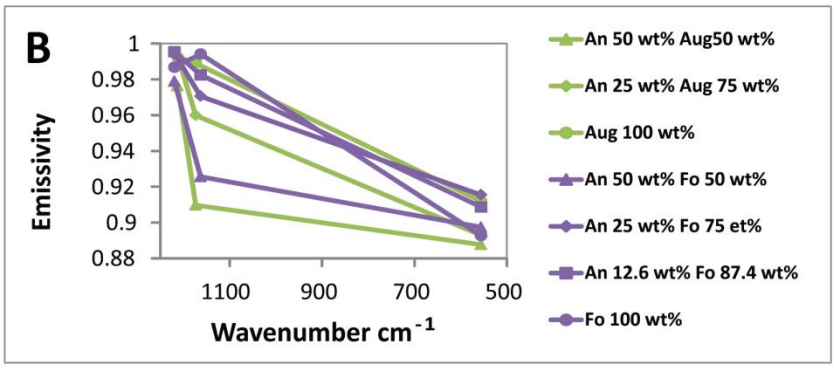

Figure 4.5

Comparison of CF with Ch456 concavity at Aristarchus crater. Left: Diviner CF map scaled 7.8μm(blue) to 8.55μm(red). Right: Ch 456 concavity index scaled -0.01(blue) to 0.005(red).

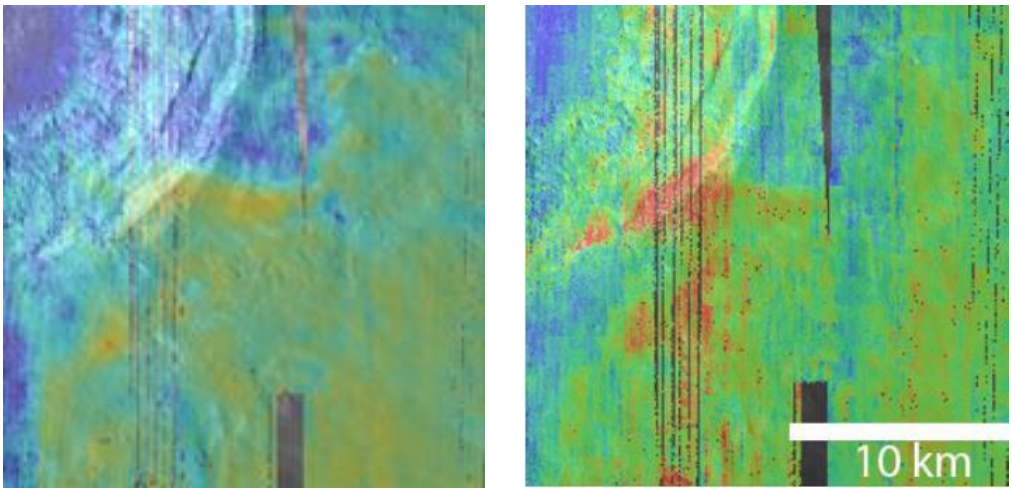

Figure 4.6

Plot of Ch 456 concavity index vs. CF for the southwest rim of Aristarchus crater. The CF values have had the incidence angle, but not the OMAT correction applied.

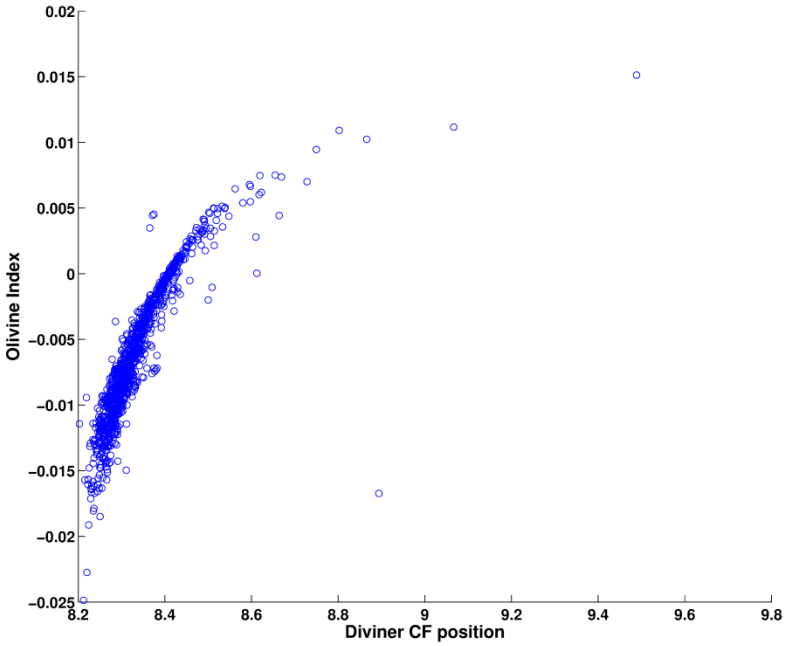

Figure 4.A1

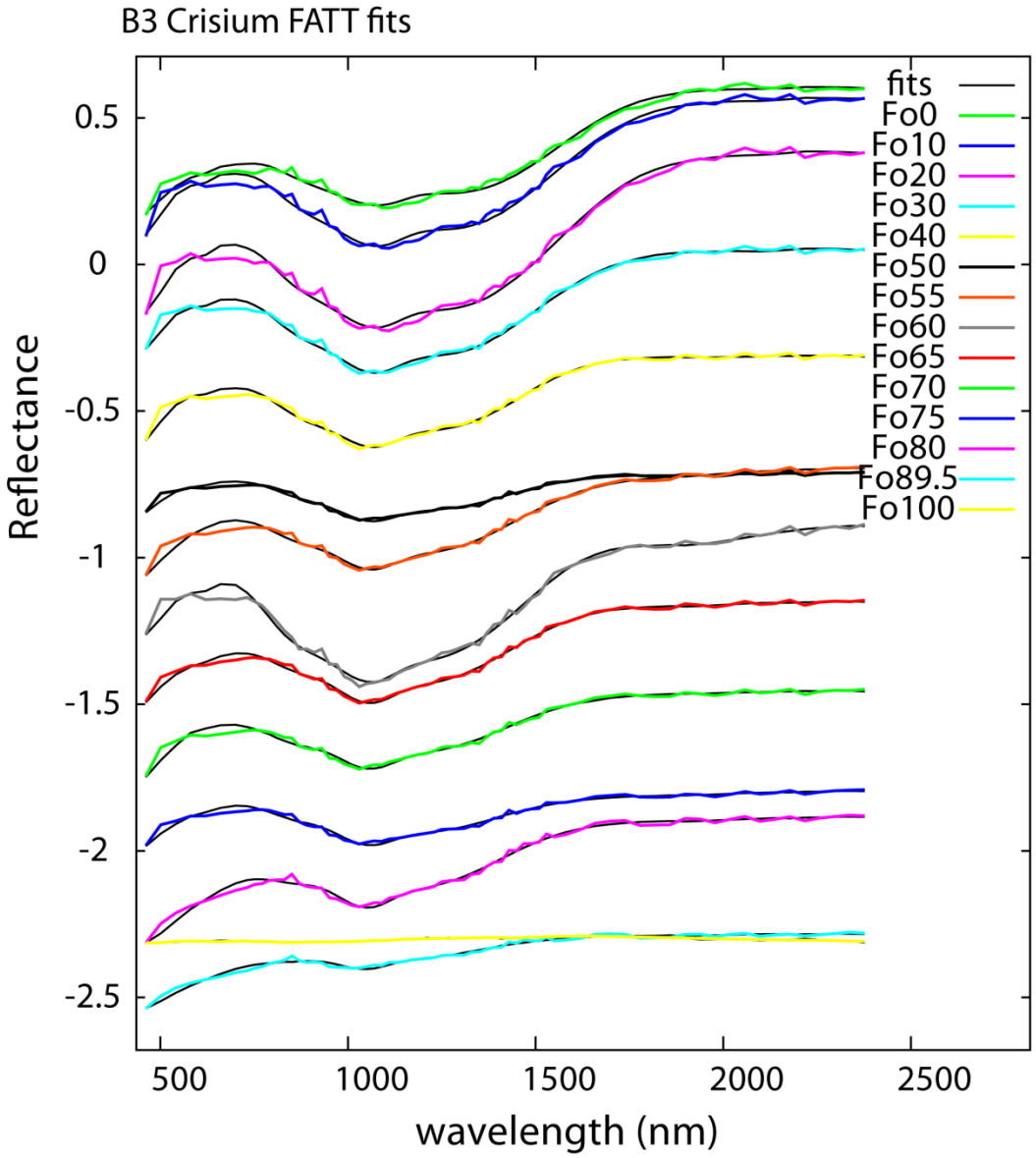
B3 Crisium FATT fits
Reflectance
wavelength (nm)
0.5
0
-0.5
-1
-1.5
-2
-2.5
500
1000
1500
2000
2500
fits
Fo0
Fo10
Fo20
Fo30
Fo40
Fo50
Fo55
Fo60
Fo65
Fo70
Fo75
Fo80
Fo89.5
Fo100

Figure 4.A2

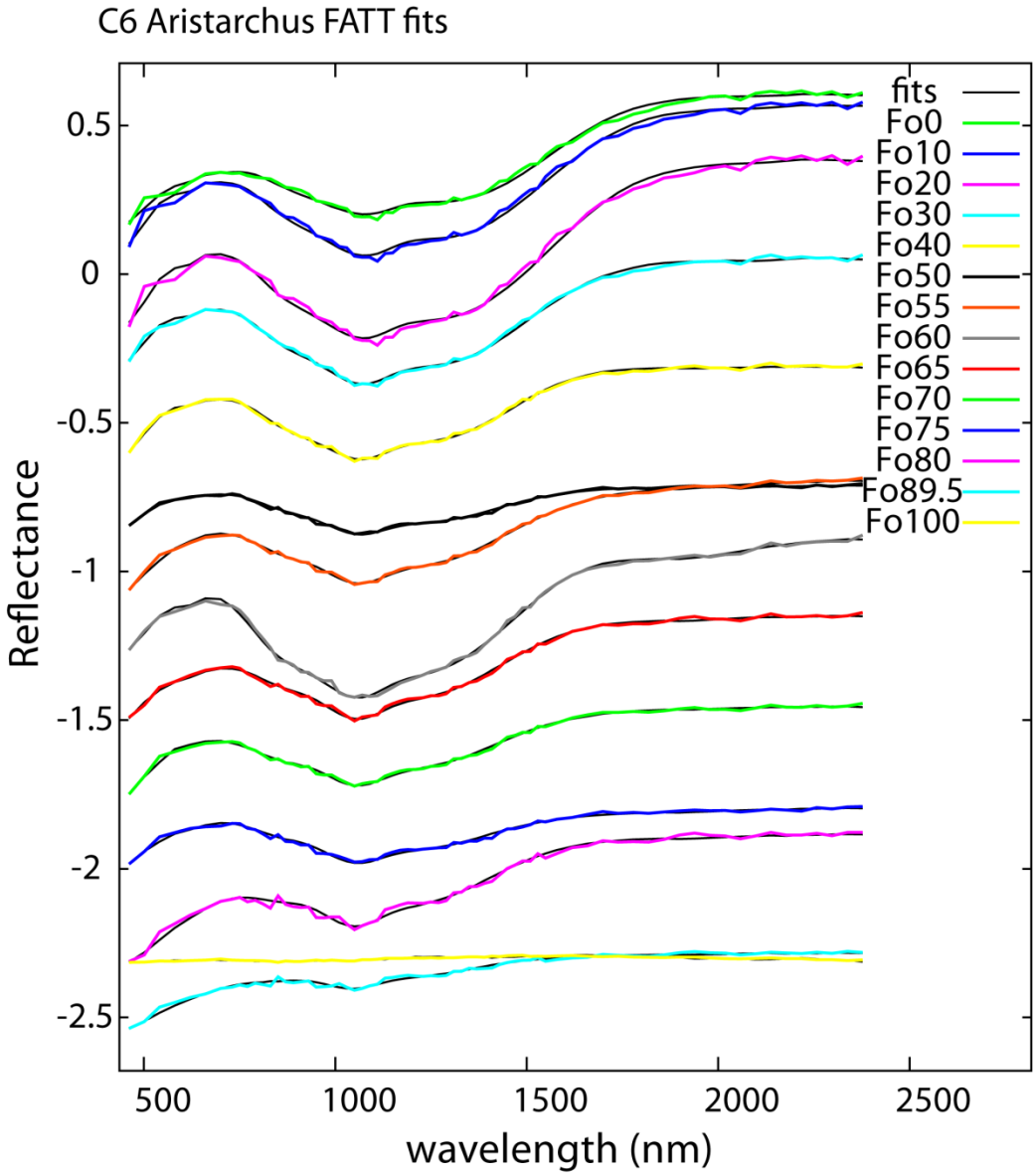
C6 Aristarchus FATT fits
fits
Fo0
Fo10
Fo20
Fo30
Fo40
Fo50
Fo55
Fo60
Fo65
Fo70
Fo75
Fo80
Fo89.5
Fo100
Reflectance
0.5
0
-0.5
-1
-1.5
-2
-2.5
500
1000
1500
2000
2500
wavelength (nm)

Figure 4.A3

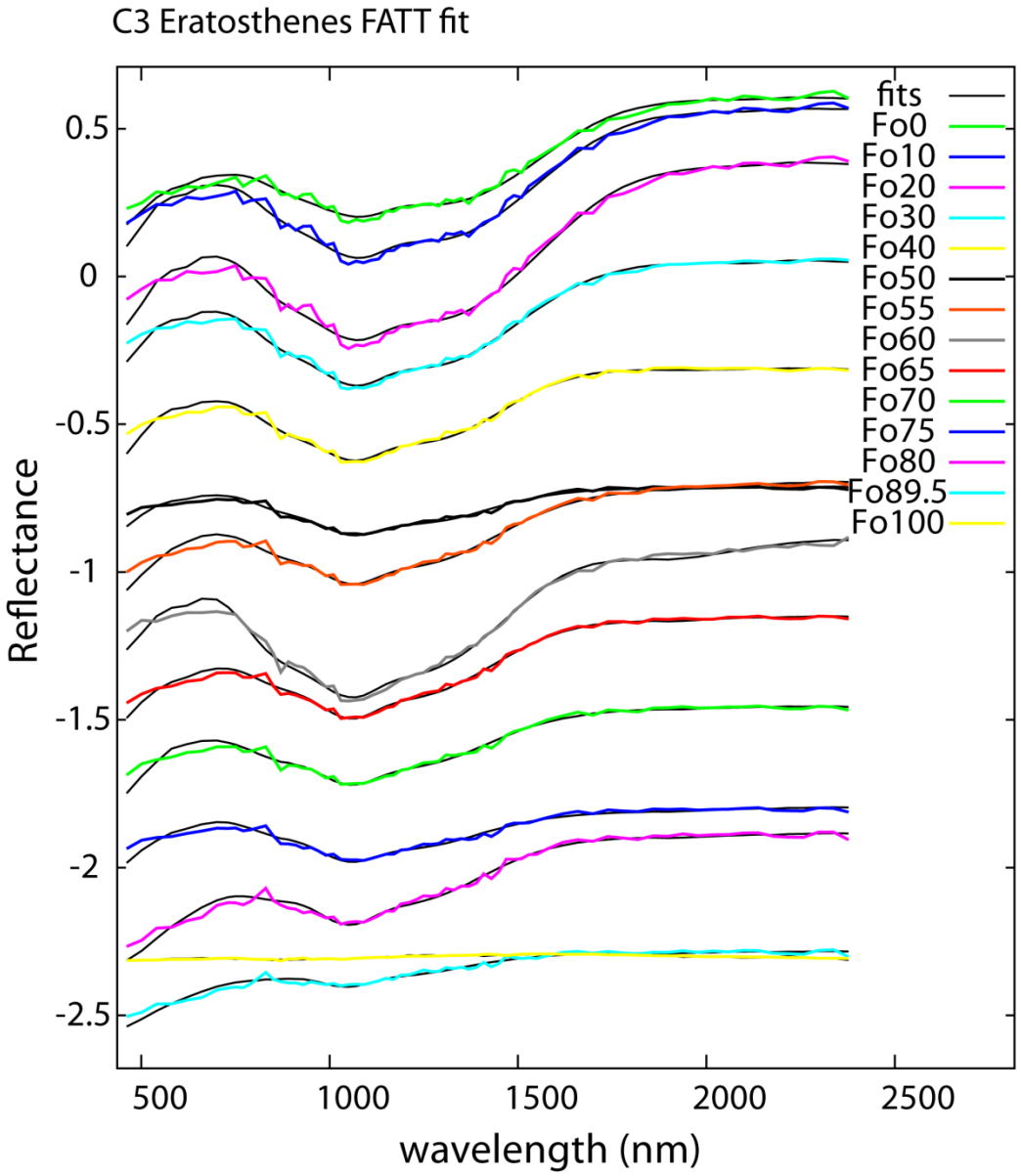
C3 Eratosthenes FATT fit
fits
Fo0
Fo10
Fo20
Fo30
Fo40
Fo50
Fo55
Fo60
Fo65
Fo70
Fo75
Fo80
Fo89.5
Fo100
Reflectance
0.5
0
-0.5
-1
-1.5
-2
-2.5
500
1000
1500
2000
2500
wavelength (nm)

Figure 4.A4

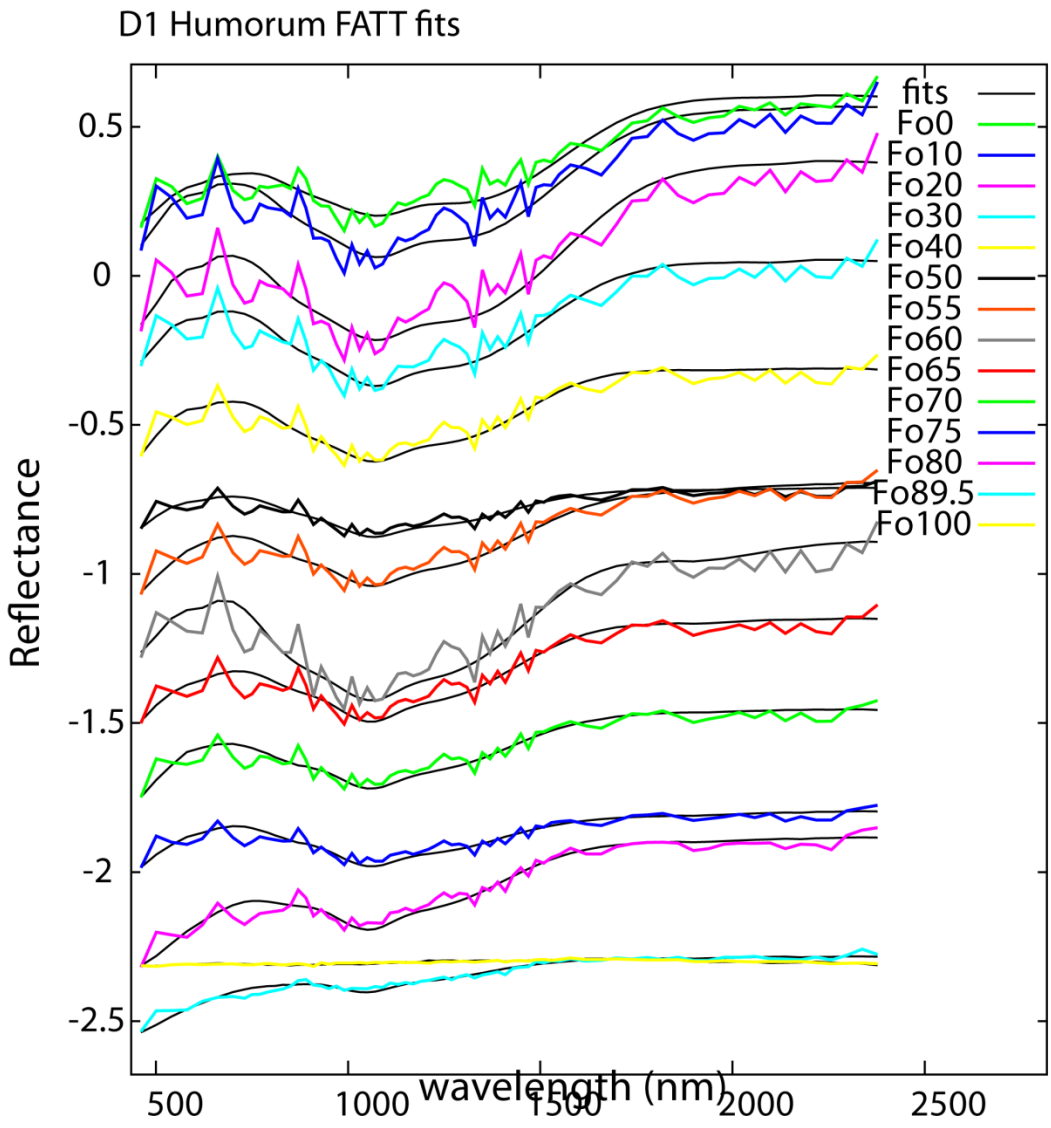
D1 Humorum FATT fits
fits
Fo0
Fo10
Fo20
Fo30
Fo40
Fo50
Fo55
Fo60
Fo65
Fo70
Fo75
Fo80
Fo89.5
Fo100
Reflectance
0.5
0
-0.5
-1
-1.5
-2
-2.5
500
1000
1500
2000
2500
wavelength (nm)

Figure 4.A5

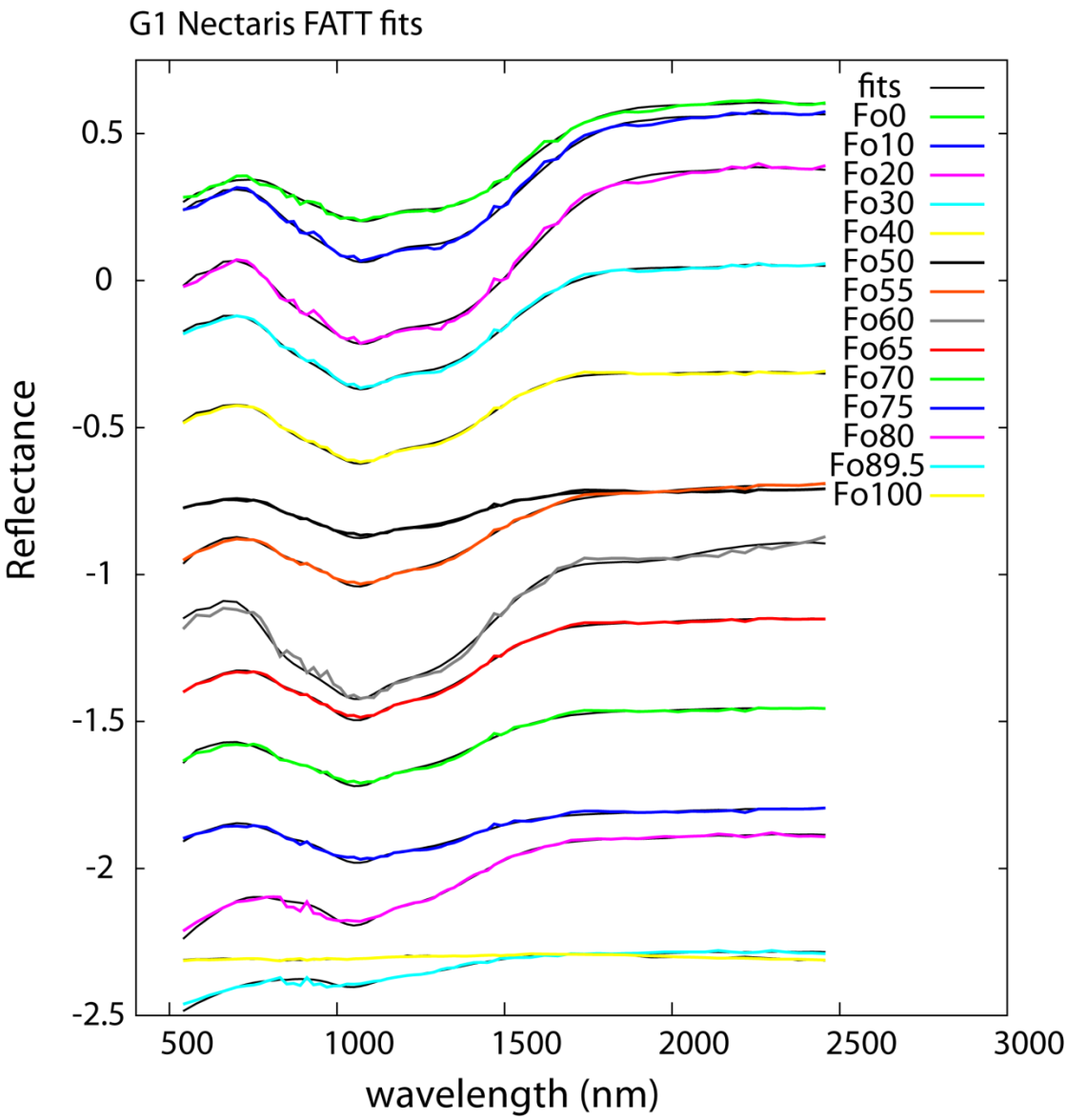
G1 Nectaris FATT fits
fits
Fo0
Fo10
Fo20
Fo30
Fo40
Fo50
Fo55
Fo60
Fo65
Fo70
Fo75
Fo80
Fo89.5
Fo100
Reflectance
0.5
0
-0.5
-1
-1.5
-2
-2.5
500
1000
1500
2000
2500
3000
wavelength (nm)

Chapter 5: summary and future directions

First, I showed that replacing Mie scattering with the T-matrix method in hybrid RT models improves the match between modeled and measured mid-IR spectra. However, the smallest particle size was still not well modeled at long wavelengths. One way to approach this would be to test whether a less dense, but larger total particle cluster gives better results. Additionally, the T-matrix method can be used to compare scattering properties of spherical versus non-spherically shaped particles of the same refractive index. The newest version of the MSTM code allows for the investigation of internal scatters by allowing the spheres to be embedded in other spheres.

Another possibility is to explore different RT formulations. In particular, I am interested in trying the DISORT (Discrete ordinates radiative transfer transfer) program. DISORT uses a multi-stream method where the user can input the number of streams used in computation and also the number of angles at which they would like calculated intensites [*Stamnes et al.*, 2000].

Then, I outlined the process for deriving mid-IR optical constants of monoclinic crystals. I then give sets of optical constants for four clinopyroxene compositions that had not previously been measured. I would like to begin working on a similar method for triclinic materials. Triclinic optical constants have been measured by *Höfer et al.* [2014] for $K_2Cr_2O_7$ from reflectance spectra taken at near-normal incidence. Additionally, there is much work to be done before oriented optical constants can be applied to surfaces made up of randomly oriented particulates. *Mayerhöfer and Popp* [2007] describe a method to verify optical constants derived from dispersion theory against measured reflectance spectra of both course and fine particulates. They found that of the two different sets of CuO optical constants tested, only one could be

validated. This type of validation method would be useful for choosing sets of optical constants to apply to remote sensing data.

Lastly, I compared Diviner remote sensing data with laboratory emissivity spectra of plagioclase-olivine mixtures taken under lunar-like conditions to investigate olivine-bearing regions of the moon. Mixing between components was found to be non-linear and mixing behavior differed between ambient and vacuum pressures. These results highlight the need for emissivity models that are applicable to fine-grained surfaces.

References

Stamnes, K. et al. (2000) DISORT, a general-purpose Fortran program for discrete-ordinate-method radiative transfer in scattering and emitting layered media: documentation of methodology. Goddard Space Flight Center, NASA .

Hofer, S., J. Popp, T.G. Mayerhofer (2014) Dispersion analysis of triclinic $K_2Cr_2O_7$. Vibrational Spectroscopy, 72, 111-118.

Mayerhofer and Popp (2007) Employing spectra of polycrystalline materials for the verification of optical constants obtained from corresponding low-symmetry single crystals. Applied Optics, 46, 3, 327-334.

Biboliography

Adams, J. B., and L. H. Goullaud (1978), Plagioclase feldspars-Visible and near infrared diffuse reflectance spectra as applied to remote sensing, paper presented at Lunar and Planetary Science Conference Proceedings.

Adams, J. B., and T. B. McCord (1972), Electronic spectra of pyroxenes and interpretation of telescopic spectral reflectivity curves of the moon, paper presented at Lunar and Planetary Science Conference Proceedings.

Allen, C.C., Greenhagen, B.T., Donaldson Hanna, K.L. and Paige, D.A. (2011), Analysis of lunar pyroclastic deposit FeO abundances by LRO Diviner, *Journal of Geophysical Research: Planets*, *117*(E12).

Arnold, J.A., Glotch, T.D., Greenhagen, B.T., Thomas, I.R., and Bowles, N.E. (2013), Enhanced compositional analysis of the Moon using Diviner's long wavelength channels, *European Planetary Science Conference*, abstract 686.

Aronson, J. R. (1986), Optical constants of monoclinic anisotropic crystals: orthoclase, *Spectrochimica Acta Part A: Molecular Spectroscopy*, *42*(2), 187-190.

Aronson, J. R., and A. G. Emslie (1973), Spectral Reflectance and Emittance of Particulate Materials. 2: Application and Results, *Appl. Opt.*, *12*(11), 2573-2584.

Aronson, J.R. (1986), Optical constants of monoclinic anisotropic crystals: Orthoclase, *Spectrochimica Acta Part A: Molecular Spectroscopy*, *42*(2–3), 187–190.

Aronson, J.R., Emslie, A.G., Miseo, E.V., Smith, E.M., Strong, P.F. (1983), Optical constants of monoclinic anisotropic crystals: gypsum, *Applied Optics*, *22*(24), 4093–4098.

Aronson, J.R., Emslie, A.G., Strong, P.F. (1985), Optical constants of triclinic anisotropic crystals: blue vitriol, *Applied Optics*, *24*(8), 1200–1203.

Bandfield, J. L., P. R. Christensen, and M. D. Smith (2000), Spectral data set factor analysis and end-member recovery: Application to analysis of Martian atmospheric particulates, *Journal of Geophysical Research: Planets*, *105*(E4), 9573-9587.

Bandfield, J.L., Hamilton, V.E., and Christensen, P.R. (2000), A Global View of Martian Surface Compositions from MGS-TES, *Science, 287*(5458), 1626–1630.

Beintema, D.A. (1997), PAH's and crystalline silicates in planetary nebula, *Astrophysics and Space Science*, *225*(1-2), 507–512.

Belousov, M.V. and Pavinich, V.F. (1978), Infrared reflection spectra of monoclinic crystals, *Optics and Spectroscopy*, *45*(5), 771–774.

Berreman , D.W. (1972), Optics in Stratified and Anisotropic Media: 4 × 4–Matrix Formulation, *Journal of the Optical Society of America, 62*(4), 502–510.

Berreman, D. W. (1972), Optics in stratified and anisotropic media: 4× 4-matrix formulation, *JOSA*, *62*(4), 502-510.

Bohren, C. F., and D. R. Huffman (1983), *Absorption and scattering of light by small particles*, John Wiley & Sons.

Born, M. and Wolf, E. (1999), Principles of Optics, p. 840, Cambridge University Press, UK.

Bouwman, J., Meeus, G., de Koter, A., Hony, S., Dominik, C., Waters, L.B.F.M. (2001), Processing of silicate dust grains in Herbig Ae/Be systems, *Astronomy and Astrophysics*, *375*, 950–962.

Bowey, J.E., Morlock, A., Kohler, M. and Grady, M. (2007), 2–16 um spectroscopy of micron-sized enstatite $(Mg,Fe)_2Si_2O_6$ silicates from primitive chondritic meteorites, *Monthly Notices of the Royal Astronomical Society, 376*(3), 1367–1374.

Braatz, A., Ott, U., Henning, Th., Jäger, C. and Jeschke, G. (2000), Infrared, ultraviolet, and electron paramagnetic resonance measurements on presolar diamonds: Implications for optical features and origin, *Meteoritics & Planetary Science*, *35*(1), 75–84.

Bradley, J. P., Brownlee, D. E., and Veblen, D. R. (1983), Pyroxene whiskers and platelets in interplanetary dust - Evidence of vapour phase growth, *Nature*, *301*, 473–477.

Cahill, J. T. S., P. G. Lucey, K. R. Stockstill-Cahill, and B. R. Hawke (2010), Radiative transfer modeling of near-infrared reflectance of lunar highland and mare soils, *Journal of Geophysical Research: Planets*, *115*(E12), E12013.

Chandrasekhar, S. (1960), Radiative Transfer, *Dover*.

Chandrasekhar, S. (1960), Radiative Transfer, *Dover*.

Chapman, C.R., Morrison, D., and Zellner, B. (1975), Surface properties of asteroids: A synthesis of polarimetry, radiometry, and spectrophotometry, *Icarus*, *25*(1), 104–130.

Che, C., and T. D. Glotch (2014), Thermal alteration: A possible reason for the inconsistency between OMEGA/CRISM and TES detections of phyllosilicates on Mars?, *Geophysical Research Letters*.

Cheng, J., S. Liang, F. Weng, J. Wang, and X. Li (2010), Comparison of radiative transfer models for simulating snow surface thermal infrared emissivity, *Selected Topics in Applied Earth Observations and Remote Sensing, IEEE Journal of*, *3*(3), 323-336.

Conel, J. E. (1969), Infrared emissivities of silicates: Experimental results and a cloudy atmosphere model of Spectral emission from condensed particulate mediums, *Journal of Geophysical Research*, *74*(6), 1614-1634.

Conel, J. E. (1969), Infrared emissivities of silicates: Experimental results and a cloudy atmosphere model of Spectral emission from condensed particulate mediums, *Journal of Geophysical Research, 74*(6), 1614-1634.

Conel, J. E. (1969), Infrared emissivities of silicates: Experimental results and a cloudy atmosphere model of Spectral emission from condensed particulate mediums, *Journal of Geophysical Research, 74*(6), 1614-1634.

Conel, J.E. (1969), Infrared emissivities of silicates: Experimental results and a cloudy atmosphere model of Spectral emission from condensed particulate mediums, *Journal of Geophysical Research, 74*(6), 1614–1634

De Sanctis, M.C., Ammannito, E. Capria, M.T., Tosi, F., Capaccioni, F., Zambon, F., Carraro, F., Fonte, S., Frigeri, A., Jaumann, R., Magni, G., Marchi, S., McCord, T.B., McFadden, L.A., McSween, H.Y., Mittlefehldt, D.W., Nathues, A., Palomba, E., Pieters, C.M., Raymond, C.A., Russell, C.T., Toplis, M.J., and Turrini, D. (2012), Spectroscopic Characterization of Mineralogy and Its Diversity Across Vesta, *Science, 336*(6082), 697–700.

Denevi, B., P. Lucey, and S. Sherman (2008), Radiative transfer modeling of near-infrared spectra of lunar mare soils: Theory and measurement, *Journal of Geophysical Research: Planets (1991–2012), 113*(E2).

Donaldson Hanna, K. L., M. B. Wyatt, I. R. Thomas, N. E. Bowles, B. T. Greenhagen, A. Maturilli, J. Helbert, and D. A. Paige (2012), Thermal infrared emissivity measurements under a simulated lunar environment: Application to the Diviner Lunar Radiometer Experiment, *Journal of Geophysical Research: Planets*, *117*(E12), E00H05.

Donaldson Hanna, K. L., M. B. Wyatt, I. R. Thomas, N. E. Bowles, B. T. Greenhagen, A. Maturilli, J. Helbert, and D. A. Paige (2012), Thermal infrared emissivity measurements under a

simulated lunar environment: Application to the Diviner Lunar Radiometer Experiment, *Journal of Geophysical Research: Planets*, *117*(E12), E00H05.

Donaldson Hanna, K., I. Thomas, B. Greenhagen, N. Bowles, and C. Pieters (2014), Characterization of Apollo Soil Samples Under Simulated Lunar Conditions, paper presented at Lunar and Planetary Institute Science Conference Abstracts.

Donaldson Hanna, K.L., Thomas, I.R., Bowles, N.E., Greenhagen, B.T., Pieters, C.M., Mustard, J.F., Jackson, C.R.M. and Wyatt, M.B. (2012), Laboratory emissivity measurements of the plagioclase solid solution series under varying environmental conditions, *Journal of Geophysical Research, 117*(E11004), 7pp.

Donev, A., S. Torquato, and F. H. Stillinger (2005), Neighbor list collision-driven molecular dynamics simulation for nonspherical hard particles.: II. applications to ellipses and ellipsoids, *Journal of Computational Physics*, *202*(2), 765-793.

Dorschner, J., Begemann, B., Henning, T., Jaeger, C., and Mutschke, H. (1995), Steps toward interstellar silicate mineralogy. II. Study of Mg–Fe-silicate glasses of variable composition, *Astronomy and Astrophysics, 300*, 503–520.

Dyar, M. D., Sklute, E. C., Menzies, O. N., Bland, P. A., Lindsley, D., Glotch, T., Lane, M. D., Schaefer, M. W., Wopenka, B., Klima, R., Bishop, J. L., Hiroi, T., Pieters, C., and Sunshine, J. (2009), Spectroscopic characteristics of synthetic olivine: An integrated multi-wavelength and multi-technique approach, *American Mineralogist, 94*(7), 883–898.

Dyar, M., E. Sklute, O. Menzies, P. Bland, D. Lindsley, T. Glotch, M. Lane, M. Schaefer, B. Wopenka, and R. Klima (2009), Spectroscopic characteristics of synthetic olivine: An integrated multi-wavelength and multi-technique approach, *American Mineralogist*, *94*(7), 883-898.

Elardo, S. M., D. S. Draper, and C. K. Shearer Jr (2011), Lunar Magma Ocean crystallization revisited: Bulk composition, early cumulate mineralogy, and the source regions of the highlands Mg-suite, *Geochimica et Cosmochimica Acta, 75*(11), 3024-3045.

Fabian, D., Henning, T., Jäger, C., Mutschke, H., Dorschner, J., Wehrhan, O. (2001), Steps toward interstellar silicate mineralogy, *Astronomy & Astrophysics, 378*(1), 228–238.

Friedlander, L., and T. Glotch (2014), Phyllosilicate Spectra Identified at Mawrth Vallis by Factor Analysis and Target Transformation are Consistent with Impact-Related Spectral Change, paper presented at Lunar and Planetary Institute Science Conference Abstracts.

Glotch, T. D. and Rossman, G. R. (2009), Mid-infrared reflectance spectra and optical constants of six iron oxide/oxyhydroxide phases, *Icarus*, *204*(2), 663–671.

Glotch, T. D., Christensen, P. R., and Sharp, T. G. (2006), Fresnel modeling of hematite crystal surfaces and application to martian hematite spherules, *Icarus, 181*, 408–418.

Glotch, T. D., et al. (2010), Highly Silicic Compositions on the Moon, *Science*, *329*(5998), 1510-1513.

Glotch, T. D., et al. (2010b), Highly Silicic Compositions on the Moon, *Science*, *329*(5998), 1510-1513.

Glotch, T. D., Hagerty, J. J. Lucey, P. G., Hawke, B. R. Giguere, T. A., Arnold, J. A., Williams, J.-P. Jolliff, B. L., and Paige, D. A. (2011), The Mairan Domes: Silicic volcanic constructs on the Moon, *Geophys. Res. Lett., 38*(L21204), doi:10.1029/2011GL049548.

Glotch, T. D., J. L. Bandfield, P. R. Christensen, W. M. Calvin, S. M. McLennan, B. C. Clark, A. D. Rogers, and S. W. Squyres (2006), Mineralogy of the light-toned outcrop at Meridiani Planum as seen by the Miniature Thermal Emission Spectrometer and implications for its formation, *Journal of Geophysical Research: Planets*, *111*(E12), E12S03.

Glotch, T. D., P. G. Lucey, J. L. Bandfield, B. T. Greenhagen, I. R. Thomas, R. C. Elphic, N. Bowles, M. B. Wyatt, C. C. Allen, and K. D. Hanna (2010a), Highly silicic compositions on the Moon, *Science, 329*(5998), 1510-1513.

Glotch, T.D. and Rogers, A.D. (2013), Evidence for magma-carbonate interaction beneath Syrtis Major, Mars, *Journal of Geophysical Research: Planets, 118*, 126–137.

Glotch, T.D., Lucey, P.G., Bandfield, J.L., Greenhagen, B.T., Thomas, I.R., Elphic, R.C., Bowles, N.E., Wyatt, M.B., Allen, C.C., Donaldson Hanna, K.L., and Paige, D.A. (2010), Highly Silicic Compositions on the Moon, *Science, 329*(5998), 1510–1513.

Glotch, T.D., Rossman, G.R., and Aharonson, O. (2007), Mid-infrared (5-100 μm) reflectance spectra and optical constants of 10 phyllosilicate minerals, *Icarus, 192*, 605–62.

Goswami, J. N., and M. Annadurai (2008), Chandrayaan-1 mission to the Moon, *Acta Astronautica, 63*(11), 1215-1220.

Greenhagen, B. T., et al. (2010), Global Silicate Mineralogy of the Moon from the Diviner Lunar Radiometer, *Science, 329*(5998), 1507-1509.

Greenhagen, B. T., et al. (2010), Global Silicate Mineralogy of the Moon from the Diviner Lunar Radiometer, *Science, 329*(5998), 1507-1509.

Greenhagen, B. T., P. Lucey, J. Bandfield, P. Hayne, J. Williams, and D. Paige (2011), The Diviner Lunar Radiometer compositional data products: Description and examples, paper presented at Lunar and Planetary Institute Science Conference Abstracts.

Greenhagen, B.T., Lucey, P.G., Wyatt, M.B., Glotch, T.D., Allen, C.C., Arnold, J.A., Bandfield, J.L., Bowles, N.E., Hanna, K.L.D., Hayne, P.O., Song, E., Thomas, I.R., and Paige, D.A. (2010), Global Silicate Mineralogy of the Moon from the Diviner Lunar Radiometer, *Science, 329*(5998), 1507–1509.

Grieve, R. A. F., D. Stoffler, and A. Deutsch (1991), The Sudbury structure - controversial or misunderstood, *J. Geophys. Res.-Planets*, *96*(E5), 22753-22764.

Griffiths, D.J. (1999), Introduction to Electrodynamics, 3rd ed., 576p, Prentice Hall, Upper Saddle River, New Jersey.

Griffiths, R. W., and I. H. Campbell (1990), Stirring and structure in mantle starting plumes, *Earth and Planetary Science Letters*, *99*(1–2), 66-78.

Hamilton, V.E. (2000), Thermal infrared emission spectroscopy of the pyroxene mineral series, *Journal of Geophysical Reasearch*, *105*(E4), 9701–9716.

Hamilton, V.E., Christensen, P.R., McSween, H.Y., and Bandfield, J.L. (2001), Searching for the source regions of martian meteorites using MGS TES: Integrating martian meteorites into the global distribution of igneous materials on Mars, *Meteoritics & Planetary Science, 38*(6), 871–885.

Hanner, M.S., Lynch, D.K., and Russel, R.W. (1994), The 8–13 micron spectra of comets and the composition of silicate grains, *Astrophysical Journal, Part I, 425*(1), 274–285.

Hapke, B. (1993), Introduction to the Theory of reflectance and Emission Spectroscopy, edited, Cambridge University Press, New York.

Hapke, B. (1993), Introduction to the Theory of reflectance and Emission Spectroscopy, edited, Cambridge University Press, New York.

Hapke, B. (1993a), Theory of Reflectance and Emittance Spectroscopy, 472 p, Cambridge University Press, Cambridge, U.K.

Hapke, B. (1996), A model of radiative and conductive energy transfer in planetary regoliths, *Journal of Geophysical Research: Planets (1991–2012)*, *101*(E7), 16817-16831.

Hapke, B. (1996), A model of radiative and conductive energy transfer in planetary regoliths, *Journal of Geophysical Research: Planets (1991–2012)*, *101*(E7), 16817-16831.

Hapke, B. (2008), Bidirectional reflectance spectroscopy: 6. Effects of porosity, *Icarus*, *195*(2), 918-926.

Hapke, B. (2012), *Theory of reflectance and emittance spectroscopy*, Cambridge University Press.

Hapke, B. (2012), Theory of Reflectance and Emittance Spectroscopy, 528 p, Cambridge University Pres, Cambridge, U.K. 2nd edition.

Henderson, B. G., and B. M. Jakosky (1994), Near-surface thermal gradients and their effects on mid-infrared emission spectra of planetary surfaces, *Journal of Geophysical Research: Planets*, *99*(E9), 19063-19073.

Henning, T. and Mutschke, H. (1997), Low-temperature infrared properties of cosmic dust analogues, *Astronomy and Astrophysics, 327*, 743–754.

Hess, P. C. (1994), Petrogenesis of lunar troctolites, *Journal of Geophysical Research: Planets*, *99*(E9), 19083-19093.

Hess, P. C. (1998), Source regions to lunar troctolite parent magmas, paper presented at Lunar and Planetary Institute Science Conference Abstracts.

Hess, P. C. (2000), Petrogenesis of lunar troctolites-Implications for the Moon and its evolution, paper presented at Lunar and Planetary Institute Science Conference Abstracts.

Hofer, S., J. Popp, T.G. Mayerhofer (2014) Dispersion analysis of triclinic $K_2Cr_2O_7$. Vibrational Spectroscopy, 72, 111-118.

Hunt, G. R., and L. M. Logan (1972), Variation of Single Particle Mid-Infrared Emission Spectrum with Particle Size, *Appl. Opt.*, *11*(1), 142-147.

Isaacson, P. J., et al. (2011), Remote compositional analysis of lunar olivine-rich lithologies with Moon Mineralogy Mapper (M3) spectra, *Journal of Geophysical Research: Planets*, *116*(E6), E00G11.

Isaacson, P. J., R. L. Klima, J. M. Sunshine, L. C. Cheek, C. M. Pieters, T. Hiroi, M. D. Dyar, M. Lane, and J. Bishop (2014), Visible to near-infrared optical properties of pure synthetic olivine across the olivine solid solution, *American Mineralogist*, *99*(2-3), 467-478.

Jäger, C., Dorschner, J., Mutschke, H., Posch, T., and Henning, T. (2003), Steps toward interstellar silicate mineralogy. VII. Spectral properties and crystallization behaviour [sic] of magnesium silicates produced by the sol-gel method, *Astronomy and Astrophysics, 408,* 193-204.

Jäger, C., F. Molster, J. Dorschner, T. Henning, H. Mutschke, and L. Waters (1998), Steps toward interstellar silicate mineralogy. IV. The crystalline revolution, *Astronomy and Astrophysics, 339,* 904-916.

Jäger, C., Molster, F.J., Dorschner, J., Henning, Th., Mutschke, H., and Waters, L.B.F.M. (1994), Steps toward interstellar silicate mineralogy. IV. The crystalline revolution, *Astronomy and Astrophysics, 339*, 904–916.

Jäger, C., Mutschke, H., Begemann, B., Dorschner, J., and Henning, T. (1998), Steps toward interstellar silicate mineralogy. 1: Laboratory results of a silicate glass of mean cosmic composition, *Astronomy and Astrophysics, 292*(2), 641–655.

Johnson, E.A., Rossman, G.R., Dyar, M.D., and Valley J.W. (2002), Correlation between OH concentration and oxygen isotope diffusion rate in diopsides from the Adirondack Mountains, New York, *American Mineralogist, 87*(7), 899–908.

Karner, J., Papike, J.J. and Shearer, C.K. (2006), Comparative planetary mineralogy: Pyroxene major- and minor-element chemistry and partitioning of vanadium between pyroxene and melt in planetary basalts, *American Mineralogist, 91*(10), 1574–1582.

Kilma, R.L., Pieters, C.M., and Dyar, M.D. (2008), Characterization of the 1.2 μm M1 pyroxene band: Extracting cooling history from near-IR spectra of pyroxenes and pyroxene-dominated rocks, *Meteoritics & Planetary Science*, *43*(10), 1591–1604.

Kinch, K. M., J. Sohl-Dickstein, J. F. Bell, J. R. Johnson, W. Goetz, and G. A. Landis (2007), Dust deposition on the Mars Exploration Rover Panoramic Camera (Pancam) calibration targets, *Journal of Geophysical Research: Planets*, *112*(E6), E06S03.

Klima, R. L., C. M. Pieters, and M. D. Dyar (2008), Characterization of the 1.2 μm M1 pyroxene band: Extracting cooling history from near-IR spectra of pyroxenes and pyroxene-dominated rocks, *Meteoritics & Planetary Science*, *43*(10), 1591-1604.

Klima, R. L., Pieters, C. M., and Dyar, M. D. (2007), Spectroscopy of synthetic Mg-Fe pyroxenes I: spin-allowed and spin-forbidden crystal field bands in the visible and near-infrared, *Meteoritics & Planetary Science, 42*(2), 235-253.

Klima, R.L., Pieters, C.M., Boardman, J.W., Green, R.O., Head, J.W. III, Isaacson, P.J., Mustard, J.F., Nettles, J.W., Petro, N.E., Staid, M.I., Sunshine, J.M., Taylor, L.A., Tompkins, S. (2011), New insights into lunar petrology: Distribution and composition of prominent low-Ca pyroxene exposures as observed by the Moon Mineralogy Mapper (M^3), *Journal of Geophysical Research, 116*(E00G06), 13 pp.

Kokhanovsky, A. A. (2006), *Light Scattering Reviews: Single and Multiple Light Scattering*, Springer.

Kokhanovsky, A. A. (2006), *Light Scattering Reviews: Single and Multiple Light Scattering*, Springer.

Lane, M.D. (1999), Midinfrared optical constants of calcite and their relationship to particle size effects in thermal emission spectra of granular calcite, *Journal of Geophysical Research—Planets, 104*, 14099–14108.

Liu, D. (2012), An improved radiative transfer model for estimating mineral abundance of immature and mature lunar soils, *LPSC XLIII*.

Logan, L. M., and G. R. Hunt (1970), Emission spectra of particulate silicates under simulated lunar conditions, *Journal of Geophysical Research*, *75*(32), 6539-6548.

Logan, L. M., G. R. Hunt, J. W. Salisbury, and S. R. Balsamo (1973), Compositional implications of Christiansen frequency maximums for infrared remote sensing applications, *Journal of Geophysical Research*, *78*(23), 4983-5003.

Logan, L.M., Hunt, G.R., Salisbury, J.W., and Balsamo, S.R. (1973), Compositional implications of Christiansen frequency maximums for infrared remote sensing applications, *Journal of Geophysical Research, 78*(23), 4983-5003.

Long, L. L., Querry, M. R., Bell, R. J., and Alexander, R. W. (1992), Optical propertied of calcite and gypsum in crystalline and powedered form in the infrared and far-infrared, *Infrared Physics, 34*(2), 191-201.

Longhi, J. (2003), A new view of lunar ferroan anorthosites: Postmagma ocean petrogenesis, *Journal of Geophysical Research: Planets, 108*(E8), 5083.

Lucey, P. G. (2010), Planetary science: Mantle of the Moon exposed?, *Nature Geosci, 3*(8), 517-518.

Lucey, P. G., B. R. Hawke, C. M. Pieters, J. W. Head, and T. B. McCord (1986), A compositional study of the Aristarchus Region of the Moon using near-infrared reflectance spectroscopy, *Journal of Geophysical Research: Solid Earth*, *91*(B4), 344-354.

Lucey, P. G., D. Paige, B. Greenhagen, J. Bandfield, and T. Glotch (2010), Comparison of Diviner Christiansen Feature position and visible albedo: Composition and space weathering implications, paper presented at Lunar and Planetary Institute Science Conference Abstracts.

Lucey, P. G., D. T. Blewett, G. J. Taylor, and B. R. Hawke (2000), Imaging of lunar surface maturity, *Journal of Geophysical Research: Planets*, *105*(E8), 20377-20386.

Lucey, P. G., et al. (2006), Understanding the Lunar Surface and Space-Moon Interactions, *Reviews in Mineralogy and Geochemistry*, *60*(1), 83-219.

Lucy, P.G. (1998), Model near-infrared optical constants of olivine and pyroxene as a function of iron content, *Journal of Geophysical Research: Planets, 103*(E1), 1703–1713.

Lumme, K. and Bowell, E. (1981), Radiative transfer in the surfaces of atmosphereless bodies. I. Theory, *The Astronomical Journal, 86*(11), 1694–1721.

Lyon, R. J. P. (1965), Analysis of rocks by spectral infrared emission (8 to 25 microns), *Economic Geology*, *60*(4), 715-736.

Lyon, R. J. P. (1965), Analysis of rocks by spectral infrared emission (8 to 25 microns), *Economic Geology*, *60*(4), 715-736.

Mackinnon, I.D.R. and Rietmeijer, F.J.M. (1987), Mineralogy of chondritic interplanetary dust particles, *Review of Geophysics, 25*(7), 1527–1553.

Mackowski, D. W., and M. I. Mishchenko (1996), Calculation of the< i> T</i> matrix and the scattering matrix for ensembles of spheres, *JOSA A*, *13*(11), 2266-2278.

Mackowski, D. W., and M. I. Mishchenko (1996), Calculation of the< i> T</i> matrix and the scattering matrix for ensembles of spheres, *JOSA A*, *13*(11), 2266-2278.

Malinowski, E. R. (1991), Factor analysis in chemistry.

Mätzler, C. (2002), MATLAB functions for Mie scattering and absorption, version 2, *IAP Res. Rep*, *8*.

Mayerhofer and Popp (2007) Employing spectra of polycrystalline materials for the verification of optical constants obtained from corresponding low-symmetry single crystals. Applied Optics, 46, 3, 327-334.

Mayerhofer and Popp (2007), Employing spectra of polycrystalline materials for the verification of optical constants obtained from corresponding low-symmetry single crystals, *Applied Optics, 46*(3), 327–334.

Mayerhöfer, T. G., S. Weber, and J. Popp (2011), Simplified formulas for non-normal reflection from monoclinic crystals, *Optics Communications*, *284*(3), 719-723.

Mayerhofer, T.G., Weber, S., and Popp, J. (2010), Simplified formulas for non-normal reflection from monoclinic crystals, *Optics Communications, 284*(3), 719–723.

McCord, T.B., Adams, J.B., Johnson, T.V. (1970), Asteroid vesta: spectral reflectivity and compositional implications, *Science, 168*(3938), 1445–1447.

Mie, G. (1908), Beiträge zur Optik trüber Medien, speziell kolloidaler Metallösungen, *Annalen der physik, 330*(3), 377-445.

Milan, L., Thomas, I., Bowles, N. (2011), Lunar regolith thermal gradients and emission spectra: Modeling and validation, *Journal of Geophysical Research, 116*(E12).

Mishchenko, M. I. (2008), Multiple scattering, radiative transfer, and weak localization in discrete random media: unified microphysical approach, *Reviews of Geophysics*, *46*(2).

Mishchenko, M. I. (2008), Multiple scattering, radiative transfer, and weak localization in discrete random media: unified microphysical approach, *Reviews of Geophysics*, *46*(2).

Mishchenko, M. I., and L. D. Travis (1994), Light scattering by polydispersions of randomly oriented spheroids with sizes comparable to wavelengths of observation, *Applied Optics*, *33*(30), 7206-7225.

Mishchenko, M. I., L. D. Travis, and A. A. Lacis (2002), *Scattering, absorption, and emission of light by small particles*, Cambridge university press.

Mishchenko, M. I., L. D. Travis, and D. W. Mackowski (1996), < i> T</i>-matrix computations of light scattering by nonspherical particles: A review, *Journal of Quantitative Spectroscopy and Radiative Transfer*, *55*(5), 535-575.

Mishchenko, M. I., L. D. Travis, R. A. Kahn, and R. A. West (1997), Modeling phase functions for dustlike tropospheric aerosols using a shape mixture of randomly oriented polydisperse spheroids, *Journal of Geophysical Research: Atmospheres (1984–2012)*, *102*(D14), 16831-16847.

Mishchenko, M. I., L. Liu, and G. Videen (2007), Conditions of applicability of the single-scattering approximation, *Opt. Express*, *15*(12), 7522-7527.

Mishchenko, M.I., Dlugach, J.M., Yanovitskij, E.G. and Zakharova, N.T. (1999), Bidirectional reflectance of flat, opticallt thick particulate layers; an efficient radiative transfer solution and applications to snow and soil surfaces, *Joural of quantitative spectroscopy and radiative transfer*, *63*(2-6), 409–432.

Moersch, J., and P. R. Christensen (1995), Thermal emission from particulate surfaces: A comparison of scattering models with measured spectra, *Journal of Geophysical Research: Planets (1991–2012)*, *100*(E4), 7465-7477.

Moersch, J., and P. R. Christensen (1995), Thermal emission from particulate surfaces: A comparison of scattering models with measured spectra, *Journal of Geophysical Research: Planets (1991–2012)*, *100*(E4), 7465-7477.

Molster, F. and Kemper, C. (2004), Crystalline Silicates, *Space Science Reviews, 119*(1–4), 3–28.

Molster, F.J., Waters, L.B.F.M., Tielens, A.G.G.M., Barlow, M.J. (2002), Crystalline silicate dust around evolved stars, *Astronomy and Astrophysics, 382*, 184–221.

Mustard, J. F., and J. E. Hays (1997), Effects of hyperfine particles on reflectance spectra from 0.3 to 25 μm, *Icarus*, *125*(1), 145-163.

Mustard, J. F., et al. (2011), Compositional diversity and geologic insights of the Aristarchus crater from Moon Mineralogy Mapper data, *Journal of Geophysical Research: Planets*, *116*(E6), E00G12.

Mustard, J. F., et al. (2011), Compositional diversity and geologic insights of the Aristarchus crater from Moon Mineralogy Mapper data, *Journal of Geophysical Research: Planets*, *116*(E6), E00G12.

Mustard, J.F., Poulet, F., Gendrin, A., Bibring, J.P., Langevin, Y., Gondet, B., Mangold, N., Bellucci, G., and Altieri, F. (2005), Olivine and Pyroxene Diversity in the Crust of Mars, *Science, 30(*5715), 1594–1597.

Mutschke, H., Andersen, A.C., Jäger, C., Henning, T., and Braatz, A. (2004), Optical data of meteoritic nano-diamonds from far-ultraviolet to far-infrared wavelengths, *Astronomy and Astrophysics, 423*, 983–993.

Nash, D. B., J. W. Salisbury, J. E. Conel, P. G. Lucey, and P. R. Christensen (1993), Evaluation of infrared emission spectroscopy for mapping the moon's surface composition from lunar orbit, *Journal of Geophysical Research: Planets*, *98*(E12), 23535-23552.

Nash, D. B., J. W. Salisbury, J. E. Conel, P. G. Lucey, and P. R. Christensen (1993), Evaluation of infrared emission spectroscopy for mapping the moon's surface composition from lunar orbit, *Journal of Geophysical Research: Planets, 98*(E12), 23535-23552.

Ody, A., Poulet, F., Langevin, Y., Bibring, J.P., Bellucci, G., Altieri, F., Gondet, B., Vincendon, M., Carter, J., and Manaud, N. (2012), Global maps of anhydrous minerals at the surface of Mars from OMEGA/MEx, *Journal of Geophysical Research: Planets, 117*(E11).

Ohtake, M., et al. (2009), The global distribution of pure anorthosite on the Moon, *Nature*, *461*(7261), 236-240.

Paige, D.A., Foote, M.C., Greenhagen, B.T., Schofield, J.T., Calcutt, S., Vasavada, A.R., Preston, D.J., Taylor, F.W., Allen, C.C., Snook, K.J., Jakosky, B.M., Murray, B.C., Soderblom, L.A., Jau, B., Loring, S., Bulharowski, J., Bowles, N.E., Thomas, I.R., Sullivan, M.T., Avis, C., Jong, E.M., Hartford, W., and McCleese, D.J. (2010), The Lunar Reconnaissance Orbiter Diviner Lunar Radiometer Experiment, *Space Science Reviews, 150*(1-4), 125–160.

Pavinich, V.F. and Belousov, M.V. (1978), Dispersion analysis of reflection spectra of monoclinic crystals, Optics and Spectroscopy 45, 881. Translated from Opt. Spektrosk. 45, 1114.

Pieters, C. M. (1982), Copernicus Crater Central Peak: Lunar Mountain of Unique Composition, *Science*, *215*(4528), 59-61.

Pieters, C. M. (1996), Plagioclase and maskelynite diagnostic features, paper presented at Lunar and Planetary Institute Science Conference Abstracts.

Pieters, C. M., et al. (2009), The Moon Mineralogy Mapper (M3) on Chandrayaan-1, *Current Science (00113891)*, *96*(4), 500-505.

Pitman, K. M., M. J. Wolff, and G. C. Clayton (2005), Application of modern radiative transfer tools to model laboratory quartz emissivity, *Journal of Geophysical Research: Planets (1991–2012)*, *110*(E8).

Pitman, K. M., M. J. Wolff, and G. C. Clayton (2005), Application of modern radiative transfer tools to model laboratory quartz emissivity, *Journal of Geophysical Research: Planets (1991–2012)*, *110*(E8).

Powell, K., P. McGovern, and G. Kramer (2012), Olivine Detections at the Rim of Crisium Basin with Moon Mineralogy Mapper, paper presented at Lunar and Planetary Institute Science Conference Abstracts.

Ramsey, M.S. and Christensen, P.R. (1998), Mineral abundance determination: Quantitative deconvolution of thermal emission spectra, *Journal of Geophysical Research, 103*(B1), 577–596.

Rogers, A.D. and Christensen, P.R. (2007), Surface mineralogy of Martian low–albedo regions from MGS–TES data: Implications for upper crustal evolution and surface alteration, *Journal of Geophysical Research, 112*(E01003).

Rogers, A.D., Bandfield, J.L., and Christensen, P.R (2007), Global spectral classification of Martian low-albedo regions with Mars Global Surveyor Thermal Emission Spectrometer (MGS-TES) data, *Journal of Geophysical Research, 112*(E02004).

Roush, T., Pollack, J., Orenberg, J. (1991), Derivation of midinfrared (5–25 μm) optical constants of some silicates and palagonite, *Icarus, 94*(1), 191–208.

Ruff, S. W., and P. R. Christensen (2002), Bright and dark regions on Mars: Particle size and mineralogical characteristics based on Thermal Emission Spectrometer data, *Journal of Geophysical Research: Planets*, *107*(E12), 5119.

Ruff, S. W., P. R. Christensen, P. W. Barbera, and D. L. Anderson (1997), Quantitative thermal emission spectroscopy of minerals: A laboratory technique for measurement and calibration, *Journal of Geophysical Research: Solid Earth (1978–2012)*, *102*(B7), 14899-14913.

Ruff, S. W., P. R. Christensen, P. W. Barbera, and D. L. Anderson (1997), Quantitative thermal emission spectroscopy of minerals: A laboratory technique for measurement and calibration, *Journal of Geophysical Research: Solid Earth (1978–2012)*, *102*(B7), 14899-14913.

Ryder, G. (1991), Lunar ferroan anorthosites and mare basalt sources - the mixed connection, *Geophysical Research Letters*, *18*(11), 2065-2068.

Ryder, G., M. D. Norman, and G. Jeffrey Taylor (1997), The complex stratigraphy of the highland crust in the Serenitatis region of the Moon inferred from mineral fragment chemistry, *Geochimica et Cosmochimica Acta*, *61*(5), 1083-1105.

Salisbury, J. W., A. Basu, and E. M. Fischer (1997), Thermal Infrared Spectra of Lunar Soils, *Icarus*, *130*(1), 125-139.

Salisbury, J. W., A. Wald, and D. M. D'Aria (1994), Thermal-infrared remote sensing and Kirchhoff's law: 1. Laboratory measurements, *Journal of Geophysical Research: Solid Earth (1978–2012)*, *99*(B6), 11897-11911.

Salisbury, J. W., A. Wald, and D. M. D'Aria (1994), Thermal-infrared remote sensing and Kirchhoff's law: 1. Laboratory measurements, *Journal of Geophysical Research: Solid Earth (1978–2012)*, *99*(B6), 11897-11911.

Salisbury, J. W., and A. Wald (1992), The role of volume scattering in reducing spectral contrast of reststrahlen bands in spectra of powdered minerals, *Icarus*, *96*(1), 121-128.

Salisbury, J. W., and A. Wald (1992), The role of volume scattering in reducing spectral contrast of reststrahlen bands in spectra of powdered minerals, *Icarus*, *96*(1), 121-128.

Salisbury, J. W., and L. S. Walter (1989), Thermal infrared (2.5–13.5 μm) spectroscopic remote sensing of igneous rock types on particulate planetary surfaces, *Journal of Geophysical Research: Solid Earth*, *94*(B7), 9192-9202.

Salisbury, J. W., and L. S. Walter (1989), Thermal infrared (2.5–13.5 μm) spectroscopic remote sensing of igneous rock types on particulate planetary surfaces, *Journal of Geophysical Research: Solid Earth*, *94*(B7), 9192-9202.

Salisbury, J. W., B. Hapke, and J. W. Eastes (1987), Usefulness of weak bands in midinfrared remote sensing of particulate planetary surfaces, *Journal of Geophysical Research: Solid Earth (1978–2012)*, *92*(B1), 702-710.

Salisbury, J.W. (1972), Spectroscopic remote sensing of lunar surface composition, *Earth, Moon and Planets*, *5*(3-3), 332−347.

Seitz, F. (1940), Modern theory of solids, McGraw-Hill, New York.

Sharkov, E. A. (2003), *Passive microwave remote sensing of the Earth: physical foundations*, Springer.

Shearer, C. K., and J. Papike (2005), Early crustal building processes on the moon: Models for the petrogenesis of the magnesian suite, *Geochimica et Cosmochimica Acta*, *69*(13), 3445-3461.

Shkuratov, Y., Starukhina, L., Hoffman, H. and Arnold, G. (1999), A model of spectral albedo of particulate surfaces: implications for optical properties of the moon, *Icarus, 137*(2), 235–246.

Shkuratov, Y.G., Kaydash, V.G. and Pieters, C.M. (2004), Lunar Clinopyroxene and Plagioclase: Surface Distribution and Composition, *Solar System Research, 39*(4), 255–266. Translated from *Astronomicheskii Vestnik, 39*, 4, 2005, 291–303 (in Russian).

Sogawa, H., Koike, C., Chihara, H., Suto, H., Tachibaba, S., Tsuchiyama, A., and Kozasa, T. (2006), Infrared reflection specra of forsterite crystal, *Astronomy & Astrophysics, 451*, 357–361.

Song, E., Bandfield, J.L., Lucey, P.G., Greenhagen, B.T., Paige, D.A. (2013), Bulk mineralogy of lunar crater central peaks via thermal infrared spectra from the Diviner Lunar Radiometer: A study of the Moon's crustal composition at depth, *Journal of Geophysical Research: Planets, 118*(4), 689–707.

Song, E., J. L. Bandfield, P. G. Lucey, B. T. Greenhagen, and D. A. Paige (2013), Bulk mineralogy of lunar crater central peaks via thermal infrared spectra from the Diviner Lunar Radiometer: A study of the Moon's crustal composition at depth, *Journal of Geophysical Research: Planets, 118*(4), 689-707.

Spitzer, W., and D. Kleinman (1961), Infrared lattice bands of quartz, *Physical Review, 121*(5), 1324.

Spitzer, W.G. and Kleinman, D.A. (1961), Infrared lattice bands of quartz, *Physical Review, 121*(5,) 1324–1335.

Spitzer, W.G., Kleinman, D.A. and Walsh, D. (1959), Infrared properties of hexagonal silicon carbide, *Physical Review, 113*(1), 127–132.

Stamnes, K. et al. (2000) DISORT, a general-purpose Fortran program for discrete-ordinate-method radiative transfer in scattering and emitting layered media: documentation of methodology. Goddard Space Flight Center, NASA .

Stewart, S. (2011), Impact basin formation: The mantle excavation paradox resolved, paper presented at Lunar and Planetary Institute Science Conference Abstracts.

Sunshine, J. M., and C. M. Pieters (1998), Determining the composition of olivine from reflectance spectroscopy, *Journal of Geophysical Research: Planets*, *103*(E6), 13675-13688.

Sunshine, J. M., C. M. Pieters, and S. F. Pratt (1990), Deconvolution of mineral absorption bands: An improved approach, *Journal of Geophysical Research: Solid Earth*, *95*(B5), 6955-6966.

Sunshine, J.M., Bus, J., McCoy, T.J., Burbine, T.H., Corrigan, C.M., and Binzel, R.P. (2004), High–calcium pyroxene as an indicator of igneous differentiation in asteroids and meteorites, *Meteoritics & Planetary Science, 39*(8), 1343–1357.

Suto, H., Koike, C., Sogawa, H., Tsuchiyama, A., Chihara, H., and Mizutani, K. (2002), Infrared spectra of fayalite crystal, *Astronomy & Astrophysics, 389*, 568–571.

Thomas, I., N. Bowles, B. Greenhagen, T. Glotch, K. Donaldson Hanna, M. Wyatt, J. Bandfield, and D. Paige (2010), Emission measurements of lunar analogues for interpretation of returning data from the Diviner Lunar Radiometer on NASA's Lunar Reconnaissance Orbiter, paper presented at Lunar and Planetary Institute Science Conference Abstracts.

Thomas, I., N. Bowles, B. Greenhagen, T. Glotch, K. Donaldson Hanna, M. Wyatt, J. Bandfield, and D. Paige (2010), Emission measurements of lunar analogues for interpretation of returning data from the Diviner Lunar Radiometer on NASA's Lunar Reconnaissance Orbiter, paper presented at Lunar and Planetary Institute Science Conference Abstracts.

Thomas, N., and J. Bandfield (2013), Identification of Spectral Endmembers in CRISM Data Using Factor Analysis and Target Transformation, paper presented at Lunar and Planetary Institute Science Conference Abstracts.

Tompkins, S., and C. M. Pieters (1999), Mineralogy of the lunar crust: Results from Clementine, *Meteoritics & Planetary Science*, *34*(1), 25-41.

Tompkins, S., and Pieters, C.M. (1999), Mineralogy of the lunar crust: Results from Clementine, *Meteroritics and Planetary Science*, *34*, 25–41.

Van de Hulst, H. (1957), Light scattering by small particles.

Wald, A. E., and J. W. Salisbury (1995), Thermal infrared directional emissivity of powdered quartz, *Journal of Geophysical Research: Solid Earth (1978–2012)*, *100*(B12), 24665-24675.

Wenrich, M. L., and Christensen, P. R. (1996), Optical constants of minerals derived from emission spectroscopy: Application to quartz, *Journal of Geophysical Research: Solid Earth*, *101*, 15921–15931.

Wieczorek, M., B. Jolliff, A. Khan, M. Pritchard, B. Weiss, J. Williams, L. Hood, K. Righter, C. Neal, and C. Shearer (2006), New views of the moon, *Rev. Min. Geochem*, *60*, 221-364.

Wolff, M. J., and R. T. Clancy (2003), Constraints on the size of Martian aerosols from Thermal Emission Spectrometer observations, *Journal of Geophysical Research: Planets*, *108*(E9), 5097.

Yamamoto, S., et al. (2010), Possible mantle origin of olivine around lunar impact basins detected by SELENE, *Nature Geosci*, *3*(8), 533-536.

Yamamoto, S., et al. (2010), Possible mantle origin of olivine around lunar impact basins detected by SELENE, *Nature Geosci*, *3*(8), 533-536.

Yamamoto, S., et al. (2012), Olivine-rich exposures in the South Pole-Aitken Basin, *Icarus*, *218*(1), 331-344.

Yamamoto, S., et al. (2012), Olivine-rich exposures in the South Pole-Aitken Basin, *Icarus*, *218*(1), 331-344.

Yeh, P. (1979), Optics of anisotropic layered media: A new 4 × 4 matrix algebra, *Surface Science, 96(*1-3), 41–53.

Zeidler, S., Posch, T., and Mutschke, H. (2013), Optical constants of refractory oxides at high temperatures. Mid-infrared properties of corundum, spinel, and alpha-quartz, potential carriers of the 13 mum feature, *Astronomy & Astrophysics, 553*(81).

Zeidler, S., Posch, T., Mutschke, H., Richter, H., and Wehrhan, O. (2011), Near-infrared absorption properties of oxygen-rich stardust analogs. The influence of coloring metal ions, *Astronomy & Astrophysics, 526*(68).